Modelling Directional Casting Processes in which Heat Conduction and Cavity Radiation are the Dominant Modes of Heat Transfer

P J Kotschy

Modelling Directional Casting Processes in which Heat Conduction and Cavity Radiation are the Dominant Modes of Heat Transfer

by

P J Kotschy

A thesis submitted for the degree of Doctor of Philosophy in the Faculty of Engineering

Department of Mechanical Engineering
University of Cape Town
Republic of South Africa

February 2002

Abstract

Directional investment casting processes involve complex interactions of various mechanisms of heat and mass transfer in spatially complex domains and in the presence of a change of phase. In particular, the transfer of heat within the furnace occurs in the form of conduction, convection and radiation. This thesis addresses the development of computational techniques to simulate, at a macroscopic scale, such casting processes.

In this study the conservation of heat energy within the casting is assumed to be maintained by conduction, accompanied by the release of latent heat energy during solidification. The overall state of the radiation in the furnace chamber is analysed in terms of the absorbed, emitted and reflected energies for each surface defining the geometry of the chamber. By applying a diffuse–grey approximation to these energies, an expression for the net heat flux for each surface is derived.

A Galerkin isoparametric finite element formulation using first–order hexahedral elements is extended to numerically couple the radiant interactions. A backward–difference temporal algorithm, together with a modified Newton iterative method, is used to solve the non–linear equations at selected instants during the solidification history. A novel algorithm allows the hitherto tight coupling of the conduction and radiation calculations to be loosened somewhat without significant loss of accuracy. The diagonal dominance of the equations describing the radiant interactions can then be exploited in a Gauss–Seidel relaxation solution method.

The notoriously high cost associated with cavity radiation computations is attributable to the large size of the required view factor database. The cost is roughly proportional to the cube of the number of surfaces representing the geometry of the furnace chamber. A primary objective of this work is to reduce both this cost and the time spent by the analyst in setting up the computer models. This is achieved along four fronts, namely: reducing the required number of view factors; reducing the cost of calculating each view factor; reducing the cost associated with each Newton iteration; and finally, making possible the specification of symmetry planes at an abstracted level. In particular, the analyst is now able to specify symmetries between two or more dissimilar regions and between regions having unequal mesh densities.

Results of the simulations of four investment casting processes are analysed. The accuracy of the simulations is checked against experimentally measured thermal histories and certain measured microstructural features. It is evident that the radiant interactions occurring outside

the casting significantly influence the solidification behaviour within. In the particular case of a clustered directional casting, radial thermal gradients arise not only from the radiant interaction of the casting and ceramic mould surfaces with the furnace, but also from a 'self–interaction' between the various surfaces. With respect to initializing the database of view factors for the simulation of the clustered casting, application of the techniques developed here result in a 39–fold reduction in the computational cost.

Declaration

I, Paul Johann Kotschy, declare that this thesis is essentially my own work and that it has not been submitted for a degree at any other university.

.....

P J Kotschy

February 2002

To
Mom, Dad and Mels—my Everlasting

Acknowledgements

I express my gratitude to the following:

My supervisors, Dr G Mitchell, Professor G Nurick and the late Professor John Martin for their patience and guidance during my studies

The Division for Materials Science and Technology of the CSIR for their financial support and for the use of their casting facilities

Mels, Dr Mitchell and Professor Martin for their assistance in proof reading the text

Contents

List of Figures

List of Tables

List of Algorithms

Nomenclature

Abbreviations

Al	Aluminium
Al_2O_3	Aluminium dioxide
B	Boron
C	Carbon
Co	Cobalt
Cr	Chromium
DS	Directional solidification
Hf	Hafnium
Nb	Niobium
Ni	Nickel
PDAS	Primary dendrite arm spacing
SC	Single crystal solidification
SiO_2	Silicon dioxide
Ti	Titanium
W	Tungsten
Zr	Zirconium

Ordinary Symbols

$\hat{\mathbf{a}}$	Unit vector parallel to an axis of rotation
A	Surface area
A^n	Surface area of radiating facet S^n
a_N, b_N, c_N	Parameters defining N_N^e with $a_N, b_N, c_N \in \{-1, 1\}$
a_N, b_N, c_N	Parameters defining N_N^e with $a_N, b_N, c_N \in \{-1, 1\}$
A_p	$A \cos\beta$, projected surface area (Figure 3.5)
A'^n	Surface area of radiating facet S'^n

$\mathbf{b}$ Arbitrary point on an axis of rotation $\hat{\mathbf{a}}$

b Axial position of baffle relative to the casting geometry

b_0 Initial axial position of baffle relative to the casting geometry

$\bar{c}$ Projection of $\mathbf{c}$ in the direction $(-\hat{\mathbf{n}}_w)$

$\mathbf{c}'$ Transformation of centroid $\mathbf{c}$ according to the mapping $\mathbb{S}^{A^{-1}} : \mathbf{c} \mapsto \mathbf{c}'$

$\mathbf{c}^n$ Centroid of radiating facet S^n

C_p Specific heat capacity

C_s Sensible specific heat capacity in the interval $[T_S, T_L]$

$\mathbf{d}^n$ Difference vector, $\mathbf{x}^{n+1} - \mathbf{x}^n$

$e_{\lambda b}$ Hemispherical spectral emissive power

$e'_{\lambda b}$ Directional spectral emissive power

$e'_{\lambda i}$ Directional spectral incident power

e'_{λ} Directional spectral emissive power

e Hemispherical total emissive power

e_b Total emissive power for a blackbody

$e_{\max}$ Total number of finite elements

$F_{\max}$ Total number of facets comprising the radiating cavity

$F_{\mathcal{M}}$ Total number of *master* facets

$F_{\mathcal{S}}$ Total number of *slave* facets

$F_{\mathcal{S}}^n$ Number of slave facets which are symmetric to the master facet S^n

F View (or configuration) factor

f_t Approximation to $f(t)$ for any function f

F_{ma} Magnitude of the view from facet S^m to the ambient environment

F_{mn} Magnitude of the view of facet S^m from facet S^n

G Thermal gradient across the mushy zone

g Volumetric heat generation term

G_{mn} Gauss–Seidel matrix element equal to $\delta_{mn} - \rho_m F_{mn}$

H Enthalpy

h Convection coefficient

$i'_{\lambda b}$ Spectral intensity for a blackbody

i'_{λ} Spectral intensity

I_{np} Index mapping function (page ??)

J_{MN} Jacobian matrix element at time $t + \Delta t$

k Thermal conductivity

$K(\mathbf{x}, t)$ Solid–liquid interface surface equation

L Latent heat of fusion per unit mass

$m_{\max}$ Number of (T_m, ϵ_m) samples

$N_{\max}$ Total number of interpolation functions, $N_M(\mathbf{x})$

$\hat{\mathbf{n}}$, $\hat{\mathbf{n}}'$ Unit normal vectors

$\hat{\mathbf{n}}^n$ Average unit normal vector for facet S^n

$\hat{\mathbf{n}}_w$ Unit direction of casting withdrawal

N_M M'th interpolation function in the method of weighted residuals

N_M^e M'th interpolation function defined only over finite element e

$n_{\max}$ Number of temporal sub–divisions of the casting withdrawal stage

$\mathbf{p}$ Point at intersection of line $\overline{\mathbf{c}^n\mathbf{c}^m}$ and the facet S^p
Focus of an arc swept about an axis $\hat{\mathbf{a}}$

$Q'_{\lambda a}$ Radiant energy absorbed by a surface per unit time in wavelength interval $\mathrm{d}\lambda$ and in solid angle $\mathrm{d}\omega$

$Q'_{\lambda b}$ Radiant energy emitted from a black surface per unit time in wavelength interval $\mathrm{d}\lambda$ and in solid angle $\mathrm{d}\omega$

$Q'_{\lambda e}$ Radiant energy emitted from a non–black surface per unit time in wavelength interval $\mathrm{d}\lambda$ and in solid angle $\mathrm{d}\omega$

$Q'_{\lambda i}$ Radiant energy incident on a surface per unit time in wavelength interval $\mathrm{d}\lambda$ and in solid angle $\mathrm{d}\omega$

$\mathbf{q}$ Heat flux vector

q^n Average net heat flux over facet S^n

q_i^n Average incident flux over facet S^n

q_o^n Average radiosity over facet S^n

q^{ma} Approximation to the net heat flux at the integration point on the elemental face coincident with radiating facet S^m

Q_a Radiant energy absorbed by a surface per unit time

q_g Net heat flux across a 'thermal gap'

Q_i Radiant energy incident on a surface per unit time

q_i Incident radiant energy per unit time and per unit area

q_o Radiosity

Q_r Radiant energy reflected by a surface per unit time

q_R Heat flux component of $\mathbf{q}$ normal to S_R

$q_{\lambda o}$ Hemispherical spectral radiosity

$q'_{\lambda o}$ Directional spectral radiosity

q_o^{*m} Initial estimate of the average radiosity of facet S^m

$\mathbf{R}$ Givens rotation matrix

R_t^N Weighted residual at time t for the N'th degree of freedom

$S(x)$ Step function

S^n n'th radiating facet

S_I I'th boundary surface over which temperature is prescribed

S_R R'th boundary surface over which heat flux is prescribed

S'^p Transformation of the symmetric facet, S^p, onto the symmetry's master facet set

T_h Temperature of the furnace heaters

T_{melt} Melting temperature if solidification (or melting) takes place at a single temperature

T_c Temperature of the furnace walls

T Temperature

t time

T^n Average temperature over the radiating facet S^n. Note that this is distincly different from $T^N(t)$ which is a nodal quantity

$T^N(t)$ N'th nodal temperature approximation to $T(\mathbf{x}^N, t)$

$T^{n\alpha}$ Temperature of the α'th integration point of the finite elemental face which is geometrically exactly coincident with facet S^n

T_0 Initial temperature

T_a Ambient temperature

T_I Prescribed temperature over surface S_I

T_L Liquidus temperature

T_m m'th temperature sample for temperature–dependent emissivity

t_n n'th instant at which casting withdrawal speed changes

T_S Solidus temperature

T_t^N Approximation to the N'th nodal temperature, $T(\mathbf{x}^N, t)$

T_{ref} Reference temperature at which enthalpy, $H(T)$, is defined to vanish

T_{ga}, T_{gb} Temperatures of the a'th and b'th surfaces at a 'thermal gap'

$\mathbf{u}(\mathbf{x})$ Utility vector function equal to $\mathbf{p}(\mathbf{x}) - \mathbf{x}$

$\mathbf{u}^n$ Difference vector, $\mathbf{p} - \mathbf{x}^n$

$\mathbf{v}_w$ Casting withdrawal velocity, $v_w(t)\hat{\mathbf{n}}_w$, relative to the furnace geometry

V Volume

V^e Volume of finite element e

V_S Solidus speed normal to the solidus isotherm

v_{wn} Constant casting withdrawal speed in time interval $[t_{n-1}, t_n]$

$\mathbf{w}^n$ Utility cross–product, $\mathbf{d}^n \times \mathbf{u}^n$

v_w Magnitude of the casting withdrawal velocity

$\mathbf{x}$, $\mathbf{x}'$ Position vectors

$\mathbf{x}^N$ Position vector of N'th node

$\mathbf{x}_K$ Point on the interface surface $K(\mathbf{x}, t)$

x_b, x_c, z_c Distance coordinates defined in Figure 6.11

$\mathbf{y}$ Arbitrary point on an axis of rotation

Greek Symbols

α Hemispherical total absorptivity

α'_λ Directional spectral absorptivity

β Spherical coordinate: azimuthal angle

$\beta(\mathbf{x}, \mathbf{y})$ Angle between normal vector at $\mathbf{x}$ and the line joining $\mathbf{x}$ and $\mathbf{y}$

ΔL Total latent heat release over $[T_S, T_L]$

Δt Time increment

$\Delta T^{n\alpha}$ The difference $T^{n\alpha} - T^n$

Δ 'Distance' between two facets

δ Height of the baffle zone (Figure 4.10

$\Delta\mathbf{x}$ Difference vector between two integration points

ϵ Hemispherical total emissivity

ϵ_m m'th emissivity sample for temperature–dependent emissivity

ϵ_n Average hemispherical emissivity over facet S^n

ϵ_{ga}, ϵ_{gb} Emissivities of the a'th and b'th surfaces at a 'thermal gap'

ϵ'_λ Directional spectral emissivity

γ Parameter in generalised trapezoidal rule
Switch in Algorithm 2 for radiation to ambient environment

λ Wavelength

π Constant, 3.141592653

$\boldsymbol{\xi}$ Position vector, expressed in the natural coordinate system (ξ, η, ζ) of a hexahedral finite element

ξ, η, ζ Natural local spatial coordinates spanning the unit cube

ρ Hemispherical total reflectivity

ρ_m Mass density

ρ_n Average hemispherical reflectivity over facet S^n

σ Stefan–Boltzmann constant, 5.729×10^{-8} $\mathrm{Wm^{-2}K^{-4}}$

θ Spherical coordinate: axial angle
Angle of rotation i.r.o. cyclic symmetry

θ_b, θ_c Angular coordinates defined in Figure 6.11

ϕ Arbitrary finite variational field having C_1 continuity in volume V

ϕ^N N'th arbitrary variational field

ω Solid angle such that $\mathrm{d}\omega = \sin(\beta)\mathrm{d}\beta\mathrm{d}\theta$

Calligraphic Symbols

$\mathcal{S}_{\max}$ Total number of symmetries within the cavity

$\mathcal{S}^A$ The A'th symmetry operation

$\mathcal{S}^A_{\mathcal{M}}$ Set of radiating gmaster facet indices for the A'th symmetry

$\left|\mathcal{S}^A_{\mathcal{M}}\right|$ The number of master facets in the set $\mathcal{S}^A_{\mathcal{M}}$

$\mathcal{S}^A_{\mathcal{M}b}$ The b'th facet index in the set $\mathcal{S}^A_{\mathcal{M}}$

Special Symbols

$\approx$ approximately equal to

$\delta(.)$ Dirac distribution functional

δ_{NM} Kronecker–delta symbol, equal to 1 when $N = M$, and 0 otherwise

$\dfrac{\partial}{\partial n}$ Component, $\hat{\mathbf{n}} \cdot \dfrac{\partial}{\partial \mathbf{x}}$, of the gradient in the direction $\hat{\mathbf{n}}$

$\oint_{\partial A}$ Closed integral along path bounding A

$\dfrac{\partial}{\partial \mathbf{x}}$ Gradient operator

$\dot{\square}$ Partial derivative wrt t

$\equiv$ defined as

$\square|_{\square}$ Evaluated at, evaluated on

$\forall$ for all

D Hemispherical solid angle

$\in$ is an element of

∞ infinity

∂A Path bounding surface area A

∂V	Surface bounding volume V
$\partial \mathbf{x}/\partial \boldsymbol{\xi}$	Transformation matrix of the map $\mathbf{x} : \boldsymbol{\xi} \mapsto \mathbf{x}(\boldsymbol{\xi})$
$\lvert\square\rvert$	Absolute value, vector length
$\mathbb{R}$	The set of real numbers
$\square \cdot \square$	Inner product
$\square \times \square$	Cross product
§	Section
det(.)	determinant of

Chapter 1

Introduction

The directional investment casting process involves complex interactions of various mechanisms of heat and mass transfer in spatially complex domains and in the presence of a change of phase. Because of these intrinsic complexities, experimental 'trial-and-error' methods have traditionally been used in a foundry to eliminate defects and to improve casting quality and reproduceability. However, as component designs have become more complicated and requirements on microstructural integrity have become tighter, alternative methods have been sought. It is now with relatively recent advances in computer hardware and software technologies that computer modelling has become one such alternative method; and it is to this alternative that this thesis is directed.

Many of the mechanisms underlying solidification processes are now well understood. They are usually described by balance laws which differ dramatically depending on the length and time scales at which the subject is studied [1]. At the smallest length and time scales the study of solidification is concerned with the thermodynamic driving forces for nucleation of solid particles and the kinetics of the subsequent growth of the particles. Much research activity is directed at modelling solidification at these small scales [2].

While not discounting the importance of this work, many technical challenges still exist at the larger scales. Indeed, these technical challenges often limit the extent to which the abovementioned research work can be applied to practical industrial problems [3]. This thesis confronts some of the challenges in modelling investment casting processes at the macroscopic scale.

In general, at the macroscopic scale the modelling problem involves a coupling of physical laws which account for the conservation of mass, heat energy, momentum, and, in the case of the solidification of multi–component alloys, species.

Since it is assumed that the molten metal does not convect, the conservation of mass and momentum are trivial. The conservation of species, on the other hand, results in the formation of a spatial zone of instability known as the *mushy zone* in which metal solidification takes place as the molten metal cools [4, 5, 6]. This zone is bounded empirically by two surfaces—one at

the *solidus* temperature and the other at the *liquidus* temperature. The spontaneous release of heat energy of fusion occurs within the mushy zone.

The conservation of heat energy must account for the heat transfer modes of conduction and radiation. It is assumed that conduction heat transfer takes place within the casting, and that the numerous time–dependent three–dimensional radiant interactions take place within the furnace cavity.

During vacuum investment casting, the transfer of heat energy between the casting and the furnace walls is dominated by radiation. However, this radiant interaction is complex and is therefore not easy to simulate computationally. Sources of this complexity are identified as follows:

- Not only is radiant energy exchanged between the casting and the furnace, but also between the various surfaces of the casting and the furnace separately. A consequence of this self irradiation is that the thermal state at any point in the furnace therefore depends on the thermal state globally
- In the case of directional casting, the relative motion between the casting and the furnace means that the geometry of the radiating cavity changes with time. Hence the interactions are time–dependent
- A common casting configuration is one in which individual components are arranged cyclically around a central axis. This arrangment is known as a *cluster*. Despite the possible existence of planes of geometric symmetry in the cluster, the contribution of each component in the cluster to the overall radiant interaction cannot be neglected. This adds significantly to the size of the computation

Addressing this radiant interaction requires a level of computing resource that is often not in proportion with the impact of radiation on the overall problem. In many cases the required resource is so high that either it limits the scope and size of problems that can be addressed using computer methods [7], or it renders the models unsuitable for iterative analysis with each simulation run taking too long.

In a review of numerical methods used to predict radiative heat transfer, Howell stressed the need for developing more effective computational methods [8]. Howell identified the important characteristics that should be considered in the development of any new method as being: (1) computational efficiency, (2) accuracy, (3) ability to handle irregular three–dimensional geometries, and (4) mesh compatibility with conduction/convection analysis methods. Although many of the current numerical techniques may contain some of these qualities, it is my view that no existing method handles all. The primary objective of this thesis is therefore to extend our ability to simulate 'real–world' investment casting processes in a manner which addresses all these qualities.

In particular, a numerical model of the radiant interactions is developed which:

- is both sufficiently accurate and computationally efficient
- couples very easily to current standard computer models of heat transfer
- reduces the analyst's initial effort in setting up the models

Computer models of directional investment casting processes started appearing early in the 1980s [9]. In the same decade Giamei *et al* used a temperature and time dependent convection boundary condition to account for the radiant interaction [10]. In this relatively simple approach the geometry of the furnace was not accounted for explicitly, and the models could only be applied to castings of single components of convex shape. This approach was later extended by Kotschy and Carter by introducing time–dependent radiation view factors into the boundary condition [11]. Although reasonable agreement between calculated and measured results was obtained, the treatment was still restricted to the analysis of single component castings.

Giamei [12, 13] and Vermont [14] were among the first to recognise the importance of considering a more rigorous treatment of the radiant interaction when modelling investment casting processes. This was later endorsed by Rappaz *et al* [7]. It was realised that the geometrical definition of the models must be extended to include not only the geometry of the casting but also that of the furnace in which the casting is confined.

Dupret *et al* and their predecessors achieved this inclusion quite elegantly for axisymmetric crystal growth furnaces by applying a Galerkin discretisation to a net–radiation analysis of the furnace cavity [15]. Using a similar approach, Hoffman *et al* developed a model of the directional casting process of a single non–axisymmetric component [16, 17]. Their model, however, did not exploit the apparent geometrical symmetries in their furnace cavity.

More recently, clusters of components have been studied [18]–[22]. In many of these studies the abovementioned large computational cost associated with the radiant interaction was confirmed, although not comprehensively addressed. Firstly, in all the studies a net–radiation analysis accounting for the radiant interaction within the furnace cavity was coupled to a standard finite element analysis of solidification within the casting. However, it appears that no special treatment was given to the coupling mechanisms, and to their impact on the overall solution accuracy. Secondly, although planes of geometrical symmetry within both the cluster and furnace was accounted for, it was done so in a computationally intensive manner.

In this thesis the aim is to extend the current capability by paying close attention to both the size and complexity of this computational problem. As above, a standard Galerkin isoparametric finite element model of conduction within the casting is coupled to a net–radiation model applied to the furnace cavity. Specific innovations inherent in this modelling initiative include (listed in order of importance):

- the development of a unique algorithm to couple the finite element calculations to the radiation calculations so that the overall levels of numerical accuracy and stability of the solutions are raised

- the exploitation of planes of geometric symmetry in a manner which dramatically reduces the required number of degrees of freedom without a significant loss of accuracy
- the simulation of the relative motion of the casting and the furnace without requiring the view–factor database to be reconstructed at every time increment
- the development of various pre–processing algorithms to expedite the analyst's task of setting up the computational models

The general purpose finite element code ABAQUS is used as the finite element implicit solver. The radiation calculations described in this thesis are coupled to finite element calculation via recourse to ABAQUS's DFLUX user-subroutine [23]. This exact mechanism for this coupling is discussed in detail in §4.4 of Chapter 4.

The organization of the thesis is as follows:

In Chapter 2 directional investment casting processing is discussed. The process parameters affecting solidification behaviour are identified. In turn, the solidification behaviour is related to the as–cast microstructure by introducing the concepts of the thermal gradient across the mushy zone and the solidus front velocity.

In Chapter 3 a mathematical analysis is developed to describe the conservation of heat energy within the directional casting furnace. It is assumed that energy conservation within the casting is maintained by heat conduction accompanied by a release of latent heat during solidification. A radiation model is developed from first principles to describe the conservation of heat energy at the radiating material boundaries.

A numerical solution is developed in Chapter 4. A Galerkin isoparametric finite element approximation is extended to account numerically for the radiant interactions. The techniques which address the prohibitively large computational cost associated with computing the radiant interactions are comprehensively described.

Aspects of the software implementation are addressed in Chapter 5, with particular emphasis on the efficient organisation and manipulation of the various model data sets.

Finally, results of simulations of various casting processes are presented in Chapter 6. The accuracy of the simulations is checked against experimentally measured data. The specific cost savings that accrue in applying the specialised computational techniques are analysed.

Chapter 2

Directional Investment Casting Technology

2.1 Introduction

Investment casting is not new. Its application can be traced back to the manufacture in China of bronze jewellery dating from 1500 BC [24]. In the early part of this century, the method was applied to the manufacture of gold fillings and dental inlays. By the mid–thirties the technique was regarded as specialised with limited relevance. This situation changed during the Second World War with the increased demand for precision components for armaments and aircraft parts. The pace of development accelerated with the introduction of aircraft gas turbines. The drive to increase engine efficiency through raised operating temperatures prompted the use of investment casting in the production of the turbine blades.

Since their emergence in the 1950s, cast superalloys have found widespread use in gas turbine engines. The steady increase in their use is largely due to the rapid pace of alloy development by the investment casting industry, as well as to improvements in melting and casting process design and practices [4, 25].

From the perspective of alloy development, the high strength of modern superalloys at temperatures close to their incipient melting points derives partly from the existence of both the ordered γ'–particles and various carbides residing in the γ–matrix that act as barriers to deformation[1]. Also, the superalloys have high creep strength resulting from the alignment or elimination of grain boundaries normal to the major stress axis. They have superior thermal fatigue resistance resulting from the existence of low–modulus <001> crystallographic orientation parallel to the solidification direction.

From the perspective of process design, this high elevated–temperature capability is attributable largely to the development of directional solidification (DS) and single–crystal (SC) technolo-

[1] γ and γ' are important metallographic phases which form during the solidification of a number of nickel-based superalloys.

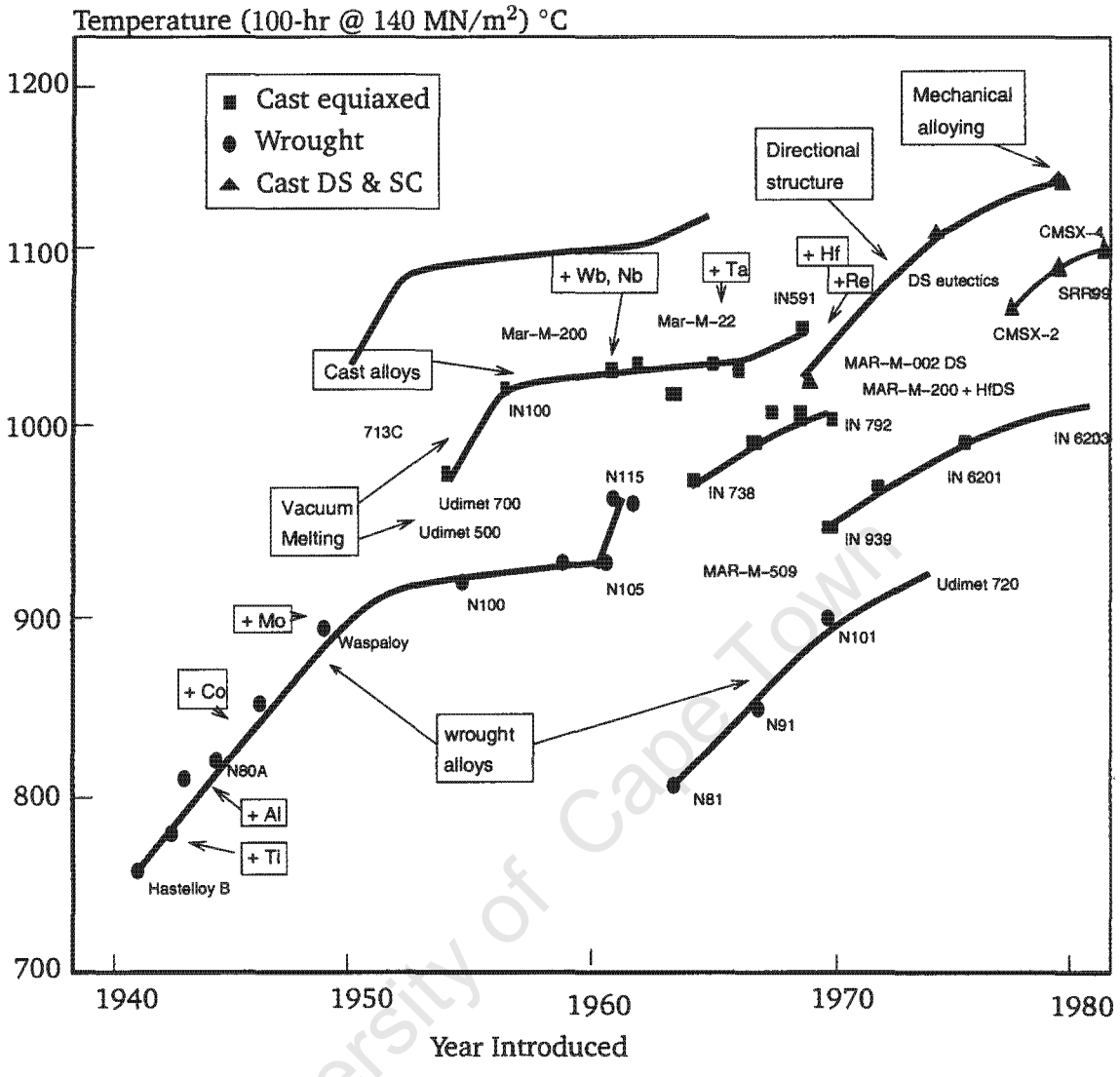

Figure 2.1: Increase in temperature capabability in superalloys [28]

gies, which were first pioneered by Versnyder [26] and Versnyder and Shank [27] also in the late 1950s. The chronological progress in increasing the temperature capability of the alloys is summarised in Figure 2.1 [28], with corresponding developments in the microstructure, shown schematically in Figure 2.2 [25].

How does DS and SC processing contribute to the superior properties of superalloys? The formation of the 'as–cast' microstructure during solidification depends strongly on the manner and rate in which the latent heat of fusion is carried away from the advancing solid–liquid interfaces. In directional solidification, the direction of the thermal gradients in the solidifying metal is constrained to be oriented closely with the longitudinal axis, so that the latent heat of fusion is carried away from the interfaces mainly through the solid. The result is that all microstructural features, such as dentrites, eutectic regions and grain boundaries will tend to be oriented similarly. This will be discussed further in §2.2 and §2.3 in the context of directional

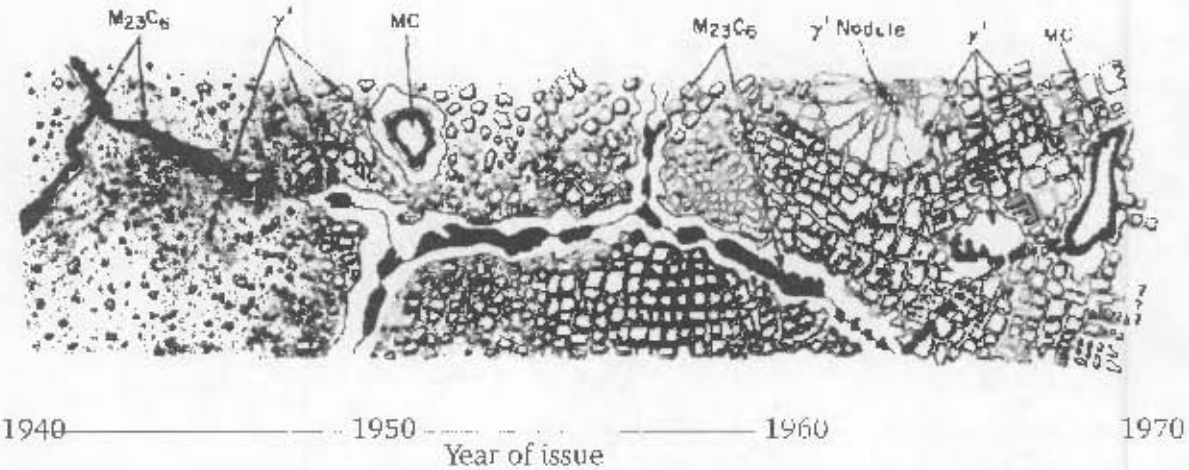

Figure 2.2: Evolution of nickel base superalloy microstructure. Structure shown is heat treated for best rupture properties. Compositions are generalised and typical [25]

casting processing.

2.2 Directional Solidification Processing

Ceramic refractory materials which are used in the construction of the shell mould to contain the solidifying metals were introduced in the mid–1950s. Their introduction facilitated the entry of the industry into the general commercial field because it allowed the range of cast materials to be increased dramatically. To the original alloy steels and superalloys were added carbon steels, tool steels, aluminium alloys, copper alloys, magnesium alloys and more recently titanium alloys.

The principal stages in a typical industrial–type lost–wax investment casting process are shown in Figure 2.3. An expendable wax pattern is made by injecting wax into a metal dye. The wax patterns are then mounted onto a runner system to form an assembly. In the next two stages alternate layers of ceramic slurry and granular material are applied to the assembly until the shell is of the desired thickness. The primary ceramic coating is usually zircon–based, while alumina–silicates are used in subsequent coatings. The wax is then removed by autoclaving and the mould is fired to give full strength and to remove remaining moisture. For superalloy applications the melting and casting is done under vacuum to eliminate contamination of the metal by various gases. After the casting has cooled, the ceramic shell is removed. The runner system is then machined away and the casting is finished to specification.

A typical DS vacuum furnace, as shown in Figure 2.4, consists of three chambers, namely, an induction melting chamber above, a graphite resistance–heating chamber, and a water–cooled chamber below. The ceramic mould assembly resides on a water–cooled chill–plate which is in turn supported by a ram. At the start of the casting process the ram is positioned such that

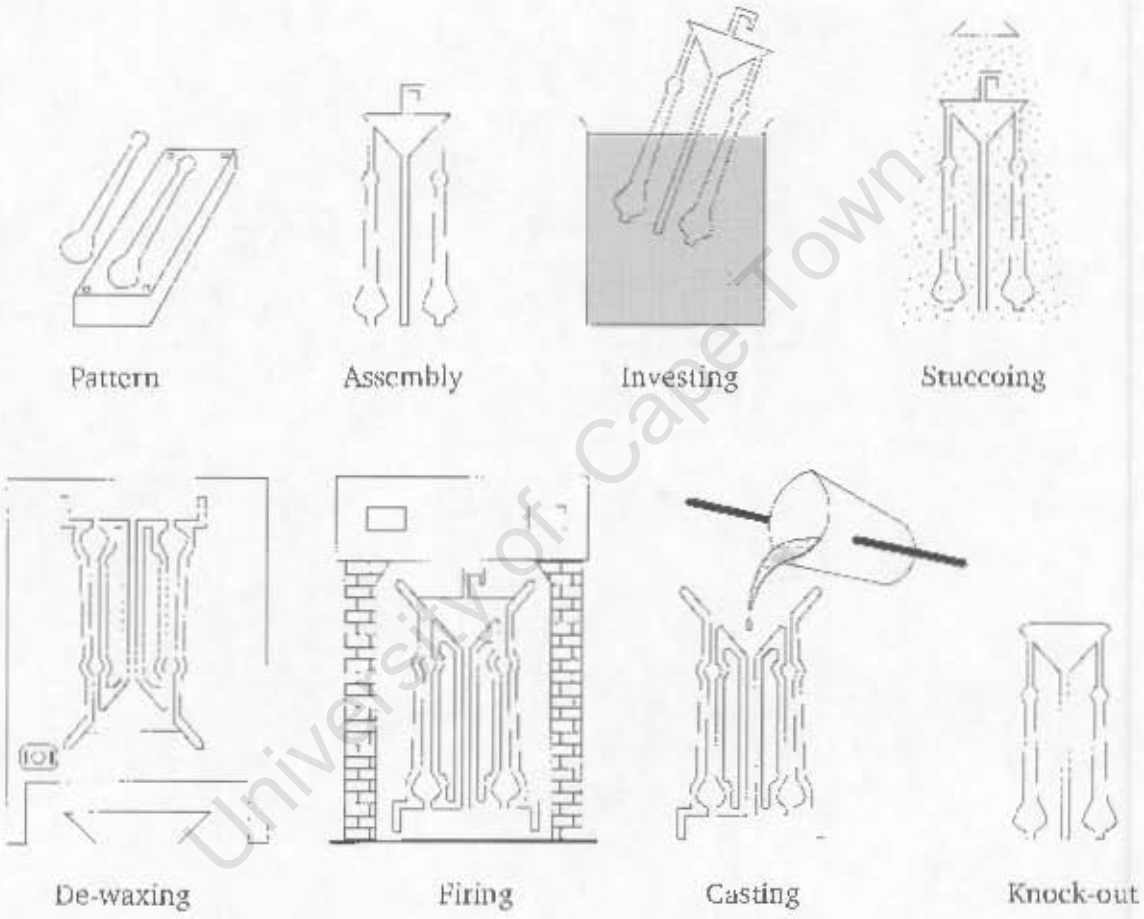

Figure 2.3: Diagram of the 'lost–wax' investment casting process under vacuum conditions

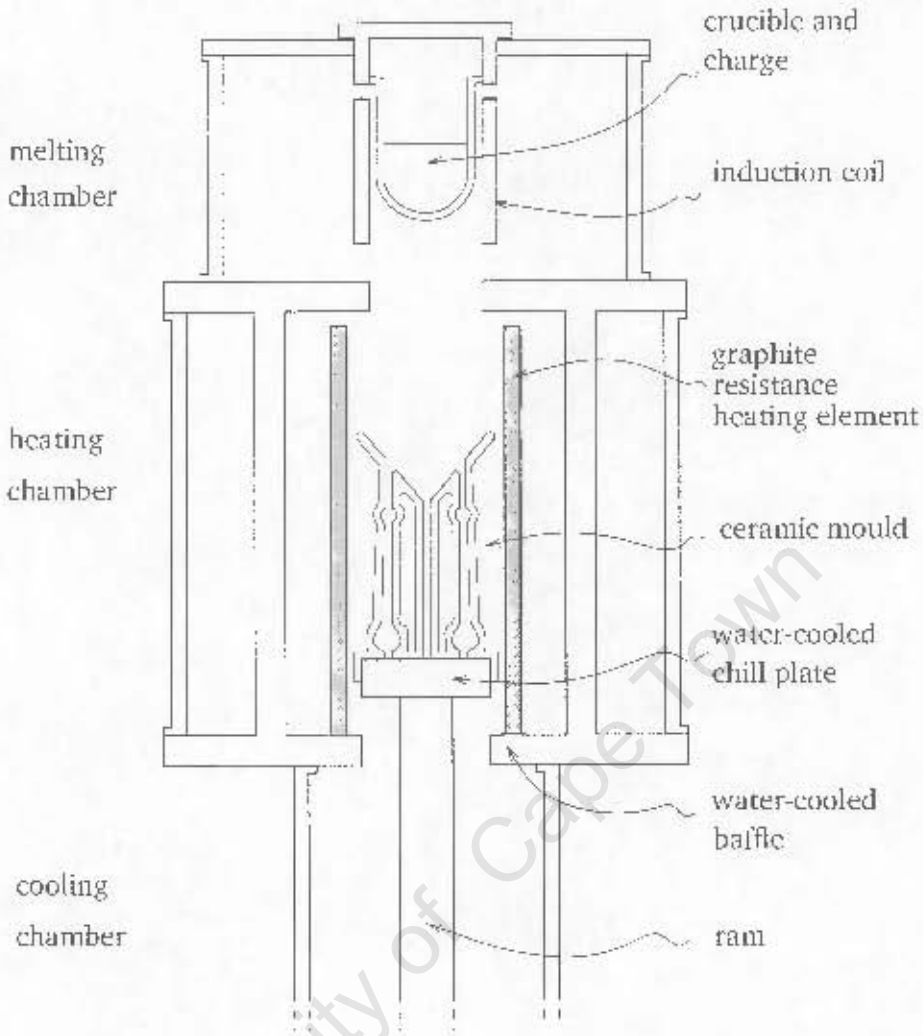

Figure 2.4: Diagram of a directional solidification investment casting process using a shell mould

the shell mould is located in the heating chamber. The molten metal is then poured into the mould, after which the ram is lowered at a carefully controlled rate, moving the metal/mould combination down into the cooled chamber.

Obviously the lower regions of the casting are the first to lose heat, firstly by conduction to the chill–plate and secondly via radiation to the walls of the bottom chamber. As time progresses more of the casting becomes subjected to radiation heat loss to the bottom chamber. Consequently, in the presence of a positive vertical thermal gradient the lower regions of the casting are the first to solidify.

In such a process the parameters that affect the solidification behaviour, and consequently, the as–cast microstructure, are typically:

- the geometry of the casting and of the furnace
- in particular, the diameter of the baffle

- the magnitude of the longitudinal thermal gradient between the heating and cooling chamber
- the temperature of the graphite heaters and walls of the cooling chamber
- the thickness and thermal properties of the ceramic mould
- the number and orientation of individual components that are cast simultaneously
- the casting withdrawal rate

The relative influence of these parameters on the solidification behaviour was studied in detail by Kotschy [11, 29, 30]. As will be discussed below, with respect to as–cast microstructure, the solidification behaviour may be adequately characterised not by the abovementioned processing parameters, but by the magnitudes of the thermal gradients within the solidifying region and the velocity of the phase fronts bounding the solidifying region.

The attractiveness of DS and SC processing is that these intrinsic attributes are correlated more closely with the processing parameters than in the case of equiaxed processing. Firstly, the thermal gradient in a solidifying region of the casting must, by definition, be proportional to the heat flux in the same region (Equation (3.1), §3.2). It was verified by Kotschy that the heat flux in turn depends, for a given metal, on the first six parameters above. Secondly, the solidification velocities in a solidifying region may be loosely correlated with the casting withdrawal rate. Thirdly, both thermal gradient and cooling rate depend strongly on casting geometry.

2.3 Microstructure and Defect Formation

As was implied above, the morphology of microstructural features that form during solidification depends, firstly, on the influence of the thermal field on solute diffusion in the liquid ahead of the solidifying interface [5, 6], and secondly, on the fact that the solute concentration influences the solification temperature—usually lowering the solidification temperature with increasing solute concentration. During solidification, solute material will diffuse into the liquid, resulting in a solute concentration profile in the liquid in front of the solidifying interface. The concentration profile results in a melting temperature profile ahead of the interface.

Plane-front solidification breaks down whenever the thermal gradient ahead of the interface drops below a threshold value. Below this threshold, actual temperatures in the liquid will remain lower than the local melting temperature until the solid phase begins to nucleate. The spatial zone of constitutional instability, in which temperatures are below the local melting temperature, is known as the *mushy zone*, and it is in this zone that microstructural features form which are of interest to us here.

It has been be shown [4, 31] that the nature of the microstructural features may be classified according to the ratio of the thermal gradient, G, in the mushy zone to the solidus front velocity,

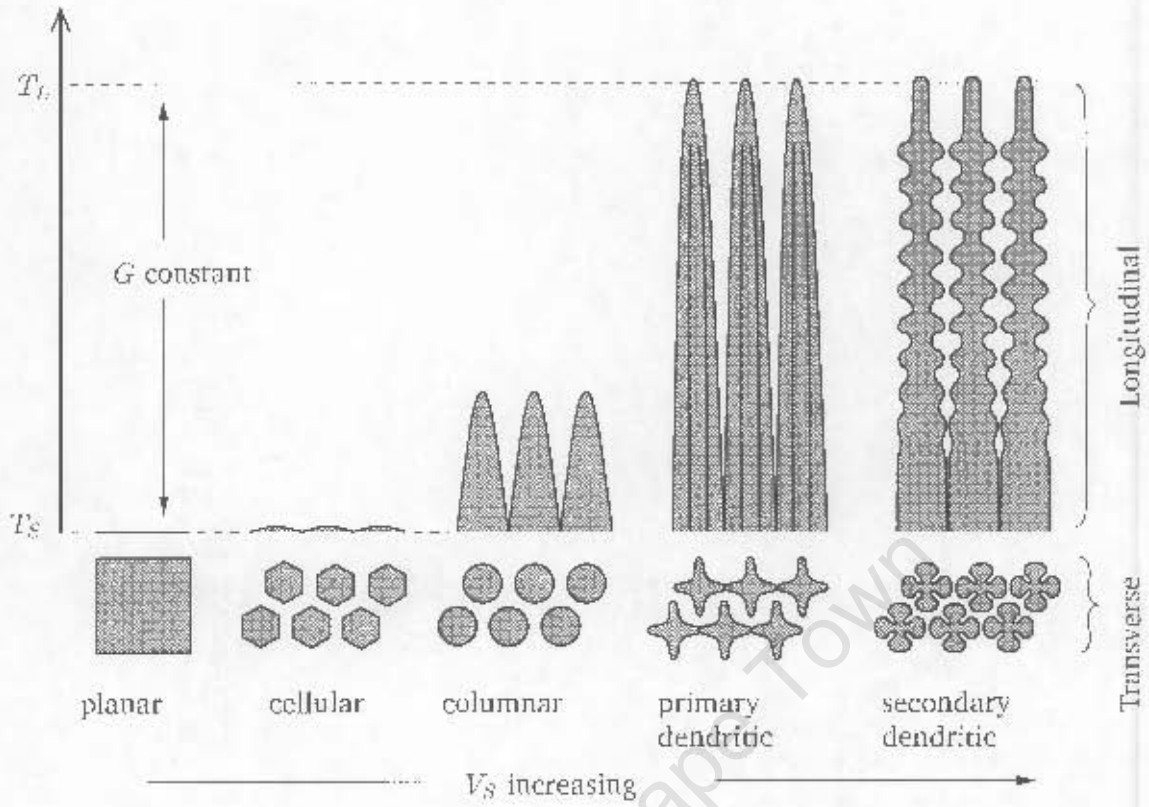

Figure 2.5: Schematic of microstructural morphologies changing with increasing V_S for constant G. T_S and T_L are respectively the solidus and liquidus temperatures bounding the mushy zone [29]

V_S. This is summarised schematically in Figure 2.5. Measured microstructural morphologies obtained with six superalloys that were directionally solidified in a range of conditions with various values of G and V_S are shown in Figure 2.6 [4]. In this figure zones bounded by values of G/V_S are clearly identifiable.

Furthermore, under conditions of dendritic growth it was shown by Burden and Hunt [6] that the spacing between the primary dendrite arms may be related approximately to the function $1/(V_S G^2)^{1/4}$. This formula was verified by Kotschy and Carter [29]. Casting simulations of the directional casting of a superalloy tensile test specimen were compared against experimentally measured results.

With respect to the formation of voids due to shrinkage during solidification, Niyama, *et al* [32, 33], applied a simple Darcy fluid flow model in the interdentritic regions to relate the onset of shrinkage in a casting to a critical value of $(G/V_S)^{1/2}$. Other workers discovered similar relationships (with varying degrees of empiricism) between other microstructural features and values of G and V_S [34, 35, 36, 37].

Equipped with these relationships, a casting modelling programme is able to provide valuable links between microstructure and process design. Indeed, it is now possible to prescribe optimal parameter settings for a given casting geometry such that the desired microstructure is

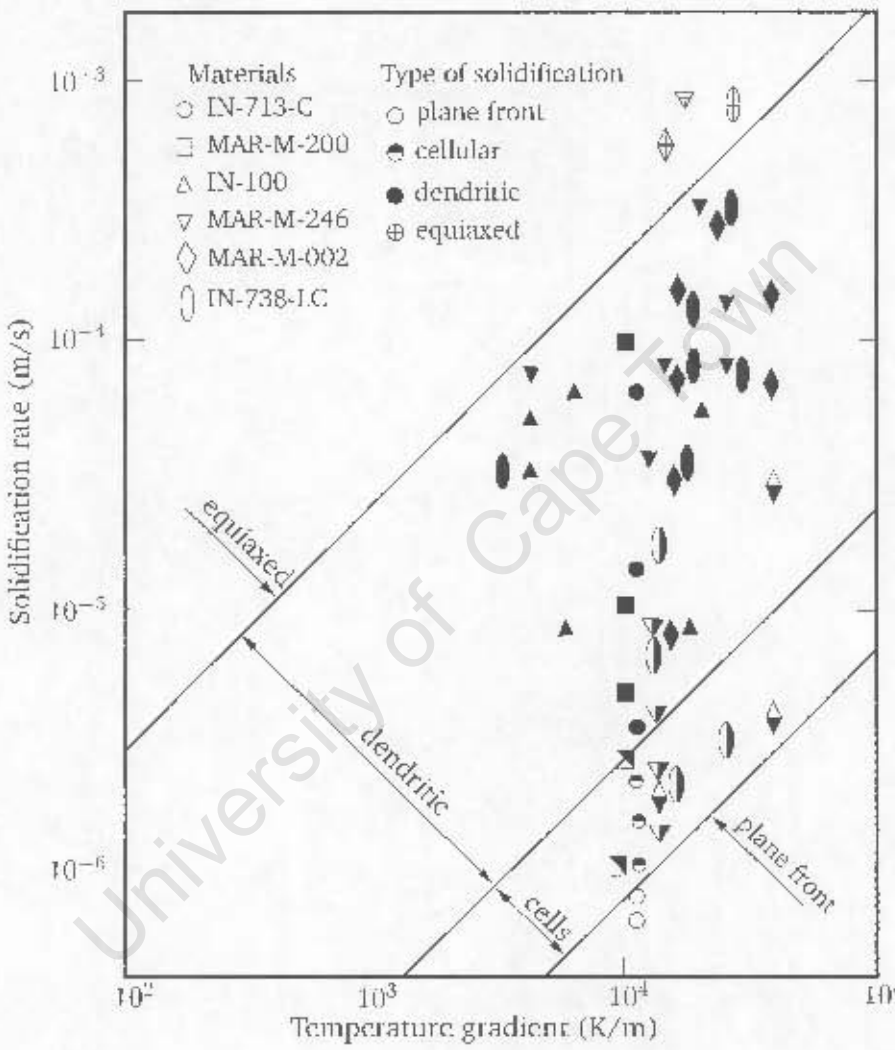

Figure 2.6: Morphologies of directionally solidified superalloys mapped on a plot of $\log(V_S)$ versus $\log(G)$. The lines drawn between the various zones are lines of constant G/V_S [4, p26]

obtained with a minimum number of casting defects and a minimised casting scrap rate. This will be demonstrated in Chapter 6. Of course, this is all true provided that the models which compute these relationships are solveable in reasonable time and are sufficiently accurate.

In the next chapter a mathematical model will be developed which, in the author's view, captures the relevant physical phenomena influencing the casting process, and which will therefore form the basis for the development of computer models which are sufficiently accurate and which may readily be applied to industrial casting processes.

2.4 Summary

The widespread use of cast superalloys is largely attributable both to the rapid pace of alloy development and to improvements in melting and casting process design and practices. With respect to process design, the directional and 'single-crystal' investment casting processes have contributed significantly.

In this chapter the directional (and 'single-crystal') casting process was described in some detail. Specific processing parameters which influence the solidification behaviour—which in turn influences the nature of the as-cast microstructure—were identified.

Much of the character of the as-cast microstructure may be related to the solification behaviour via both the thermal gradient across the mushy zone and the solidus front velocity. In particular, the spacing between the primary dendrite arms and the formation of voids due to macro-shrinkage was related to specific functions of the gradient and the velocity. Such relationships provide valuable links between the as-cast microstructure and the process design and practice.

Chapter 3

Mathematical Model

3.1 Introduction

Casting is a multiphysics process. A complete macroscopic description of casting must account for the conservation of mass, heat energy, momentum and solute species [38, 39, 40]. To simulate the casting process, the analyst must in general address the following: (1) the fluid flow during the initial mould filling, (2) the evolution of latent heat during solidification, (3) the exchange of heat energy between the casting, the mould, and the surrounding environment by radiation and convection, (3) convection–driven mass currents originating from thermal gradients in the liquid metal, (4) thermal impedance layers that form between neighbouring materials after solidification, (6) macro-segregation, (6) the formation of as–cast microstructural features, and (5) the formation of macro– and micro–porosity voids in the casting.

As a simplification, in this thesis the effects of fluid flow and convection in the liquid are neglected. Solidification during directional investment casting processing occurs relatively slowly and in a controlled manner with conduction and radiation being the dominant heat transfer modes.

In developing the mathematical model it is assumed that, with the exception of the release of latent heat of fusion, heat energy is conserved within the casting. This conservation is maintained by conduction heat transfer. The latent heat of fusion is associated with solidification of the metal during cooling. This latent heat is assumed to be released evenly throughout the temperature range bounded by the solidus and liquidus temperatures. In addition, conservation at material boundaries is maintained, firstly by radiation heat transfer between the casting and the furnace, and secondly, by conduction between the casting and the chill plate supporting the casting (Figure 2.4).

Because of their profound influences on the process, a thorough analysis of both the latent heat of fusion released during solidification and the radiation at the material boundaries is developed in this work. In both cases the analysis begins from first principles, because doing so will help both to communicate adequately the simplifying assumptions which were invoked,

and to place this macroscopic treatment in the correct context within the temporal and spatial scales.

The mathematical description of conduction heat transfer follows that of Özisik [41], together with others for the treatment of solidification. The foundational description of radiation heat transfer follows that of Siegel and Howell [42].

3.2 Heat Balance within the Solidifying Casting

Throughout this analysis it is assumed that the solidifying casting, the ceramic mould, the chill plate and the investment casting furnace are comprised of homogeneous, isotropic solids with possible sources of internal heat generation. This assumption is valid in the case of metal investment casting processes. In directional casting processes the liquid metal is typically allowed to stabilise after being poured into the mould cavity. Turbulent and laminar fluid flow of the molten metal above the solidifying fronts are therefore not considered. However, it must be noted that casting comprises a complex interplay between various effects, and a more detailed study of it at smaller scales must account for this fluid flow.

3.2.1 Conduction

The transfer of heat energy from hotter regions in the casting to cooler regions cannot be measured directly. But the concept of heat still has physical meaning because it is related to the measurable scalar quantity called temperature. Once a temperature distribution, $T(\mathbf{x}, t)$, within a body is determined as a function of position and time, the flow of heat in the body may be computed from laws relating heat flow to the temperature gradient [41].

At the microscopic level the transfer takes place from more energetic molecules to less energetic ones. In the case of gases the more energetic molecules, being in constant and random motion, periodically collide with molecules of a lower energy level and exchange kinetic energy and momentum. In liquids the molecules are more closely spaced than in gases, but the molecular energy exchange process is qualitatively similar to that in gases. In electrically non–conducting solids, heat is conducted by lattice waves caused by atomic motion. In electrically conducting solids, the principal contribution to the energy transfer is that due to the motion of free electrons.

These underlying microscopic processes give rise at a macroscopic level to heat transfer by conduction, where heat is transfered from one part of a body at a higher temperature to another part at a lower temperature. At a macroscopic level the basic law that relates the heat flow and this temperature gradient is generally known as Fourier's law, after the French mathematical physicist Joseph Fourier [43]. For a homogeneous, isotropic solid the law is given in the form

$$\mathbf{q}(T, \mathbf{x}, t) = -k(T, \mathbf{x}, t) \frac{\partial T(\mathbf{x}, t)}{\partial \mathbf{x}} \tag{3.1}$$

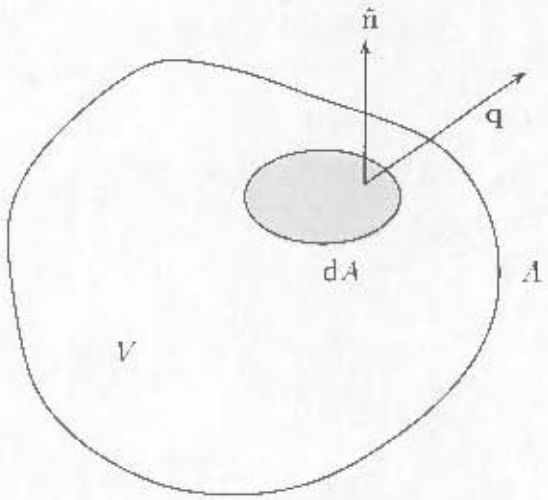

Figure 3.1: Nomenclature for the derivation of the heat conduction equation

where the temperature gradient is a vector normal to the isothermal surface. The heat flux vector, $\mathbf{q}(T, \mathbf{x}, t)$, represents heat flow per unit time per unit area of the isothermal surface in the direction of the decreasing temperature. The positive scalar proportionality constant, $k(T, \mathbf{x}, t)$, is the thermal conductivity and is assumed to be a characteristic of the material. Since the vector $\mathbf{q}(T, \mathbf{x}, t)$ points in the direction of decreasing temperature, the minus sign is included in (3.1) to make the heat flow a positive quantity.

For a small control volume, V, as shown in Figure 3.1, the energy balance may be stated as [41]

$$\begin{bmatrix}\text{rate of heat entering}\\ \text{through the bounding}\\ \text{surfaces of } V\end{bmatrix} + \begin{bmatrix}\text{rate of energy}\\ \text{generation}\\ \text{in } V\end{bmatrix} = \begin{bmatrix}\text{rate of storage}\\ \text{of energy}\\ \text{in } V\end{bmatrix} \tag{3.2}$$

The terms are evaluated as:

$$\begin{bmatrix}\text{rate of heat entering}\\ \text{through the bounding}\\ \text{surfaces of } V\end{bmatrix} = \int_A \mathbf{q}\cdot\hat{\mathbf{n}}\,\mathrm{d}A = -\int_V \frac{\partial \mathbf{q}}{\partial \mathbf{x}}\,\mathrm{d}V \tag{3.3a}$$

where A is the surface area bounding the volume element V, $\hat{\mathbf{n}}$ is the outward–drawn normal unit vector to the surface $\mathrm{d}A$. The minus sign is included to ensure positive heat flow into the volume element V. The divergence theorem is used to convert the surface integral to a volume integral [44].

$$\begin{bmatrix}\text{rate of energy}\\ \text{generation}\\ \text{in } V\end{bmatrix} \int_V \rho_m(T, \mathbf{x}, t)\, C_p(T, \mathbf{x}, t)\frac{\partial T(\mathbf{x}, t)}{\partial t}\,\mathrm{d}V \tag{3.3b}$$

$$\begin{bmatrix}\text{rate of energy}\\ \text{generation}\\ \text{in } V\end{bmatrix} = \int_V g(T, \mathbf{x}, t)\,\mathrm{d}V \tag{3.3c}$$

As denoted, the mass density, ρ_m, the specific heat capacity, C_p, and the volumetric heat generation, g, may all depend on $T(\mathbf{x}, t)$, $\mathbf{x}$ and t. Substituting (3.3) into (3.2) yields the energy conservation equation applicable over the entire control volume

$$\int_V \left[-\frac{\partial \mathbf{q}}{\partial \mathbf{x}} + g - \rho_m C_p \frac{\partial T}{\partial t} \right] dV \quad 0 \tag{3.4}$$

Equation (3.4) is derived for an arbitrarily small volume element V in the solid. Hence the volume may be made arbitrarily small allowing the integral to be removed:

$$\frac{\partial \mathbf{q}}{\partial \mathbf{x}} + g = \rho_m C_p \frac{\partial T}{\partial t} \tag{3.5}$$

Substituting $\mathbf{q}(\mathbf{x}, t)$ from (3.1) into (3.5), the differential equation for heat conduction for a stationary, homogeneous, isotropic solid with heat generation within the solid is

$$\frac{\partial}{\partial \mathbf{x}} \cdot \left(k \frac{\partial T}{\partial \mathbf{x}} \right) + g = \rho_m C_p \frac{\partial T}{\partial t} \tag{3.6}$$

By constraining the heat generation term to have a certain form, this conservation equation, together with a set of boundary and initial conditions (§3.3 and §3.4) allows for the prediction of the temperature evolution within the casting, and hence, using (3.1), for the prediction of the heat flux at all points within the body and at all times.

Non–linearities may be present in this description if any of the quantities k, g, ρ_m or C_p in the above differential equation depend on temperature T, or if the boundary or initial conditions are non–linear with respect to temperature or geometry. A further non–linearity in the formulation arises if the body is undergoing a change of phase, such as in the case of solidification. This source of non–linearity will be discussed in more detail below.

3.2.2 Solidification during Casting

Solidification involves the release of latent heat within the solidifying body at all material points undergoing a change of phase. In the case of pure substances, the solidification takes place at a discrete temperature, and the solid and liquid phases are separated by a sharp moving interface. In the case of mixtures and impure materials, such as superalloys, the solidification takes place over an extended temperature range, and as a result, the solid and liquid phases are separated by a two–phase moving region, commonly known as the mushy zone.

Early work in deriving analytic solutions to problems involving a change of phase included those by Lam and Clapeyron [45] in 1831 and by Stefan [46] in 1891. The fundamental nature of this type of problem (known as a Stefan problem) is that the phase–change boundaries are both unknown and moving, and that the parabolic heat conduction equation (3.6) is to be solved in regions whose boundaries are also to be determined. This presents another source of non–linearity in addition to that which may appear in specifying the boundary and initial conditions of Equation (3.6).

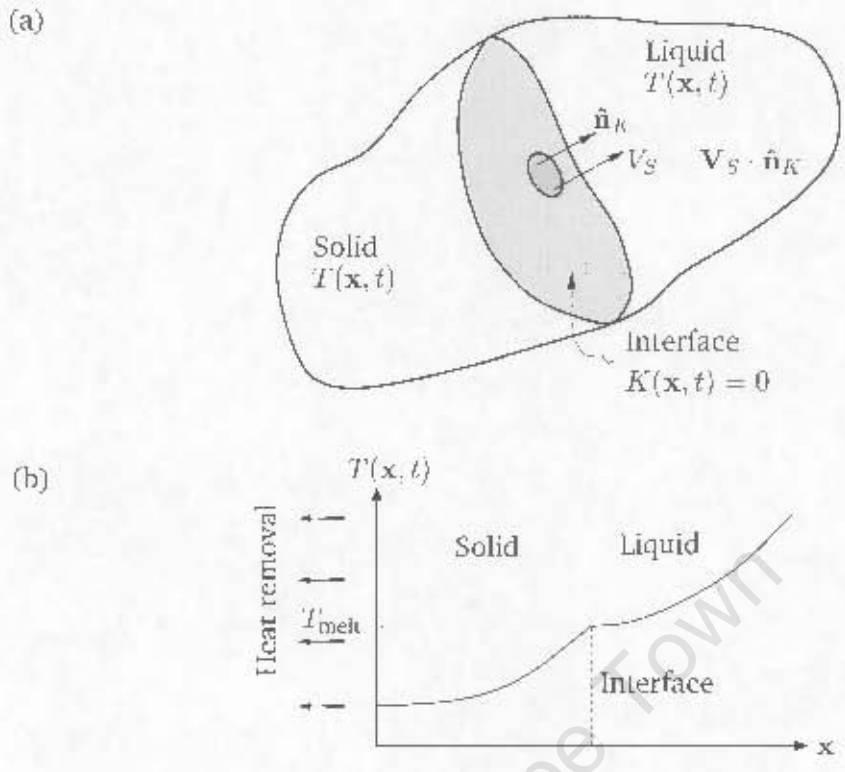

Figure 3.2: (a) Solidification showing interface moving in direction $\hat{\mathbf{n}}$, (b) Typical temperature distribution in neighbourhood of a point on the solidifying interface

Over the years much attention has been given to finding analytic solutions. The so–called integral method was applied by Goodman [47, 48] and many others [49]–[52] to solve one–dimensional transient phase–change problems. Other techniques have included the use of Green's functions [53, 54], perturbation methods [55, 56], the embedding technique [57]–[59], and a variable eigenvalue approach [60]. The disadvantage of these formulations, however, is that they do not lend themselves well to the quest for numerical solutions of problems in which solidification does not take place at a unique temperature.

In an alternative (albeit equivalent) approach, the liberation of heat during solidification is treated as a moving planar heat source located at the solid–liquid interface. The transient two–domain phase–change problem is cast in the form of a single transient heat conduction problem applied to a single domain which now includes both solid and liquid material [61, 62] as shown in Figure 3.2.

The moving heat source in (3.6) is written as $\rho_m L V_S \delta(\mathbf{x} - \mathbf{x}_K)$, where L (in units J/kg) is the latent heat of fusion per unit mass of the material, V_S is the normal speed of the interface, and δ is Dirac's distrubutional functional.[1] The quantity $\mathbf{x}_K(\mathbf{x}, t)$ is some point on the (as yet unknown) solid–liquid surface interface $K(\mathbf{x}, t) = 0$ such that the vector $(\mathbf{x} \quad \mathbf{x}_K)$ is

[1] In the early period of quantum mechanics, P.A.M. Dirac introduced the distribution functional, $\delta(x)$, which on its own did not have well—efined values, but when occurring as part of an integrand, the value of the integral could be well defined [63, 64]. It was defined such that $\int_{-\infty}^{\infty} \delta(x)\, dx = 1$ so that $\int_{-\infty}^{\infty} \delta(x - a)\, \phi(x)\, dx = \phi(a)$

perpendicular to the interface. Therefore from (3.6)

$$\frac{\partial}{\partial \mathbf{x}} \cdot \left(k \frac{\partial T}{\partial \mathbf{x}} \right) + \rho_m L V_S \, \delta(\mathbf{x} - \mathbf{x}_K) = \rho_m C_p \frac{\partial T}{\partial t} \qquad \forall \, \mathbf{x} \text{ in } V \tag{3.7}$$

And on the interface

$$T(\mathbf{x}, t) = T_{\text{melt}} \qquad \forall \, (\mathbf{x}, t) \quad \text{in} \quad V \quad \text{s.t.} \quad K(\mathbf{x}, t) = 0 \tag{3.8}$$

where T_{melt} is the melting temperature. In a variant of this single-domain approach a new independent variable, called the enthalpy, H, is introduced as the sum of the 'sensible' and the latent heats per unit volume[65, 66]. For Stefan problems in which the material undergoes a discrete change of phase, the enthalpy is defined as

$$H(T) \equiv H(T_{\text{ref}}) - \int_{T_{\text{ref}}}^{T} \rho_m C_p(\tau) \, \mathrm{d}\tau + \rho_m L \, S(T - T_{\text{melt}}) \tag{3.9a}$$

where

$$S(x) = \begin{cases} 0 & \text{if } x < 0, \\ 1 & \text{if } x \geq 0 \end{cases} \tag{3.9b}$$

and T_{ref} is some reference temperature at which the enthalpy is known.

Assuming that there exist no other sources of heat generation other than the release of latent heat, the differential equation of energy conservation (3.6) for a body undergoing a change of phase may then be written as

$$\frac{\partial}{\partial \mathbf{x}} \cdot \left(k(T(\mathbf{x}, t), \mathbf{x}, t) \, \frac{\partial T(\mathbf{x}, t)}{\partial \mathbf{x}} \right) = \frac{\partial H(T(\mathbf{x}, t)}{\partial t} \qquad \forall \, \mathbf{x} \text{ in } V \tag{3.10}$$

For a material undergoing a discrete phase change, Equation (3.10) is equivalent to (3.7). Because $H(T)$ is defined as a unique function of temperature

$$\frac{\partial H}{\partial t} = \frac{\mathrm{d}H}{\mathrm{d}T} \frac{\partial T}{\partial t} = \rho_m (C_p - L \, \delta(T - T_{\text{melt}})) \frac{\partial T}{\partial t} \tag{3.11}$$

and recognising that

$$-V_S \, \delta(|\mathbf{x} - \mathbf{x}_K|) = \frac{\partial T}{\partial t} \, \delta(T - T_{\text{melt}}) \tag{3.12}$$

the equivalence follows.[2]

This single-domain approach extends naturally to casting processes in which solidification takes place no longer at a discrete temperature, T_{melt}, but rather in a mushy zone bounded by a solidus temperature, T_S, and liquidus temperature, T_L. In the mushy zone the transition from liquid to solid takes place gradually, with no apparent sharp interface.

[2] The '$-$' sign must be included because the rate $\partial T/\partial t$ is negative as the interface moves into the cooling liquid.

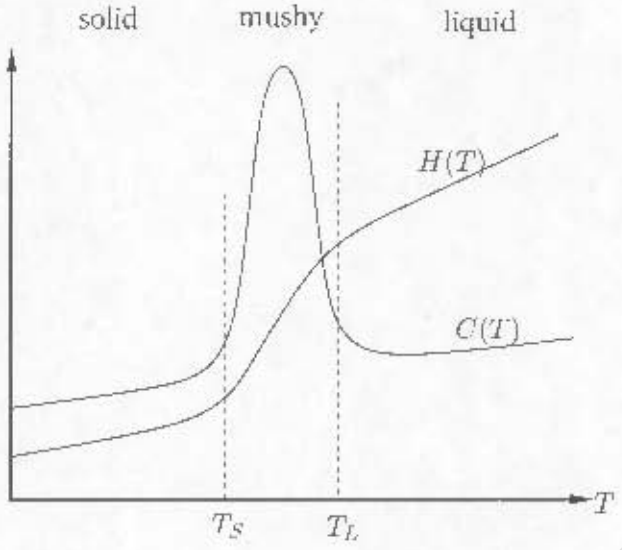

Figure 3.3: Typical variation of heat capacity and enthalpy over the mushy zone

For a material in which the change of phase takes place in a mushy zone, $[T_S, T_L]$, the enthalpy may be defined as

$$H(T) = \begin{cases} \displaystyle\int_{T_{\text{ref}}}^{T} \rho_m C_p(\tau)\,\mathrm{d}\tau & T < T_S, \\ \displaystyle\int_{T_{\text{ref}}}^{T_S} \rho_m C_p(\tau)\,\mathrm{d}\tau + \int_{T_S}^{T} \rho_m \left(\frac{\mathrm{d}L(\tau)}{\mathrm{d}\tau} + C_s(\tau) \right) \mathrm{d}\tau & T_S < T < T_L, \\ \displaystyle\int_{T_{\text{ref}}}^{T_S} \rho_m C_p(\tau)\,\mathrm{d}\tau + \rho_m L + \int_{T_S}^{T_L} \rho_m C_s(\tau)\,\mathrm{d}\tau & \\ \qquad + \displaystyle\int_{T_L}^{T} \rho_m C_p(\tau)\,\mathrm{d}\tau & T \geq T_L \end{cases} \tag{3.13}$$

The quantity $C_s(T)$ is the 'sensible' specific heat capacity in the interval $[T_S, T_L]$ excluding the latent heat. It will be assumed from now on that $H(T_{\text{ref}}) = 0$. A typical variation of the heat capacity and the enthalpy is shown in Figure 3.3. The latent heat will now be assumed to be released evenly throughout the mushy zone so that

$$\frac{\mathrm{d}L(T)}{\mathrm{d}T} = \frac{\Delta L}{T_L - T_S} \quad \text{for } T_S \leq T < T_L, \tag{3.14}$$

Application of single–domain approaches in numerical methods has found popularity owing to the simple representation of latent heat [67] and to their ease of implementation in existing software programs. However, in the case of discrete phase changes, the presence of the Dirac–delta function [56] results in stiff numerical systems, and the presence of a discontinuity in

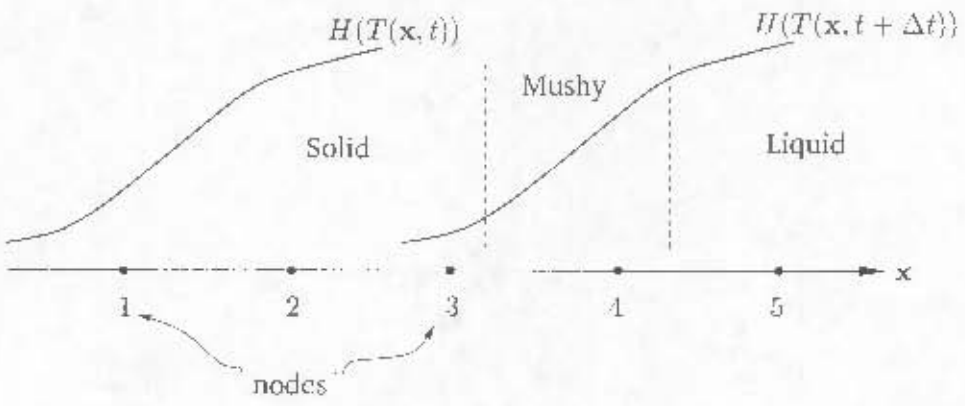

Figure 3.4: Variation of enthalpy, $H(T(\mathbf{x},t))$, where the time increment, Δt, is too large. The mushy zone bypasses integration points 2 and 3 entirely

the heat generation term becomes difficult to follow numerically. It requires firstly that the δ–functional be replaced with some finite–valued function peaking at the melting point, T_{melt}, and secondly that the discretization parameters be kept small in both time and space.

If the spacing between two adjacent integration points (see §4.2.5), $|\Delta \mathbf{x}|$, is larger than the width of the mushy zone, then the interpolation (4.5) may miss the phase change over part of the element (see §4.2.5). Furthermore, a phase change at a point may be missed if the distance travelled by the mushy zone in one time increment, Δt, is greater than the width of the mushy zone itself (Figure 3.4). This imposes a restriction on the time increment as

$$\Delta t < \frac{|\Delta \mathbf{x}|}{V_S} \tag{3.15}$$

The single–domain approach of (3.10) and (3.13) will be used in Chapter 4 when a finite element solution strategy is developed. However, before this can be done it is necessary to describe the manner in which the solidifying casting exchanges heat energy with the surrounding furnace.

3.3 Heat Balance at the Casting's Bounding Surfaces

The energy balance equation (3.10) (or (3.6)) predicts the evolution of temperature at all internal material points. However, on its own it does not predict conditions either at external boundaries, such as the outer surface of the ceramic mould, or at internal boundaries, such as between the solidified metal and the ceramic shell where a thermal boundary may form as a result of metal shrinkage during cooling. Indeed, if extra rules applied at such boundaries are not included in the mathematical model, either in the form of temperature prescriptions or heat energy balances, then (3.10) will have infinitely many solutions.

For the purpose of this analysis, a casting material boundary will be defined as a surface either

on which the temperature evolution is prescribed, or across which heat energy is transferred by some mechanism other than by point continuous conduction.

If the temperature is prescribed on a boundary surface, S_I, then the general form is

$$T = T_I(\mathbf{x}, t) \qquad \forall\, \mathbf{x} \text{ on } S_I \tag{3.16}$$

If the actual temperature is not known on a boundary surface, S_R, then a heat energy balance must be provided at the surface. The heat flux in the material at a point on S_R is equated with a flux outside the material in a vanishing neighbourhood around the same point:

$$\mathbf{q} \cdot \hat{\mathbf{n}}|_{S_R} = \left(-k\frac{\partial T}{\partial \mathbf{x}}\right)_{S_R} \cdot \hat{\mathbf{n}} \equiv q_R(T, \mathbf{x}, t) \qquad \forall\, \mathbf{x} \text{ on } S_R \tag{3.17}$$

The vector, $\hat{\mathbf{n}}$, is the outward–pointing normal at the point $\mathbf{x}$ on S_R . The heat transfer mechanism for the flux, q_R, must be known beforehand.

If the flux q_R depends on the surface temperature, T, (or worse still, on the temperature at other regions in the furnace) then (3.10) and (3.17) are coupled and non–linear, and a solution can therefore only be found in a self–consistent manner. Electromagnetic radiant energy exchange at the boundary depends on the fourth power of the absolute surface temperature, and is therefore non–linear.

3.3.1 Radiant Interaction Between the Casting and the Furnace

During vacuum investment casting, the transfer of energy between the casting and the furnace walls is dominated by radiation. Before the molten metal is poured into the mould cavity, the pressure in the furnace chamber is reduced in order to eliminate possible contamination of the solidifying superalloy by certain reactive gases. This near–vacuum condition in the chamber has the effect of reducing the contribution of convection heat transfer at all surfaces within the chamber, thereby leaving radiation as the dominant mode.

As described in Chapter 2, the chill plate on which the casting rests is constrained to move relative to the furnace chamber. This in turn affects the radiant interactions that take place in the chamber. As was discussed in §2.2 (and with (3.17)), it is indeed this effect which characterises in part the solidification behaviour in the casting.

In order to develop a reliable and predictive computer model that may be applied to directional investment casting processes of an industrial nature, the simulation of these time–dependent three–dimensional radiant interactions must be addressed. In addition, these simulations must be coupled to calculations of time–dependent heat conduction within the casting. It is the coupling of these two heat transfer mechanisms, in a solution strategy that is readily accessible to the foundry engineer, that is central to this work and to which this thesis is directed.

Since (3.10) and (3.17) are now coupled and non–linear, the pursuit of analytical solutions has been found to be feasible only in situations in which the casting geometry is simple [68].

Numerical solutions are therefore sought. In this section the foundation is laid for the development in Chapter 4 of such a numerical solution using a zonal method.

In the context of energy exchange taking place within the casting furnace, the radiating body is considered as the union of: the casting and shell combination; the furnace chamber walls; the graphite furnace heating elements; and the baffle plates separating the hot and cold zones (Figure 2.4 of §2.2). The union of the exterior surfaces of these components will be said to form a radiating cavity.

In such a cavity three types of processes take place simultaneously, namely: the emission of radiant energy from a surface element; the absorption of part of the incident energy emitted from other surfaces; and the reflection of the remaining part of the incident energy. Energy transmittance is neglected since all materials are assumed to be opaque. I judge this assumption also to be valid for the shell mould which contains a porous structure. Being at least $\frac{1}{2}$cm thick, any radiation being transmitted at a microscale will quickly be completely absorbed.

the shell mould contains a porous structure which infers radiation at the microscale leading to energy transmission by radiation through the shell.

In the next three subsections important concepts of intensity, emissive power, emissivity, absorptivity and reflectivity will be discussed. The diffuse–grey approximation will be developed and its use will be motivated to derive a formula for the radiant contribution to the flux, q_R, in Equation (3.17).

The analysis will start with fundamental quantities of radiation intensity which in general must depend on both the wavelength and the solid angle at which the radiation is emitted or received. Since q_R in (3.17) is assumed to depend on neither of these two, I shall seek to work ultimately with quantities for which such dependencies are integrated out.

Throughout the analysis a prime (') denotes a scalar radiant quantity which varies with solid angle, i.e., depends on direction. A subscript (λ) denotes dependance on wavelength. To simplify the notation, functional dependance on $\mathbf{x}$ and t are only written explicitly from §3.3.5 onwards.

3.3.2 Radiation from a Blackbody

In order to quantify radiant interactions in a cavity comprised of many real surfaces, it is necessary to first understand the nature of the radiation emitted from a single ideal surface — the surface enclosing a blackbody.

A blackbody is defined as one which perfectly absorbs the incident radiation at all wavelengths and at all angles of incidence [42]. As a perfect absorber it serves as a standard reference against which real absorbers and emitters can be compared.

The spectral intensity, $i'_{\lambda b}$, of a blackbody is defined as the energy leaving a black surface per unit time per unit wavelength, $d\lambda$, around λ and per unit projected surface area, dA_p, normal

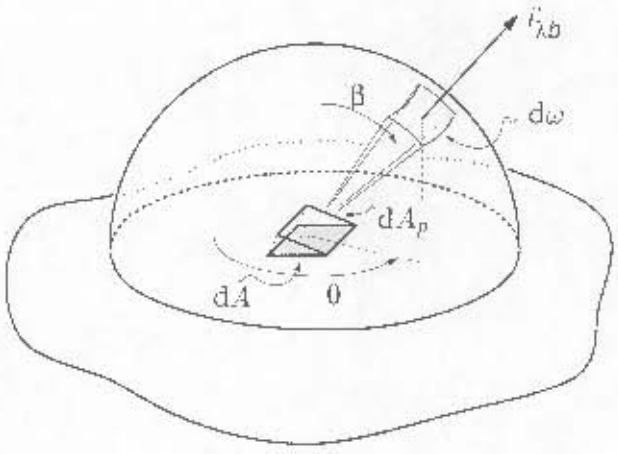

Figure 3.5: Geometric parameters used to characterise radiant energy transfer into solid angle $d\omega$

to the (β, θ) direction and into a unit solid angle centered around the direction (β, θ). This is shown schematically in Figure 3.5. Since the intensity is defined per unit projected surface area, dA_p, its value for a blackbody surface does not depend on the angle, β, at which the energy is emitted.

At the turn of the century it was shown by Max Planck [69] that for a blackbody, the spectral intensity, $i'_{\lambda b}$, in a vacuum is related to the blackbody temperature and wavelength by

$$i'_{\lambda b}(\lambda, T) = \frac{2C_1}{\lambda^5 (\exp(C_2/\lambda T) - 1)} \tag{3.18}$$

where C_1 and C_2 are constants, and the temperature is measured as the absolute temperature.

The directional spectral emissive power, $e'_{\lambda b}$, is defined similarly to $i'_{\lambda b}$ except that the definition is per unit surface area, dA, and not per unit perpendicular surface area, dA_p. By definition then,

$$e'_{\lambda b}(\lambda, \beta, T) = i'_{\lambda b}(\lambda, T)\cos(\beta) \tag{3.19}$$

Clearly $e'_{\lambda b}$ now depends on the angle of emission, β, and varies as $\cos(\beta)$.

To obtain the blackbody emission passing through the entire hemisphere above a surface, (3.19) is integrated over all solid angles, $d\omega = \sin(\beta)d\beta d\theta$, to give the hemispherical spectral emissive power as

$$e_{\lambda b}(\lambda, T) = i'_{\lambda b}(\lambda, T)\int_{\theta=0}^{2\pi}\int_{\beta=0}^{\pi/2}\cos(\beta)\sin(\beta)\,d\beta\,d\theta = \pi i'_{\lambda b}(\lambda, T) \tag{3.20}$$

Combining (3.19) and (3.20) gives a useful relationship

$$e'_{\lambda b}(\lambda, \beta, T) = \frac{\cos(\beta)}{\pi} e_{\lambda b}(\lambda, T) \qquad \text{for } 0 \le \beta < \pi/2 \tag{3.21}$$

To find the total emissive power, $e_b(T)$, for a blackbody, (3.20) is integrated over all wavelengths, using (3.18) and as shown in Figure 3.6:

$$e_b(T) = \int_0^\infty e_{\lambda b}\,d\lambda = \int_0^\infty \frac{2\pi C_1}{\lambda^5 (\exp(C_2/\lambda T) - 1)}\,d\lambda \tag{3.22}$$

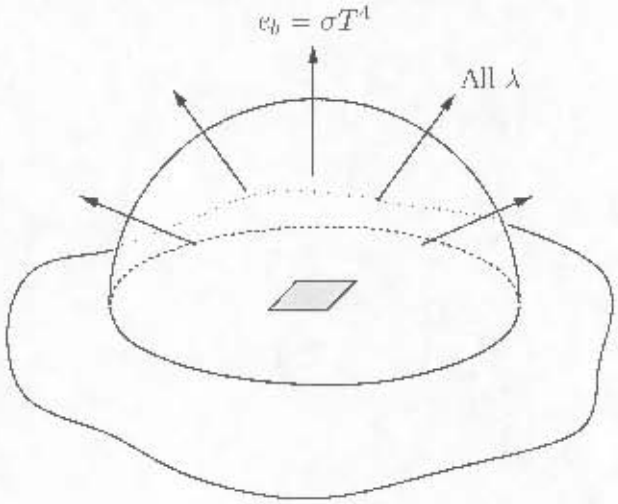

Figure 3.6: Emission, e_b, including all wavelengths, into hemispherical solid angle per unit surface and unit time

This integral can be evaluated analytically to give a surprisingly simple result, known as the Stefan–Boltzmann law:

$$e_b(T) = \sigma T^4 \tag{3.23}$$

where $\sigma = 5.729 \times 10^{-8}$ $\mathrm{Wm^{-2}K^{-4}}$ is the Stefan–Boltzmann constant. The dependence of radiation on wavelength has been removed from the total emissive power, e_b, in (3.23).

It is apparent from reading the work of others that this law (together with (3.28)) is often incorrectly applied to characterise radiation from two or more non–black surfaces [70, 71]. This law applies strictly only to a single blackbody at temperature T, emitting radiation to its environment at a temperature equal to absolute zero. Therefore, on its own it clearly cannot be applied in this work.

3.3.3 Radiation from a Real Non–Blackbody

The ability of a real non–blackbody to emit radiant energy from its surface, and the proportion of incident energy the body can absorb both depend on [42]:

- properties intrinsic to the material itself
- the texture and nature of the surface
- the surface temperature
- the angle at which energy is being emitted and received
- the wavelength of the emitted and received energy

A convenient way of characterizing the radiant energy emitted from a real non–blackbody is by referring to quantities which are defined for blackbodies. To this end a directional spectral emissivity, ϵ'_λ, is defined as the ratio of the emissive ability of the real surface at a temperature, T, to that of a blackbody at the same temperature.

Consider the geometry in the vicinity of a surface which is emitting radiation, as shown in Figure 3.5. The energy emitted from a real surface $\mathrm{d}A$ at temperature T, per unit time in wavelength interval $\mathrm{d}\lambda$ and within the solid angle $\mathrm{d}\omega$ must by definition be

$$\mathrm{d}^3 Q'_{\lambda e}(\lambda, \beta, \theta, T) = e'_\lambda(\lambda, \beta, \theta, T)\,\mathrm{d}A\,\mathrm{d}\lambda\,\mathrm{d}\omega \tag{3.24}$$

where e'_λ is termed the directional spectral emissive power for a real surface. It is conceptually the same as that for the surface of a blackbody except that it now refers to a real body's radiating surface.

Similarly, for a blackbody the energy per unit time leaving a black surface element $\mathrm{d}A$ per unit time within $\mathrm{d}\lambda$ and $\mathrm{d}\omega$ is

$$\begin{aligned} \mathrm{d}^3 Q'_{\lambda b}(\lambda, \beta, T) &= e'_{\lambda b}(\lambda, \beta, T)\,\mathrm{d}A\,\mathrm{d}\lambda\,\mathrm{d}\omega \\ &\left(= \frac{e_{\lambda b}(\lambda, T)\cos(\beta)}{\pi}\,\mathrm{d}A\,\mathrm{d}\lambda\,\mathrm{d}\omega \quad \text{using (3.21)} \right) \end{aligned} \tag{3.25}$$

By definition then, the directional spectral emissivity, ϵ'_λ, is

$$\epsilon'_\lambda(\lambda, \beta, \theta, T) \equiv \frac{\mathrm{d}^3 Q'_{\lambda e}}{\mathrm{d}^3 Q'_{\lambda b}} = \frac{e'_\lambda(\lambda, \beta, \theta, T)}{e'_{\lambda b}(\lambda, \beta, T)} \tag{3.26}$$

This is the most fundamental emissivity, because it includes a dependence on the wavelength and direction of emitting radiation, and the temperature of the surface.

However, if the material surfaces do not manifest strong dependence on either emitted wavelength or direction, then averaged emissivity quantities are desirable, in which one or more of these dependences are removed. The advantage is that the analysis is greatly simplified. Also, it turns out that values for averaged emissivities are more readily obtainable experimentally. Such averaged quantities will now be derived.

The hemispherical total emissive power for a real surface is obtained by integrating e'_λ over all solid angles and over all wavelengths, and using (3.26):

$$\begin{aligned} e(T) &= \int_{\mathrm{E}} \int_{\lambda=0}^{\infty} e'_\lambda\,\mathrm{d}\lambda\,\mathrm{d}\omega \\ &= \int_{\mathrm{E}} \int_{\lambda=0}^{\infty} \epsilon'_\lambda e'_{\lambda b}\,\mathrm{d}\lambda\,\mathrm{d}\omega \end{aligned} \tag{3.27}$$

where '$\int_{\mathrm{E}} \square\,\mathrm{d}\omega$' denotes integration over the hemisphere above $\mathrm{d}A$.

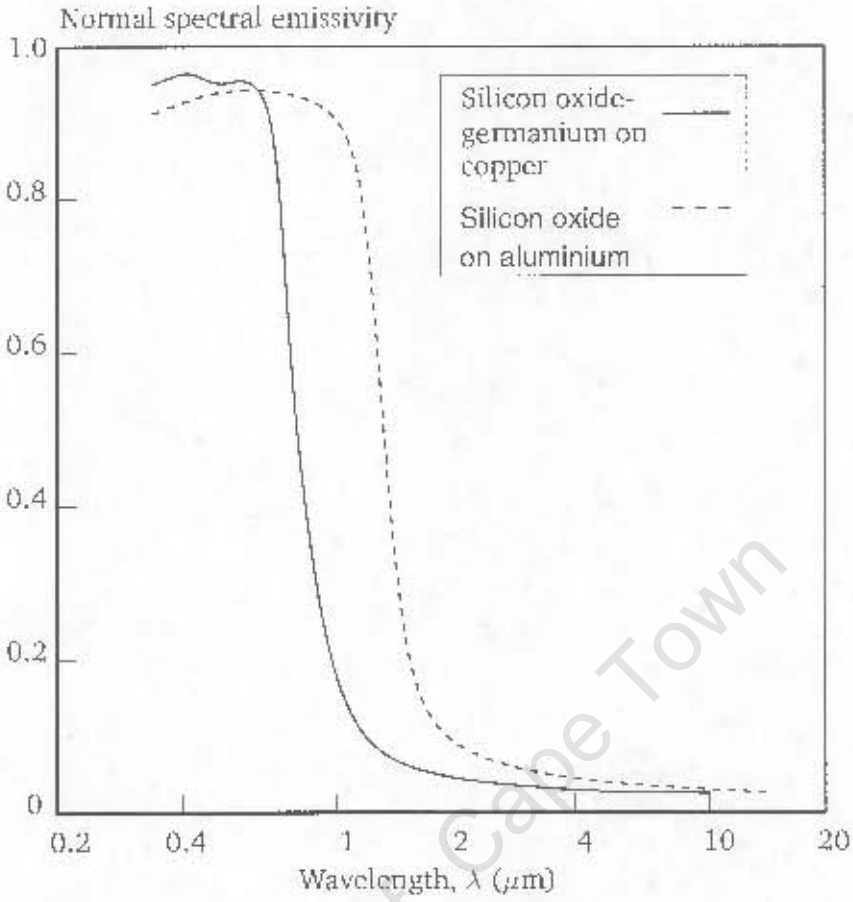

Figure 3.7: Characteristics of two spectrally selective surfaces [42, p149]

Similiar to the definition (3.26) and using (3.23), the hemispherical total emissivity is then defined as the ratio

$$\epsilon(T) \equiv \frac{e(T)}{e_b(T)} \qquad \frac{\int_{\gamma}\int_{\lambda=0}^{\infty} \epsilon'_{\lambda}\epsilon'_{\lambda b}\,\mathrm{d}\lambda\,\mathrm{d}\omega}{\sigma T^4} \tag{3.28}$$

The emissivity, $\epsilon(T)$, is usually measured experimentally.

All these quantities are totalled in the sense that contributions to the emitted energy are integrated over all wavelengths and averaged over all directions in the hemisphere above the emitting surface element. If the diffuse–grey assumptions (see §3.3.4) can be applied, and if the temperature does not vary dramatically from surface element to surface element within the cavity, then dependence of the radiant interactions on wavelength and direction may be removed in the subsequent analysis.

However, if the radiating cavity contains either specular surfaces, e.g., mirrors, for which the radiative properties depend strongly on direction, or spectral surfaces, e.g., solar selective surfaces (Figure 3.7 [72, 73]), for which properties depend on wavelength, then specular or spectral dependence, must be retained in the analysis.

The absorptivity is defined as the fraction of radiant energy incident on the surface of a body that is absorbed by the body. Experimentally it is often easier to measure the emissivity than the absorptivity. Hence, it is desirable to relate the two quantities, so that measured values of emissivity will allow the absorptivity values to be calculated. Such relations will be developed here.

If $\mathrm{d}^3Q'_{\lambda i}$ is the energy incident on a surface element $\mathrm{d}A$ from direction (β, θ) in wavelength interval $\mathrm{d}\lambda$, and if $\mathrm{d}^3Q'_{\lambda a}$ is that part of the incident energy that is absorbed by the surface, then the directional spectral absorptivity is defined as the ratio

$$\alpha'_\lambda(\lambda, \beta, \theta, T) = \frac{\mathrm{d}^3Q'_{\lambda a}(\lambda, \beta, \theta)}{\mathrm{d}^3Q'_{\lambda i}(\lambda, \beta, \theta, T)} \tag{3.29}$$

Suppose that the surface element $\mathrm{d}A$ at temperature T is placed in an isothermal black enclosure also at temperature T. Since the intensity within the black enclosure is isotropic the following relations must be satisfied:

$$\mathrm{d}^3Q'_{\lambda i} = e'_{\lambda i}\,\mathrm{d}A\,\mathrm{d}\lambda\,\mathrm{d}\omega = e'_{\lambda b}\,\mathrm{d}A\,\mathrm{d}\lambda\,\mathrm{d}\omega = \mathrm{d}^3Q'_{\lambda b} \tag{3.30}$$

where $e'_{\lambda i}$ is the directional spectral incident power.

Furthermore, in order to maintain isotropy within the enclosure, the energy emitted by the surface element must equal the energy that it absorbs. That is, $\mathrm{d}^3Q'_{\lambda a} = \mathrm{d}^3Q'_{\lambda e}$. Comparing (3.26) with (3.29) it is evident then that

$$\alpha'_\lambda(\lambda, \beta, \theta, T) = \epsilon'_\lambda(\lambda, \beta, \theta, T) \tag{3.31}$$

This law was originally proved for thermodynamic equilibrium in an isothermal enclosure, and hence is strictly only true when there is no net heat transfer to or from the surface. The validity of this approximation is however based on experimental evidence that in most applications ϵ'_λ and α'_λ are not significantly influenced by the surrounding radiation field.

The hemispherical total absorptivity, $\alpha(T)$, represents the fraction of energy incident on a body that is absorbed by the body from all directions of an enclosing hemisphere and for all wavelengths, as shown in Figure 3.8. The incident energy intercepted by the surface element is determined by integrating (3.30) over all λ and all directions (β, θ) of the hemisphere:

$$\mathrm{d}Q_i = \mathrm{d}A \int_\beta \int_{\lambda=0}^{\infty} e'_{\lambda i}\,\mathrm{d}\lambda\,\mathrm{d}\omega \tag{3.32}$$

Similarly, using (3.29) and (3.31), the total absorbed energy is equal to

$$\mathrm{d}Q_a(T) = \mathrm{d}A \int_\beta \int_{\lambda=0}^{\infty} \epsilon'_\lambda e'_{\lambda i}\,\mathrm{d}\lambda\,\mathrm{d}\omega \tag{3.33}$$

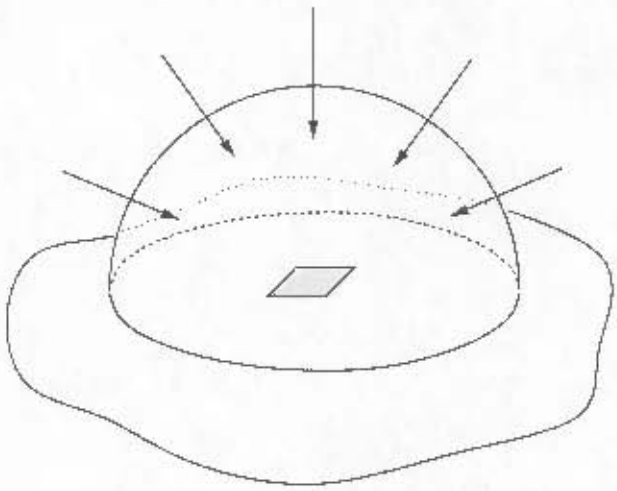

Figure 3.8: Total incident energy into an enclosing hemisphere

The hemispherical total absorptivity is then equal to

$$\alpha(T) = \frac{\mathrm{d}Q_a(T)}{\mathrm{d}Q_i} \quad \frac{\int_{\cdot}\int_{\lambda=0}^{\infty} \epsilon'_\lambda \epsilon'_{\lambda i}\,\mathrm{d}\lambda\,\mathrm{d}\omega}{\int_{\cdot}\int_{\lambda=0}^{\infty} \epsilon'_{\lambda i}\,\mathrm{d}\lambda\,\mathrm{d}\omega} \tag{3.34}$$

Continuing in a similar fashion, the fraction of energy incident from all solid angles and all wavelengths that is reflected into the entire hemisphere at the surface element $\mathrm{d}A$ is termed the hemispherical total reflectivity and may be written as

$$\rho(T) = \frac{\mathrm{d}Q_r(T)}{\mathrm{d}Q_i} \tag{3.35}$$

where $\mathrm{d}Q_r(T)$ is the energy per unit time reflected by the surface element.

For an opaque body conservation of radiant energy at a surface element implies

$$\mathrm{d}^3Q_i = \mathrm{d}^3Q_a(T) + \mathrm{d}^3Q_r(T) \tag{3.36}$$

so that using (3.34) and (3.35)

$$\alpha(T) + \rho(T) = 1 \tag{3.37}$$

3.3.4 The Diffuse–Grey Cavity Approximation

Within a cavity, the geometry of the cavity is an additional factor influencing the nature of radiant interactions. Indeed, for cavities having complex geometries the influence is dominant and it is then usually necessary to apply certain idealizations in order that the interactions may be handled with reasonable effort.

In this analysis, the radiation character of non–black surfaces will be idealised in such a way that (3.31) will hold for the averaged quantities (3.28) and (3.34). The applicability of these idealizations in modelling the radiation behaviour within a DS furnace will also be discussed.

Idealizing the Emitted Radiation

The first idealization is concerned with radiation that is emitted from a surface. If, in Equation (3.24), the directional spectral emission, e'_λ, from a surface has the same directional dependence as that of a blackbody surface, then by adopting the form of (3.19), e'_λ must be able to be written as

$$e'_\lambda(\lambda, \beta, \theta, T) = i'_\lambda(\lambda, T)\cos(\beta) \tag{3.38}$$

wherein the spectral intensity, i'_λ, no longer depends on direction. From (3.26) and again (3.19), the directional spectral emissivity, ε'_λ, then becomes

$$\varepsilon'_\lambda(\lambda, \beta, \theta, T) = \frac{i'_\lambda(\lambda, T)}{i'_{\lambda b}(\lambda, T)} \tag{3.39}$$

which is clearly independent of direction (β, θ).

The approximation (3.38) with (3.39) shall be termed the diffuse approximation, because the intensity, i'_λ, of the surface is emitted diffusely, i.e., independent of direction, just as is the case for the blackbody intensity, $i'_{\lambda b}$.

On the other hand, if e'_λ has the same spectral dependence as that of a blackbody surface, then it must be possible to write e'_λ as

$$e'_\lambda(\lambda, \beta, \theta, T) = i'_{\lambda b}(\lambda, T)\, A(\beta, \theta, T) \tag{3.40}$$

for some function $A(\beta, \theta, T)$ which does not depend on wavelength. Substituting (3.40) and (3.19) into (3.26), it is clear that ε'_λ then becomes

$$\varepsilon'_\lambda(\lambda, \beta, \theta, T) = \frac{A(\beta, \theta, T)}{\cos(\beta)} \tag{3.41}$$

which is independent of wavelength. Following Siegel and Howell [42], the approximation (3.40) together with (3.41) shall be termed the grey approximation.

If both the diffuse and the grey approximations are applicable simultaneously, then both (3.39) and (3.41) must be applicable simultaneously. I.e.,

$$\frac{i'_\lambda(\lambda, T)}{i'_{\lambda b}(\lambda, T)} = \frac{A(\beta, \theta, T)}{\cos(\beta)} \tag{3.42}$$

The left hand side of (3.42) depends on λ and T, whereas the right hand side depends on β, θ and T. This can only be possible for any set $\{\lambda, \beta, \theta, T\}$ if both sides only depend on T.

Therefore, under both the diffuse and the grey approximations, for any wavelength or direction, the emitted radiation remains a fixed fraction of the radiation that would be emitted by a blackbody surface at the same temperature, T; and the directional spectral emissivity is a function of surface temperature only. Using (3.21) and (3.22), ϵ'_λ may be removed from both integrals in (3.28), to give

$$\epsilon(T) = \epsilon'_\lambda(T)\frac{\int_\beta \cos(\beta)\,\mathrm{d}\omega \int_{\lambda=0}^{\infty} e_{\lambda b}(\lambda, T)\,\mathrm{d}\lambda}{\pi\sigma T^4} = \epsilon'_\lambda(T) \tag{3.43}$$

Similarly, when the diffuse and grey approximations are applied to the expression for absorptivity in (3.34), ϵ'_λ may be moved out of the integral, giving the important result

$$\alpha(T) = \epsilon(T) = 1 - \rho(T) = \epsilon'_\lambda(T) \tag{3.44}$$

Idealizing the Incident Radiation

An alternative idealization is concerned not with emitted radiation, but rather with the radiation that is incident on a surface. If the incident radiation satisfies the condition that, for a blackbody at temperature T,

$$e'_{\lambda,i}(\lambda, \beta, \theta, T) = B\, e'_{\lambda b}(\lambda, \beta, \theta, T) \tag{3.45}$$

for some constant B, then using (3.21) and (3.22), it is easy to show that the expression for the absorptivity (3.34) is identical to the expression in (3.28). That is, the equality (3.44) is reproduced whenever the incident emissive power, $e'_{\lambda,i}$, has the same spectral and directional form as that which is emitted by a blackbody at a temperature equal to the surface temperature.

The Diffuse–Grey Approximation

The two idealizations described here will collectively be termed the diffuse–grey approximation. Under the diffuse–grey approximation, the directional and spectral quantities no longer depend on direction and wavelength. It is sufficient to work with the averaged quantities, such as (3.43) and (3.44) only.

The DS casting furnace (Figure 2.4) constitutes a radiating cavity in which the diffuse–grey approximation may be applied. The reasons for this are:

- Regions within the cavity where the level of radiation is high are bounded by the graphite resistance heaters and the ceramic mould. The radiation emitted by the rough surfaces of these two objects has a spectral and directional character that is similar to that of a blackbody.
- Because the geometry of the cavity is usually complex, localised strong spectral and directional dependence anywhere in the cavity will be averaged out as it contributes to the incident radiation at any given surface element.

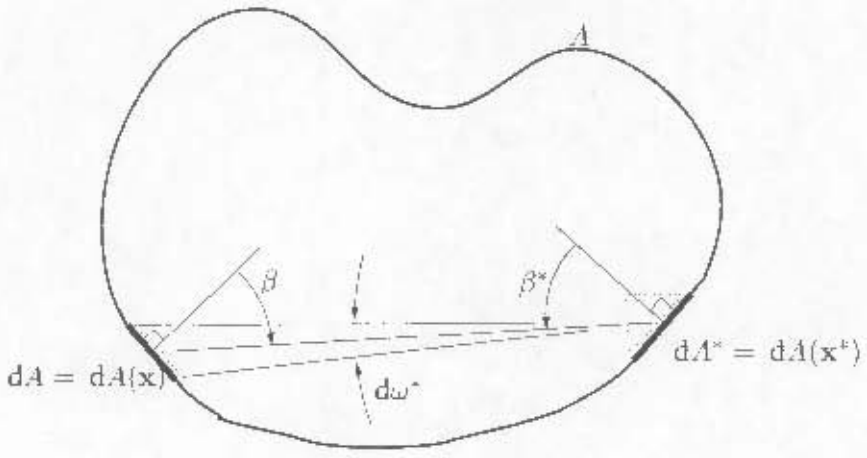

Figure 3.9: Schematic cross-section of a simple occluding radiating cavity

3.3.5 The Boundary Condition

To account for the radiant interactions in the DS casting furnace, values for the heat flux, $q_R(T, \mathbf{x}, t)$, for all radiating surfaces, S_R, must be computed (Equation (3.17)). This flux is just the net radiant heat loss rate per unit area.

At each surface element, $\mathrm{d}A$, within the furnace a fraction of the energy incident on $\mathrm{d}A$ will be reflected. Each reflected beam will in turn be partially absorbed and partially reflected by the other surface elements. Analysing the radiant exchange by tracing the path of each beam element would be a complicated procedure.

A simpler approach is to begin by defining the directional spectral radiosity, $q'_{\lambda o}(\lambda, \beta, \theta, T, \mathbf{x})$, as the sum of the emitted and reflected energy per unit time, per unit wavelength interval and per unit area leaving the surface element $\mathrm{d}A$ (Figure 3.9) in the direction (β, θ)

The energy per unit time leaving another surface element, $\mathrm{d}A^*$, directed at the surface element $\mathrm{d}A$ must then be $q'_{\lambda o}\mathrm{d}\lambda\mathrm{d}\omega^*\mathrm{d}A^*$. Since it is assumed that the cavity is under vacuum, this energy is not attenuated as it travels to $\mathrm{d}A$. Summing contributions from all $\mathrm{d}A^*$, the energy incident on $\mathrm{d}A$ per unit time must therefore be

$$\mathrm{d}Q_i \quad q_i(T, \mathbf{x})\,\mathrm{d}A \quad \int_{\lambda=0}^{\infty}\int_{A} q'_{\lambda o}(\lambda, \beta^*, \theta^*, T^*, \mathbf{x}^*)\,\mathrm{d}\omega^*\,\mathrm{d}A^*\,\mathrm{d}\lambda \tag{3.46}$$

By applying the diffuse–grey approximation this expression will be simplified. The 'diffuse' part of the approximation will be applied first, followed by the 'grey' part.

Under the 'diffuse' approximation the energy leaving $\mathrm{d}A^*$ has the same directional character as that of a blackbody surface at temperature T^*. In §3.3.2 it was shown that the emitted energy in the direction (β, θ) per unit wavelength interval, $\mathrm{d}\lambda$, per unit surface area, $\mathrm{d}A$, and per unit time, is related to the corresponding hemispherical energy by the simple formula (3.21) as

$$e'_{\lambda b}(\lambda, \beta, T) = \frac{\cos(\beta)}{\pi}\, e_{\lambda b}(\lambda, T) \qquad \text{for } 0 \leq \beta < \pi/2$$

Therefore, under the diffuse approximation, $q'_{\lambda o}$ must satisfy

$$q'_{\lambda o}(\lambda, \beta^*, \theta^*, T^*, \mathbf{x}^*) = q'_{\lambda o}(\lambda, \beta^*, T^*, \mathbf{x}^*) = \frac{\cos(\beta^*)}{\pi} q_{\lambda o}(\lambda, T^*, \mathbf{x}^*) \tag{3.47}$$

where, analogous with $e_{\lambda b}$, $q_{\lambda o}$ is the hemispherical spectral radiosity at the surface $\mathrm{d}A^*$.

Under the 'grey' approximation, analogous with (3.40), there must exist some function of temperature and position, $q_o(T, \mathbf{x})$, with which I may write

$$\frac{q_{\lambda o}(\lambda, T, \mathbf{x})}{q_o(T, \mathbf{x})} \quad \frac{i'_{\lambda b}(\lambda, T)}{\sigma T^4/\pi} \tag{3.48}$$

If (3.47) and (3.48), together with (3.18), (3.20) and (3.22), are applied to (3.46), then the directional and spectral dependencies of $q'_{\lambda o}$ are extracted to give

$$q_i(T, \mathbf{x})\ \mathrm{d}A = \int_A q_o(T^*, \mathbf{x}^*) \frac{\cos(\beta^*)\,\mathrm{d}\omega^*\,\mathrm{d}A^*}{\pi} \tag{3.49}$$

From (3.49) and invoking once again the diffuse approximation it is clear that the quantity q_o, to be called simply the radiosity, is the total radiant energy per unit surface area leaving the surface $\mathrm{d}A^*$ and entering the hemisphere above $\mathrm{d}A^*$.

Since from Figure 3.9, $\mathrm{d}\omega^* \quad \cos(\beta)\mathrm{d}A/|\mathbf{x} - \mathbf{x}^*|^2$, the above expression may be rewritten as

$$q_i(T, \mathbf{x})\ \mathrm{d}A \quad \int_A q_o(T^*, \mathbf{x}^*)\ \mathrm{d}F(\mathbf{x}^*, \mathbf{x})\,\mathrm{d}A^* \tag{3.50}$$

where

$$\mathrm{d}F(\mathbf{x}^*, \mathbf{x}) = \frac{\cos(\beta^*)\cos(\beta)\,\mathrm{d}A}{\pi\,|\mathbf{x} - \mathbf{x}^*|^2} \tag{3.51}$$

is the fraction of energy per unit time leaving $\mathrm{d}A^*$ that arrives at $\mathrm{d}A$. It will be termed a view factor (or configuration factor) to emphasise that for diffuse–grey cavities this fraction depends on geometric quantities only, namely the size of $\mathrm{d}A$ and its orientation with respect to $\mathrm{d}A^*$.

From (3.50) it is clear that

$$\mathrm{d}A^*\,\mathrm{d}F(\mathbf{x}^*, \mathbf{x}) = \mathrm{d}A\,\mathrm{d}F(\mathbf{x}, \mathbf{x}^*) \tag{3.52}$$

Using this reciprocity relation in (3.49), the incident flux for a surface element $\mathrm{d}A$ at the point $\mathbf{x}$ is derived as

$$q_i(T, \mathbf{x}) \quad = \int_{\text{views}} q_o(T^*, \mathbf{x}^*)\,\mathrm{d}F(\mathbf{x}, \mathbf{x}^*) \tag{3.53}$$

The radiosity of the surface element is the sum of the emitted energy and reflected incident energy:

$$q_o(T, \mathbf{x}) = e(T, \mathbf{x}) + \rho(T, \mathbf{x})\ q_i(T, \mathbf{x}) \tag{3.54}$$

Combining (3.53) with (3.54) and using (3.28) provides an integral formula for the radiosity at any point, $\mathbf{x}$, within the cavity as

$$q_o(T,\mathbf{x}) - \rho(T,\mathbf{x}) \int_{\text{views}} q_o(T(\mathbf{x}^*),\mathbf{x}^*)\,\mathrm{d}F(\mathbf{x},\mathbf{x}^*) - \sigma\,\epsilon(T,\mathbf{x})\,T^4(\mathbf{x}) = 0 \qquad (3.55)$$

Considering a virtual surface of area $\mathrm{d}A$ directly above the surface element $\mathrm{d}A(\mathbf{x})$ (Figure 3.9), the net heat transfer at the virtual surface is

$$q\,\mathrm{d}A = (q_o - q_i)\,\mathrm{d}A \qquad (3.56)$$

If a solution to q_o can be obtained from (3.55), then using (3.54) and (3.44) gives

$$q(T,\mathbf{x}) = \epsilon(T,\mathbf{x})\left[\sigma T^4 - q_i(T,\mathbf{x})\right] \qquad \forall\,\mathbf{x} \text{ on } S_R \qquad (3.57)$$

This is an important result in that it provides precisely the radiant heat transfer mechanism, q_R, that was sought in the natural boundary condition (3.17). The mechanism clearly depends not only on the local conditions prevailing at the surface element $\mathrm{d}A$, but also on the radiative state of the enclosure as a whole.

The complexity inherent in modelling diffuse-grey radiant interactions is contained in (3.55). The radiosity at any point depends integrally on the radiosities of all other points in the cavity. Analytical solutions are therefore only obtainable for the simplest cavity geometries. Thus, a numerical solution must be sought (see Chapter 4).

3.4 Initial Casting Conditions

In addition to the requirement for the prescription of boundary conditions, (3.6) is only able to predict the temperature evolution in a casting once the initial thermal state of all materials have been specified. Such an initial state will be specified in the form

$$T = T_0(\mathbf{x}) \qquad \forall\,\mathbf{x} \text{ in } V \text{ and } t = 0 \qquad (3.58)$$

which will be applied either separately over each spatial material domain or over the entire domain. In the numerical models developed in this work, the initial state is prescribed such that the thermal state immediately after pouring is simulated.

Equations (3.6), (3.16), (3.17) and (3.58), complete the mathematical description of the heat conduction in a homogeneous isotropic solid. This description is known as the strong form.

3.5 Summary

In this chapter a strong form was developed to describe mathematically the conservation of heat energy within the DS casting furnace. It was assumed that energy conservation within the casting was maintained by heat conduction.

The effect of solidification on the temperature field was accounted for with the release of the latent heat of fusion within the mushy zone. Two equivalent formulations were studied and compared.

In the front-tracking formulation the conservation of heat energy within the molten region of the DS casting is considered separately from that of the solidified region. The formulation lends itself to the derivation of analytic solutions. In the 'specific heat'–based formulations the entire casting is considered as a single region and the solidifying fronts are not tracked explicitly. The formulation lends itself more to the derivation of numerical solutions.

The conservation of energy at radiating material boundaries was studied in detail. The development of a diffuse–grey approximation to radiant interactions within the casting furnace made possible the removal of dependencies on directional and spectral quantities. The use of this approximation in describing the radiation within the DS furnace cavity was motivated.

By analysing the interactions in terms of the sum of the directly emitted and reflected energies leaving each surface element within the furnace, an expression for the net heat flux at the material boundaries was derived. This expression facilitates a coupling between conduction within the casting and radiation without.

Chapter 4

Numerical Model

4.1 Introduction

A numerical solution to the transfer of heat energy during vacuum investment casting processes is developed in this chapter. An isoparametric finite element approximation of heat conduction within the casting is developed along standard lines.

This finite element model is then extended to account for the complex radiant interactions that take place within the furnace cavity. A unique net–radiation model applied to the furnace cavity is coupled to the finite element model at the radiating exterior elemental faces. That is, the finite element calculation is supplied with appropriate flux boundary conditions at these faces and at each time instant for which a solution is sought.

However, a coupling which is implemented naively will compromise the strategy's numerical accuracy and stability. The source of inaccuracy and instability rests in part with the finite element model assuming at least bilinear variations of thermal quantities over an element, but with the radiation model assuming no variation of thermal quantities over a radiating facet. A novel coupling mechanism is developed in this chapter which accounts for this discrepancy and which thereby promotes both accuracy and stability.

The computations associated with the net–radiation model require a database of view factors for every point in the furnace cavity. This set of databases must, in general, be recomputed for every point whenever the geometry of the cavity changes. Modelling these interactions is expensive computationally. The emphasis in this work, therefore, has been on the development of an efficient radiation model.

A 'real–world' directional casting, consisting of six components arranged in a cluster and cast together, is discussed in §6.4 of Chapter 6 below. Simulation such a casting is complicated by: the sheer number of finite elements and radiating facets required to represent the geometry; the complexity of the radiating cavity involving, in this case, a high degree of occlusion; and, the fact that the geometry of the cavity changes over time as the cast cluster is withdrawn

from the furnace. In tackling such numerical models, the development of an efficient radiation model was found to be necessary.

Improved efficiency was obtained along three fronts, namely: reducing the number of required view factors by exploiting the presence of geometrical symmetries; reducing the cost of calculating each view factor; and, reducing the cost associated with each Newton iteration. The increase in efficiencies for the case of modelling the cast cluster is discussed in §6.4.

4.2 Finite Element Approximation of Heat Conduction within the Casting

The strong form developed in Chapter 3 will be recast in a variational (or *weak*) form. An approximate numerical model will be developed by carrying out the following steps:

- A variational statement is found which weakly satisfies the strong form.
- The spatial description is discretised following the standard Galerkin weighted residual approach.
- A well–known trapezoidal rule is used to discretise the temporal behaviour, resulting in a non–linear system of algebraic equations at each time increment. The unknowns are the values of temperature at a finite set of points in the casting.
- The equations are linearised and solved iteratively at each time increment using a modified Newton method.

These steps constitute a finite element approximation. The application of the finite element method to heat transfer problems involving a change of phase has been documented comprehensively in the literature [66],[74]–[179] and so will not be dealt with in much detail here.

4.2.1 Variational Form

A variational statement equivalent to (3.10) together with (3.16), (3.17) and (3.58) may be written as

$$\int_V \phi \frac{\partial H}{\partial t}\,\mathrm{d}V + \int_V \phi \frac{\partial}{\partial \mathbf{x}} \cdot \left(k \frac{\partial T}{\partial \mathbf{x}}\right)\,\mathrm{d}V + \int_{S_R} \phi(\mathbf{q} - \mathbf{q}_R) \cdot \mathrm{d}\mathbf{A} = 0 \tag{4.1}$$

where $\mathrm{d}\mathbf{A} = \mathrm{d}A\hat{\mathbf{n}}$ and $\phi(\mathbf{x}, t)$ is an arbitrary finite–valued variational field having C_1 continuity in the solid volume V. Recall from §3.3 that S_I is that part of the bounding surface of the casting volume V on which the temperature is known and is therefore prescribed. Recall too that S_R is the remainder of the boundary of V, and is the surface on which the heat flux, $\mathbf{q}(\mathbf{x}, t)$,

is prescribed. If (4.1) is satisfied for any arbitrary $\phi(\mathbf{x}, t)$, then the differential equations (3.17) and (3.10) are satisfied implicitly.

Applying Green's Theorem[1] gives

$$\int_V \phi \frac{\partial H}{\partial t}\, \mathrm{d}V + \int_V \frac{\partial \phi}{\partial \mathbf{x}} \cdot k \frac{\partial T}{\partial \mathbf{x}}\, \mathrm{d}V - \int_{\partial V} \phi\, k \frac{\partial T}{\partial \mathbf{x}} \cdot \mathbf{dA} - \int_{S_R} \phi\, (\mathbf{q} - \mathbf{q}_R) \cdot \mathbf{dA} \tag{4.2}$$

By partitioning the bounding surface integral in the third term using $\int_{\partial V} \equiv \int_{S_R} + \int_{S_I}$, and applying Fourier's law (3.1) to the resulting surface integration over S_R yields

$$\int_V \phi \frac{\partial H}{\partial t}\, \mathrm{d}V + \int_V k \frac{\partial \phi}{\partial \mathbf{x}} \cdot \frac{\partial T}{\partial \mathbf{x}}\, \mathrm{d}V + \int_{S_R} \phi\, \mathbf{q}_R \cdot \mathbf{dA} - \int_{S_I} k\, \phi \frac{\partial T}{\partial \mathbf{x}} \cdot \mathbf{dA} = 0 \tag{4.3}$$

The fourth term can be omitted by ensuring that $T(\mathbf{x}, t)$ satisfies the essential boundary condition (3.16) on S_I, and by restricting the choice of ϕ to functions which satisfy $\phi(\mathbf{x}, t) = 0$ for $\mathbf{x}$ on S_I. The resultant weak form is

$$\begin{aligned} \int_V \phi(\mathbf{x}, t) \frac{\partial H(T)}{\partial t}\, \mathrm{d}V + \int_V k(T, \mathbf{x}, t) \frac{\partial \phi(\mathbf{x}, t)}{\partial \mathbf{x}} \cdot \frac{\partial T(\mathbf{x}, t)}{\partial \mathbf{x}}\, \mathrm{d}V \\ + \int_{S_R} \phi(\mathbf{x}, t)\, \mathbf{q}_R(T, \mathbf{x}, t) \cdot \mathbf{dA} = 0 \end{aligned} \tag{4.4}$$

$$T(\mathbf{x}, t) = T_I(\mathbf{x}, t) \qquad \text{for } \mathbf{x} \text{ on } S_I$$

$$\phi(\mathbf{x}, t) = 0 \qquad \text{for } \mathbf{x} \text{ on } S_I$$

Recall from (3.57) that $\mathbf{q}_R(T, \mathbf{x}, t) = q_R(T, \mathbf{x}, t)\hat{\mathbf{n}}$ is the radiant heat flux vector at the point $\mathbf{x}$ on the surface S_R.

When compared to the differential form in (3.10), this weak form permits a lower order of spatial continuity in $T(\mathbf{x}, t)$ at the price of higher order spatial continuity for $\phi(\mathbf{x}, t)$.

4.2.2 Finite Element Approximation

In the method of weighted residuals, using linearly independent functions of position, the temperature field is constrained to have the interpolated form[2]:

$$T(\mathbf{x}, t) = \sum_{N=1}^{N_{\max}} N_N(\mathbf{x})\, T^N(t) \tag{4.5}$$

[1] An alternate form of Green's Theorem states that

$$\int_V f \frac{\partial \mathbf{u}}{\partial \mathbf{x}}\, \mathrm{d}V = -\int_V \frac{\partial f}{\partial \mathbf{x}} \cdot \mathbf{u}\, \mathrm{d}V + \int_{\partial V} f\mathbf{u} \cdot \mathrm{d}\mathbf{S}$$

[2] Throughout the analysis a superscripted Roman numeral or a capital letter index denotes a nodal quantity

The interpolation functions, $N_N(\mathbf{x})$, are chosen to satisfy $N_N(\mathbf{x}^M) = \delta_{NM}$ so that $T^N(t) = T(\mathbf{x}^N, t)$ are the temperatures at the nodal positions $\mathbf{x}^N$.

The standard Galerkin approximation method now restricts the variational fields to have the same form:

$$\phi(\mathbf{x}, t) \approx \sum_{N=1}^{N_{\max}} N_N(\mathbf{x})\, \phi^N(t) \tag{4.6}$$

The functions $\phi^N(t)$ are still arbitrary. Therefore, if the interpolation functions have sufficient continuity, then (4.4) is approximated by a system of $N_{\max}$ weighted integral residual statements:

$$\begin{aligned}\int_V \frac{\partial H(T)}{\partial t} N_M \,\mathrm{d}V + \sum_{N=1}^{N_{\max}} \int_V k(T, \mathbf{x}, t) \frac{\partial N_M}{\partial \mathbf{x}} \cdot \frac{\partial N_N}{\partial \mathbf{x}} \,\mathrm{d}V\, T^N(t) \\ + \int_{S_R} N_M\, \mathbf{q}_R(T, \mathbf{x}, t) \cdot \mathrm{d}A = 0 \quad \text{for } M = 1, \ldots, N_{\max}\end{aligned} \tag{4.7}$$

subject to the constraint

$$T^M(t) = T_I(\mathbf{x}^M, t) \qquad \text{for all } M \text{ s.t. } \mathbf{x}^M \text{ on } S_I \tag{4.8}$$

Equation (4.7) is thus a time–continuous description of a geometric approximation.

4.2.3 Temporal Discretization

Firstly, the nodal temperatures in (4.7) are approximated at any time τ by the (as yet unknown) quantities T_τ^N. Secondly, the following additional approximations are then made:

$$\begin{aligned} T(\mathbf{x}, t)|_{t=\tau} &\approx T_\tau(\mathbf{x}) \equiv \sum_{N=1}^{N_{\max}} N_N(\mathbf{x})\, T_\tau^N \\ H(T)|_{t=\tau} &\approx H(T_\tau) \\ k(T, \mathbf{x}, t)|_{t=\tau} &\approx k(T_\tau, \mathbf{x}, \tau) \\ \mathbf{q}_R(T, \mathbf{x}, t)|_{t=\tau} &\approx \mathbf{q}_R(T_\tau, \mathbf{x}, \tau) \end{aligned} \tag{4.9}$$

The generalised trapezoidal rule is used to discretise the temporal behaviour. If a solution is sought at the time increment $t + \Delta t$, then the rule is of the form

$$f_{t+\Delta t} = f_t + \Delta t\big((1-\gamma)\dot{f}_t + \gamma \dot{f}_{t+\Delta t}\big) \tag{4.10}$$

for some parameter $\gamma \in [0,1]$ and where $f(t)$ is approximated as f_t. The rule is known to be stable whenever $\gamma \geq \frac{1}{2}$ regardless of the size of time increment Δt. Although the Crank–Nicholson method ($\gamma = \frac{1}{2}$) has the highest order truncation error and is therefore the most accurate, it is on the limit of unconditional stability. It is also known to exhibit oscillatory behaviour in early time solutions. The backward difference method ($\gamma = 1$) is therefore chosen:

$$\frac{\partial H}{\partial t} \approx \frac{H(T_{t+\Delta t}) - H(T_t)}{\Delta t} \tag{4.11}$$

Introducing this into (4.7) gives

$$\begin{aligned} &\frac{1}{\Delta t}\int_V [H(T_{t+\Delta t}) - H(T_t)]\, N_M \,\mathrm{d}V \\ &+ \sum_{N=1}^{N_{\max}} \int_V k(T_{t+\Delta t}, \mathbf{x}, t+\Delta t) \frac{\partial N_M}{\partial \mathbf{x}} \cdot \frac{\partial N_N}{\partial \mathbf{x}} \,\mathrm{d}V\, T^N_{t+\Delta t} \\ &+ \int_{S_R} N_M\, \mathbf{q}_R(T_{t+\Delta t}, \mathbf{x}, t+\Delta t) \cdot \mathbf{dA} \\ &\equiv R^M_{t+\Delta t}(T^1_{t+\Delta t}, \ldots, T^{N_{\max}}_{t+\Delta t}) \qquad \text{for } M = 1, \ldots, N_{\max} \end{aligned} \tag{4.12}$$

subject to

$$T^P_{t+\Delta t} = T_I(\mathbf{x}^P, t+\Delta t) \qquad \text{for all } P \text{ s.t. } \mathbf{x}^P \text{ on } S_I \tag{4.13}$$

The problem has now been reduced to a system of non–linear algebraic equations, $R^M_{t+\Delta t} = 0$, for the set of unknown nodal temperatures, $T^N_{t+\Delta t}$, at the next time increment, $t + \Delta t$.

4.2.4 Non–Linear Solution Scheme

The system (4.12) is solved by a modified Newton method (Algorithm 1) in which convergence to a solution at each time increment is obtained iteratively. The method is 'modified' because the rate of change of $R^M_{t+\Delta t}$ with respect to $T^N_{t+\Delta t}$ is not formed exactly, as will be shown below.

The Jacobian matrix element, $J_{MN} = \partial R^M_{t+\Delta t} / \partial T^N_{t+\Delta t}$, is the rate of change of $R^M_{t+\Delta t}$ with respect to $T^N_{t+\Delta t}$. An approximate matrix element is

$$J_{MN} \approx \frac{1}{\Delta t}\int_V \frac{\mathrm{d}H(T_{t+\Delta t})}{\mathrm{d}T} N_M N_N \,\mathrm{d}V + \int_V k(T_{t+\Delta t}, \mathbf{x}, t+\Delta t) \frac{\partial N_M}{\partial \mathbf{x}} \cdot \frac{\partial N_N}{\partial \mathbf{x}} \,\mathrm{d}V \tag{4.14}$$

The derivation of the first term in (4.14) relied on the first approximation in (4.9) and the chain rule

$$\frac{\partial H(T_{t+\Delta t})}{\partial T^N_{t+\Delta t}} = \frac{\mathrm{d}H(T_{t+\Delta t})}{\mathrm{d}T} N_N$$

The derivative $\mathrm{d}H(T_{t+\Delta t})/\mathrm{d}T$ is from (3.13) and (3.14) given by

$$\frac{\mathrm{d}H(T_{t+\Delta t})}{\mathrm{d}T} = \begin{cases} \rho_m \left(C_s(T_{t+\Delta t}) + \dfrac{\Delta L}{T_L - T_S} \right) & T_S \leq T_{t+\Delta t} < T_L \\ \rho_m\, C_p(T_{t+\Delta t}) & \text{otherwise} \end{cases} \tag{4.15}$$

Algorithm 1 Modified Newton iterative method

for each time increment Δt **do**

Make initial guesses:
for $M = 1, \ldots, N_{\max}$ **do**
$T^M_{t+\Delta t} = T^M_t$
for P s.t. $\mathbf{x}^P$ on S_I **do**
$T^P_{t+\Delta t} = T_I(\mathbf{x}^P, t + \Delta t)$

for each Newton iteration until convergence **do**
Solve for the corrections $\Delta T^N_{t+\Delta t}$:

$$\sum_{N=1}^{N_{\max}} J_{MN} \Delta T^N_{t+\Delta t} = -R^M_{t+\Delta t} \text{ for } M = 1, \ldots, N_{\max}$$

Update the nodal temperature estimates:
for $M = 1, \ldots, N_{\max}$ **do**
$T^M_{t+\Delta t} \longleftarrow T^M_{t+\Delta t} + \Delta T^M_{t+\Delta t}$
for P s.t. $\mathbf{x}^P$ on S_I **do**
$T^P_{t+\Delta t} = T_I(\mathbf{x}^P, t + \Delta t)$

The term in (4.12) involving $H(T_t)$ does not contribute to the Jacobian since $H(T_t)$ does not depend on nodal temperatures at time increment $t + \Delta t$.

A conductivity term, $\sum_{P=1}^{N_{\max}} \int_V \frac{\partial k(T_{t+\Delta t}, \mathbf{x}, t+\Delta t)}{\partial T} N_N \frac{\partial N_M}{\partial \mathbf{x}} \cdot \frac{\partial N_P}{\partial \mathbf{x}} \, \mathrm{d}V \, T^P_{t+\Delta t}$, was omitted because the term is not symmetric and the conductivity usually varies slowly with temperature anyway. The general prescribed flux term, $\int_{S_R} N_M N_N \frac{\partial \mathbf{q}_R(T_{t+\Delta t}, \mathbf{x}, t+\Delta t)}{\partial T} \cdot \mathrm{d}A$, is omitted because the derivatives $\partial \mathbf{q}_R / \partial T$ are not calculated *a priori*.

4.2.5 Numerical Integration using Isoparametric Elements

Solving the equations constituted by the Jacobian matrix and the residual vector requires in general that the integrals in (4.12) and (4.14) be evaluated numerically. This is done by sampling the integrands at pre–selected points, adding weight coefficients to these samples, and then summing. A judicious choice of the interpolation functions eases this task and underpins the concept of the finite element.

Isoparametric Element Formulation

Until now in this analysis the only requirement for the interpolation functions, $N_N(\mathbf{x})$, is that they approximate with sufficient accuracy the temperature field according to (4.5). A further requirement is now imposed in that a given N_N must have non–zero values in only a single volume element, V^e, of the volume V. That is

$$N_N(\mathbf{x}) = \begin{cases} N_N^e(\mathbf{x}) & \mathbf{x} \text{ in } V^e \\ \\ 0 & \text{otherwise} \end{cases} \tag{4.16}$$

The volume integrals in (4.12) and (4.14) may then be partitioned as

$$\begin{aligned} I_{MN} &= \sum_{e=1}^{e_{\max}} \int_{V^e} G(N_M^e(\mathbf{x}), N_N^e(\mathbf{x}), \mathbf{x})\, \mathrm{d}V \\ &= \int_{V^f} G(N_M^f(\mathbf{x}), N_N^f(\mathbf{x}), \mathbf{x})\, \mathrm{d}V + \int_{V^g} G(N_M^g(\mathbf{x}), N_N^g(\mathbf{x}), \mathbf{x})\, \mathrm{d}V + \cdots \end{aligned} \tag{4.17}$$

where $e_{\max}$ is the total number of sub–regions. Most importantly, for a given (M, N) pair only those terms in which both N_M and N_N have non–zero values are retained. As indicated in (4.17) this would include the terms involving the sub–regions V^f and V^g, say.

For each element e, eight interpolation functions are chosen to define three–dimensional first–order hexahedral elements as:

$$N_N^e(\mathbf{x}(\xi, \eta, \zeta)) = \frac{1}{8}(1 + a_N\xi)(1 + b_N\eta)(1 + c_N\zeta) \tag{4.18}$$

for $\mathbf{x}$ in V^e; $N = 1, ..., 8$; $a_N, b_N, c_N = -1, 1$; $\xi, \eta, \zeta \in [-1, 1]$.

Furthermore, in order to simplify the numerical integration, the element is rendered isoparametric by transforming the spatial coordinate using the same interpolation as in (4.5):

$$\begin{aligned} \mathbf{x} &= \sum_{N=1}^{N_{\max}} N_N(\boldsymbol{\xi})\mathbf{x}^N \qquad \text{for } \mathbf{x} \text{ in } V \\ &= \sum_{I=1}^{8} N_I^e(\boldsymbol{\xi})\mathbf{x}^I \qquad \text{if } \mathbf{x} \text{ in } V^e \end{aligned} \tag{4.19}$$

Numerical Integration

By applying the following well—known formulae [74] for the mapping $\mathbf{x}: \boldsymbol{\xi} \mapsto \mathbf{x}(\boldsymbol{\xi})$:

$$\begin{aligned} \frac{\partial}{\partial \mathbf{x}} &= \left[\frac{\partial \mathbf{x}}{\partial \boldsymbol{\xi}}\right]^{-1} \cdot \frac{\partial}{\partial \boldsymbol{\xi}} \\ \mathrm{d}V &= \det\left(\frac{\partial \mathbf{x}}{\partial \boldsymbol{\xi}}\right) \mathrm{d}\xi\, \mathrm{d}\eta\, \mathrm{d}\zeta \end{aligned} \tag{4.20}$$

where $\partial \mathbf{x}/\partial \boldsymbol{\xi}$ is the transformation matrix of the mapping, the volume integrals in (4.17) are transformed as

$$\int_{V^e} G(N_M^e(\mathbf{x}), N_N^e(\mathbf{x}), \mathbf{x})\, \mathrm{d}V \longrightarrow \int_{-1}^{1}\int_{-1}^{1}\int_{-1}^{1} \bar{G}^e_{MN}(\xi, \eta, \zeta)\, \mathrm{d}\xi\, \mathrm{d}\eta\, \mathrm{d}\zeta \tag{4.21}$$

A Newton–Cotes scheme is chosen to evaluate the integrals numerically using integration points located at the nodes of the elements.[3]

It is clear from (4.14) that this has the effect of diagonalizing the Jacobian term associated with the enthalpy. The volume integrals are thus approximated as

$$\int_{V^e} G(N_M^e(\mathbf{x}), N_N^e(\mathbf{x}), \mathbf{x})\, \mathrm{d}V \approx \sum_{i,j,k=1}^{2} \bar{G}^e_{MN}((-1)^i, (-1)^j, (-1)^k) \tag{4.22}$$

The surface integral in (4.12) may similarly be partitioned as

$$I'_M = \sum_{e'=1}^{e'_{\max}} \int_{S_R^{e'}} G'(N_M^{e'}(\mathbf{x}), \mathbf{x})\, \mathrm{d}A \tag{4.23}$$

where now $e'_{\max}$ is the total number of elemental surfaces, $S_R^{e'}$, comprising S_R. The interpolation functions are chosen as

$$N_N^{e'}(\mathbf{x}(\xi, \eta)) = \frac{1}{4}(1 + a_N\xi)(1 + b_N\eta)$$

so that, by applying a similar procedure as for (4.21), the surface integral is approximated as

$$\int_{S_R} G'(N_M^{e'}(\mathbf{x}), \mathbf{x})\, \mathrm{d}A \approx \sum_{i,j=1}^{2} \bar{G}_M^{e'}((-1)^i, (-1)^j) \tag{4.24}$$

Of course, the summations in (4.24) can only be carried out once numerical values for the radiant heat flux, $q_R(T_{t+\Delta t}, \mathbf{x}, t+\Delta t)$, at the surface integration points are known (see (4.12)). In the next section a numerical model of the radiant interactions is developed which will supply sufficiently accurate approximations to these values.

4.3 Net–Radiation Approximation at the Surface of the Casting

Numerical solution methods of cavity radiation problems are widely reported in the literature. Direct numerical methods include the Monte Carlo methods and the net–radiation methods (also known as zone methods).

Monte Carlo methods [81] use a statistical approach to construct a radiant interaction profile by tracing a large number of individual rays within the cavity. The methods are well adapted

[3] An excellent discussion on Newton–Cotes schemes can be found in [80].

for solving problems having complexities which are geometric and specular in nature. They are, however, computationally very intensive. Maltby and Burns [82] studied the numerical properties of a three–dimensional Monte Carlo simulation. Haidekker *et al* [83] studied a hybrid zone/Monte Carlo method, known as the Discrete Transfer Method.

In the net–radiation methods, physical heat balance principles are applied at elemental surfaces within the cavity [42, 15, 8]. Approximate numerical solutions are obtained by dividing the cavity into a number of isothermal zones, and possible radiative exchanges between every pair of zones are accounted for. The methods are generally more efficient than Monte Carlo methods, but complex geometries can be difficult to model. Since the zones are assumed to be isothermal, results may be inaccurate in regions of high temperature gradients. Also, these isothermal approximations generally make coupling to other non–isothermal heat transfer modes, such as conduction, difficult and inaccurate, unless special care is taken.

Commercial numerical heat transfer codes which account for non–blackbody radiation have generally adopted the net–radiation approach. For example, the general purpose finite element code, ABAQUS, is able to address many heat transfer problems in which radiation and conduction are coupled at solid material boundaries [75]. While its capability can be applied to many industrial radiating systems, I have found it insufficient for modelling complex clustered investment casting processes. The primary reason is that, although cyclic symmetries can be accounted for, they are done so in a computationally intensive manner. In what follows I introduce an alternative handling of geometric symmetries which dramatically boosts computational performance without incurring significant loss in accuracy.

4.3.1 Discretizing the Diffuse–Grey Furnace Cavity

We begin by assuming that the radiating cavity is diffuse–grey (§3.3.4). The cavity is discretised using an assemblage of bilinear isothermal facets. This discretisation results in a system of equations which vary with time and are linear with respect to the unknown radiosities (but not with respect to temperature). The system of equations is solved for each chosen instant using a relaxation method which best exploits the properties of the system matrix.

The system matrix is constructed from a database of view factors. A primary focus of this thesis is to minimise the computational cost of constructing this database. This was achieved in three different ways — the most important of which involved a novel treatment of symmetry within the cavity. These methods are discussed in detail in this section (§4.3).

In a derivation of an approximate numerical prescription for the net heat flux, $q(T, \mathbf{x})$, the furnace cavity is divided into $F_{\max}$ bilinear facets with the n'th facet, S^n, having area A^n, as shown in Figure 4.1. An average temperature for facet S^n is defined by

$$T^n \equiv \left[\frac{1}{A^n} \int_{A^n} [T^n(\mathbf{x})]^4 \, \mathrm{d}A \right]^{\frac{1}{4}} \tag{4.25}$$

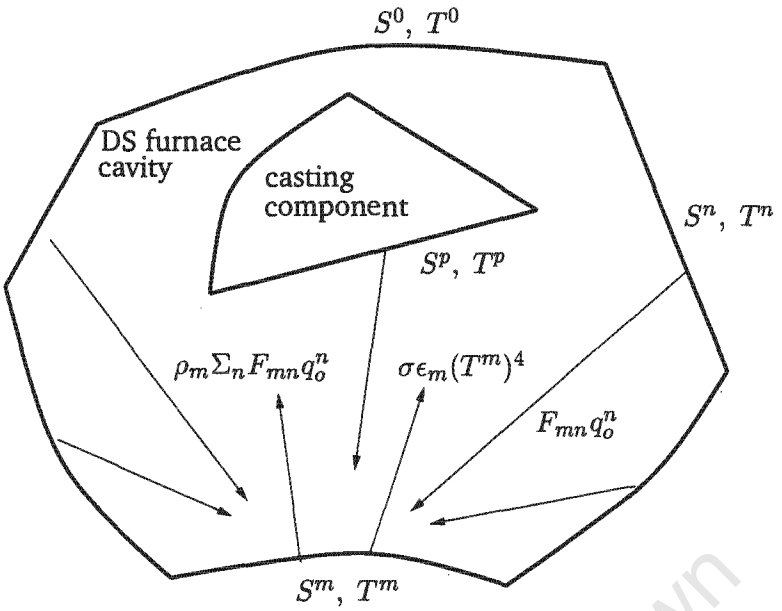

Figure 4.1: Cross–section of a discretised diffuse–grey furnace cavity composed of $F_{\max}$ facets showing energy quantities for a typical facet

Note that T^n is distinctly different from $T^N(t)$ which is an N'th nodal quantity (see Equation (4.5)).

With the definition of the radiosity, $q_o(T, \mathbf{x})$ on page 33, an average radiosity for facet S^n is defined by

$$q_o^n \equiv \frac{1}{A^n} \int_{A^n} q_o(T, \mathbf{x}) \, \mathrm{d}A \tag{4.26}$$

noting the temperature dependence of q_o^n as now being

$$q_o^n = q_o^n(T^1, \ldots, T^{F_{\max}})$$

Lastly, the hemispherical total emissivity (page 27) for all points on the S^n'th facet is approximated as

$$\epsilon(T(\mathbf{x}), \mathbf{x}) \approx \epsilon_n(T^n) \quad \forall \, \mathbf{x} \text{ on } S^n \tag{4.27}$$

The relevant set of thermal quantities for each facet is thus approximated as

$$\begin{aligned} &\{T, \, q(T, \mathbf{x}), \, q_o(T, \mathbf{x}), \, \rho(T, \mathbf{x}), \, \epsilon(T, \mathbf{x})\} \\ &\qquad \approx \{T^n, \, q^n(T^1, \ldots, T^{F_{\max}}), \, q_o^n(T^1, \ldots, T^{F_{\max}}), \, \rho_n(T^n), \, \epsilon_n(T^n)\} \quad \forall \, \mathbf{x} \text{ on } S^n \end{aligned} \tag{4.28}$$

In regions within the cavity where radiant quantities vary markedly with geometry, the density of facets must be increased until these approximations can be applied reliably. Also, the density of the facets may need to be increased in order to represent a geometry with sufficient accuracy. As will be evident in this section, the restriction on the facets to be bilinear greatly simplifies the geometric calculations.

If (3.55) is then integrated with $\frac{1}{A^m}\int_{A^m}$, the above approximations may then be invoked, resulting in

$$q_o^m(T^1,\ldots,T^{F_{\max}}) - \frac{1}{A^m}\rho_m(T^m)\int_{A^*} q_o(T,\mathbf{x}^*)\int_{A^m}\frac{\cos(\beta(\mathbf{x},\mathbf{x}^*))\cos(\beta(\mathbf{x}^*,\mathbf{x}))}{\pi\left|\mathbf{x}-\mathbf{x}^*\right|^2}\,\mathrm{d}A\,\mathrm{d}A^* - \sigma\epsilon_m(T^m)[T^m]^4 = 0 \quad (4.29)$$

The starred $(*)$ quantities apply over the entire radiating cavity, A^* $(= A)$, whereas the unstarred quantities apply over facet S^m only.

A further assumption is now made that q_o^n, as defined in (4.26), reasonably approximates the radiosity of the entire facet, S^n. Under this assumption (4.29) is thus approximated by

$$q_o^m - \frac{1}{A^m}\rho_m\sum_{n=1}^{F_{\max}} q_o^n\int_{A^n}\int_{A^m}\frac{\cos(\beta(\mathbf{x},\mathbf{x}^*))\cos(\beta(\mathbf{x}^*,\mathbf{x}))}{\pi\left|\mathbf{x}-\mathbf{x}^*\right|^2}\,\mathrm{d}A^m\,\mathrm{d}A^n - \sigma\epsilon_m[T^m]^4 = 0 \quad (4.30)$$

where now, for each m and n, $\mathbf{x}$ is on S^m and $\mathbf{x}^*$ is on S^n. It is further assumed that each radiating facet is sufficiently small that the integrand in (4.30) does not vary markedly over S^m. The integrand may then be removed from the integral over S^m:

$$\int_{A^n}\int_{A^m}\frac{\cos(\beta(\mathbf{x},\mathbf{x}^*))\cos(\beta(\mathbf{x}^*,\mathbf{x}))}{\pi\left|\mathbf{x}-\mathbf{x}^*\right|^2}\,\mathrm{d}A^m\,\mathrm{d}A^n \approx A^m\int_{A^n}\frac{\cos(\beta(\mathbf{c}^m,\mathbf{x}^*))\cos(\beta(\mathbf{x}^*,\mathbf{c}^m))}{\pi\left|\mathbf{c}^m-\mathbf{x}^*\right|^2}\,\mathrm{d}A^n$$

where $\mathbf{c}^m$—the centroid of S^m—and the two β angles are defined in Figure 4.2.

Finally, returning again to (3.55), it is thus evident that (3.55) is approximated by the discrete system

$$\sum_{n=1}^{F_{\max}} G_{mn}q_o^n = \sigma\epsilon_m[T^m]^4 \qquad m = 1,\ldots,F_{\max} \quad (4.31)$$

for the set of unknowns $\{q_o^n | n = 1\ldots F_{\max}\}$, and where

$$G_{mn} \equiv \delta_{mn} - \rho_m F_{mn}$$

$$F_{mn} \equiv \begin{cases} \displaystyle\int_{A^n}\frac{\cos(\beta(\mathbf{c}^m,\mathbf{x}^*))\cos(\beta(\mathbf{x}^*,\mathbf{c}^m))}{\pi\left|\mathbf{c}^m-\mathbf{x}^*\right|^2}\,\mathrm{d}A^n & m \neq n \\ 0 & \text{otherwise} \end{cases} \quad (4.32)$$

Allowance for Radiation to an Ambient Blackbody Environment

If the assemblage of surfaces, $\{S^n \mid n = 1,\ldots,F_{\max}\}$, does not form a closed cavity, then it may be intended that the 'holes' in the cavity be sources of blackbody radiation. For example, in many equiaxed casting procedures the molten metal is allowed to cool in an exposed ambient

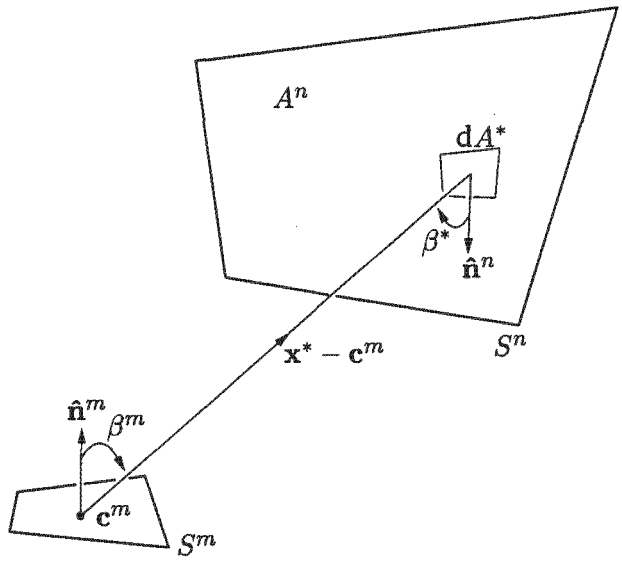

Figure 4.2: Nomenclature for the surface integration of the view factor F_{mn}

blackbody environment. Since the blackbody holes do not reflect any incident radiation, their radiosities must equal their hemispherical emissive powers (Equation (3.27) of §3.3.3). Equation (4.31) must then be modified to accommodate this specific radiant interaction so that in this case

$$\sum_{n=1}^{F_{\max}} G_{mn} q_o^n = \sigma \epsilon_m [T^m]^4 + \sigma \rho_m F_{ma} [T_a]^4 \tag{4.33}$$

where $F_{ma} = 1 - \sum_{n=1}^{F_{\max}} F_{mn}$ and T_a is the ambient blackbody temperature. The last term in (4.33) is the heat flux reflected from the m'th facet that originated from the blackbody holes.

In the software implementation described in Chapter 5 a boolean switch is provided to allow for this type of interaction and with which a constant blackbody temperature may be assigned.

4.3.2 Iterative Numerical Solution Scheme

The integral equation (3.55) has now been reduced to a system of discrete linear equations for the unknowns, q_o^n. A numerical scheme is sought which best exploits the properties of the system matrix $[\delta_{mn} - \rho_m F_{mn}]$ in (4.31), and which is able to utilise any additional information, such as good initial estimates.

A primary feature of this matrix is its strong diagonal dominance even without the use of any special row ordering. This dominance becomes more pronounced when either:

- the number, $F_{\max}$, of facets comprising the radiating cavity increases, or

- the geometric complexity of the cavity increases, since many F_{mn} views vanish due to the likely increased presence of occlusions (see §4.3.3).

In such circumstances relaxation methods are known to converge rapidly. In relaxation methods the system matrix is not inverted explicitly. Instead, corrections to an initial estimate are applied iteratively.

At the start of the finite element simulation a reasonable initial estimate, q_o^{*n} say, to the radiosity vector in (4.31) is to neglect interactions between the radiating surfaces of the casting, so that

$$q_o^{*n} = \begin{cases} \sigma\epsilon_n[T^n]^4 & \text{no blackbody radiation} \\ \\ \sigma\epsilon_n[T^n]^4 + \sigma\rho_n F_{na}[T_a]^4 & \text{blackbody radiation present} \end{cases} \tag{4.34}$$

Whereas, at the start of any subsequent time increment, initial estimates are the computed radiosities of the last finite element iteration of the previous time increment (see §4.2.4).

The Gauss–Seidel relaxation method [80] was used in this work to approximate a solution to the radiosity vector during any finite element iteration of any time increment (Algorithm 2). The validity of the Gauss–Seidel scheme may be verified by replacing q_o^{*n} with q_o^n to arrive at (4.33). In the simulations discussed in §6.2 and §6.4 it was found in this case that the average number of iterations to reach convergence was equal to 2.

Algorithm 2 Gauss–Seidel iterative scheme

$relError = relMaxResidual + 1$

while $relError > relMaxResidual$ **do**
  $relError = 0$

  for $m = 1, \ldots, F_{\max}$ **do**
    $q_o^m = \sigma\epsilon_m[T^m]^4 + \rho_m \sum_{\substack{n=1 \\ n\neq m}}^{F_{\max}} F_{mn} q_o^{*n} + \gamma\sigma\rho_m F_{ma}[T_a]^4$
    if $|q_o^m| > 0$ **then**
      if $|(q_o^m - q_o^{*m})/q_o^m| > relError$ **then**
        $relError = |(q_o^m - q_o^{*m})/q_o^m|$

    $q_o^{*m} = q_o^m$

An ambient blackbody interaction will be neglected for any facet, S^m, if either $F_{ma} = 0$ (i.e., whenever S^m has its full complement of view factors), or the switch, $\gamma \in \{0, 1\}$, has been set to 0.

As Figure 4.1 indicates, certain facets within the cavity coincide geometrically with radiating elemental faces of the finite element mesh, while the remaining facets define the furnace geometry. Numerical values for the average net heat flux are only needed for the set of coincident

facets, $\{S^p\}$, say. The computation of the net heat fluxes is therefore be restricted to this set only. From (3.54) and (3.57), on these facets the flux is computed as

$$q^p = \begin{cases} \frac{\epsilon_p}{\rho_p}\left(\sigma[T^p]^4 - q_o^p\right) & \rho_p \neq 0 \\ \\ \epsilon_p\left(\sigma[T^p]^4 - q_i^p\right) & \text{otherwise} \end{cases} \tag{4.35}$$

where from (3.53) the average incident flux over the p'th facet is approximated as

$$q_i^p = \sum_{\substack{n=1 \\ n\neq m}}^{F_{\max}} F_{pn} q_o^n \tag{4.36}$$

However, since the finite element calculations require net flux values at the integration points rather than an average value over an elemental face, a novel technique was developed for providing accurate estimates to the net heat flux at the integration points. This will be discussed in §4.4.

4.3.3 The View Factor Database

The spatial discretization of the furnace cavity has allowed the sole dependence on geometry of the infinitesimal view factor in (3.53) to be carried over to its finite counterpart, where F_{mn} depends upon the magnitude of A^n and its orientation with respect to A^m.

The computation of the view factor database,
$\{F_{mn} \mid m, n = 1, \ldots, F_{\max}; n \neq m\}$ is by far the most computationally expensive task in simulating radiant interactions. If the properties of the view factors are not exploited, it is easy to see that storage space must be allocated for $F_{\max}(F_{\max} - 1)$ entries in the view factor matrix $\{F_{mn}\}$, and the matrix must be recomputed whenever the geometry of the cavity changes. Furthermore, the computation of the integration in (4.32) for each view factor is costly. It will be shown in this section that the number of computations required to populate this matrix is, in general, proportional to $\frac{1}{2}F_{\max}(F_{\max} - 1)(F_{\max} - 2)$.

A primary initiative of this thesis is to reduce the cost associated with this matrix. This has been achieved in a number of ways as follows:

- For a given number of facets, $F_{\max}$, the number of computations was reduced by: deriving an analytic expression for the view factor, F_{mn}; invoking view factor reciprocity; and, developing an efficient algorithm to address occlusion.
- The need to recompute the matrix at every time increment was eliminated by developing a special algorithm for simulating casting motion relative to the furnace walls.

- Most importantly, the overall size of the view factor matrix was dramatically reduced through the development of a unique algorithm to exploit the existence of planes of geometric symmetry within the furnace.

These planes of symmetry may apply to the radiating cavity as a whole (i.e., the furnace chamber) or to parts of the cavity separately (such as the exterior surfaces of the ceramic mould surrounding the solidifying metal). For example, the symmetry planes that exist in the furnace chamber are in general different from those that exist in the casting geometry.

Geometrical Attributes of a Facet

In order to compute the view factor matrix, certain geometrical attritubes must be stored for each facet. These attributes are: the normal vector; the centroid position; the magnitude of its area; and the positions of the nodes. Using the nomenclature defined in Figure 4.3, they are calculated for the p'th facet as follows:[4]

$$\begin{aligned}
\hat{\mathbf{n}}^p &= \frac{(\mathbf{x}^3 - \mathbf{x}^1) \times (\mathbf{x}^4 - \mathbf{x}^2)}{|(\mathbf{x}^3 - \mathbf{x}^1) \times (\mathbf{x}^4 - \mathbf{x}^2)|} \\
\mathbf{c}^p &= \frac{1}{4}\left[\mathbf{x}^1 + \cdots + \mathbf{x}^4\right] \\
A^p &= \sum_{n=1}^{4} l^n (l^n - |\mathbf{d}^n|)(l^n - |\mathbf{u}^n|)(l^n - |\mathbf{u}^{n+1}|) \\
&\qquad \text{where } l^n \equiv \frac{1}{2}\left(|\mathbf{d}^n| + |\mathbf{u}^n| + |\mathbf{u}^{n+1}|\right)
\end{aligned} \tag{4.37}$$

where it is understood that $\mathbf{u}^5 \equiv \mathbf{u}^1$.

Occlusion

The geometry of the exterior surfaces of the casting and the interior surfaces of the furnace (Figure 4.1) comprising the radiating cavity, is of such a nature that a typical facet cannot have a direct 'line of sight' with all other facets. One or more 'third–party' facets may obscure the view. By virtue of this occlusion many of the view factors must be zero.

In deriving an algorithm to account for the existence of occlusion between two facets, S^m and S^n, the setup shown in Figure 4.3 was considered. In the figure $m = 1$ and $n = 2$ for sake of convenience only. The view factor, F_{mn}, will be deemed to vanish whenever one of the following conditions is satisfied:

- The facet S^1 'sees' the back of S^2

[4]Once again, a superscript number denotes a nodal quantity.

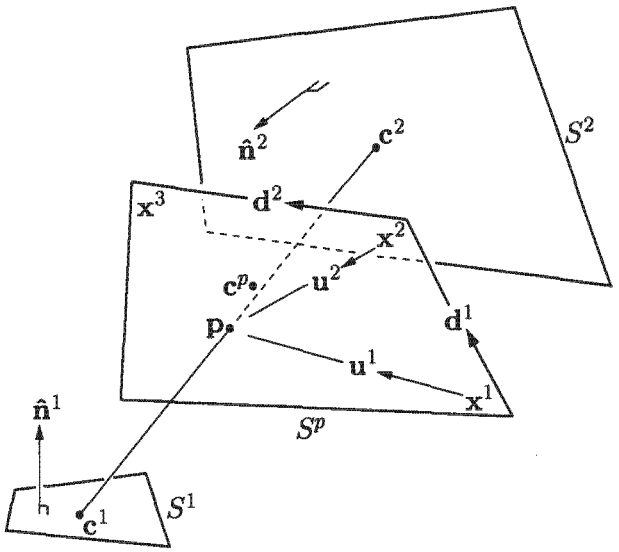

Figure 4.3: Nomenclature for two facets occluded by a third facet

- S^2 is 'behind' S^1
- There exists at least one other facet obscuring S^1's view of S^2. If some facet can be found such that the point, $\mathbf{p}$, lies within or on the border of the facet, then an obstruction to S^1's line of sight is found.

The algorithm that was implemented is listed in Algorithm 3. With regard to the third condition above, much of the algorithm is devoted to conditionally applying a series of tests to the point, $\mathbf{p}$, defined as the intersection of the line $\overline{\mathbf{c}^1\mathbf{c}^2}$ and the plane normal to $\hat{\mathbf{n}}^p$. The first test determines whether S^p could lie between S^1 and S^2. If it does then a second test determines whether $\mathbf{p}$ lies on one of the bounding line segments of S^p. If not then a final test determines whether $\mathbf{p}$ lies inside S^p. Thus, special attention was given to minimizing the computational cost through the selective application of these tests.

A limitation of Algorithm 3 is that, when finding an obstructing facet, it only considers the line of sight between the two centroids, $\mathbf{c}^1$ and $\mathbf{c}^2$. The algorithm was however found to be a good compromise between accuracy and speed, particularly when $F_{\max}$ is large.

Analytically Derived View Factor Expressions

The application of Stokes' Theorem [44, p 62] was used in (4.32) to reduce the integration over an area to a single contour integration around the boundary of the area, yielding

$$F_{mn} = \frac{1}{2\pi}\,\hat{\mathbf{n}}^m \cdot \oint_{\partial A^n} \frac{(\mathbf{c}^m - \mathbf{x}^*)}{|\mathbf{c}^m - \mathbf{x}^*|^2} \times \mathrm{d}\mathbf{x}^* \tag{4.38}$$

An exact solution to (4.38) was derived (see Appendix 7) for a view to a surface, S^n, consisting

Algorithm 3 Efficient computation of occlusion between radiating facets S^1 and S^2

$occl = 0$

{Does S^1 see back of S^2?}
if $\hat{\mathbf{n}}^2 \cdot (\mathbf{c}^2 - \mathbf{c}^1) > 0$ **then**
  $occl = 1$
  break {from n-loop}

{Is S^2 behind S^1?}
if $\hat{\mathbf{n}}^1 \cdot (\mathbf{c}^2 - \mathbf{c}^1) \leq 0$ **then**
  $occl = 1$
  break {from n-loop}

{Check for arrangement shown in Figure 4.3}
for $p = 1, \ldots, m-1, m+1, \ldots, n-1, n+1, \ldots, F_{\text{max}}$ and $occl < 1$ **do**
  if $\hat{\mathbf{n}}^p \cdot (\mathbf{c}^2 - \mathbf{c}^1) = 0$ **then**
    continue {with S^{p+1} because $S^p \parallel (\mathbf{c}^2 - \mathbf{c}^1)$ }

  $\mathbf{p} = \mathbf{c}^1 + t(\mathbf{c}^2 - \mathbf{c}^1)$ where $t = \dfrac{\hat{\mathbf{n}}^p \cdot (\mathbf{c}^p - \mathbf{c}^1)}{\hat{\mathbf{n}}^p \cdot (\mathbf{c}^2 - \mathbf{c}^1)}$

  {Could S^p possibly lie between S^1 and S^2?}
  if $0 < t < 1$ and $\hat{\mathbf{n}}^1 \cdot (\mathbf{p} - \mathbf{c}_1) > 0$ **then**

    $\mathbf{w}^i = \mathbf{d}^i \times \mathbf{u}^i$ for $i = 1, \ldots, 4$ {Utility cross–products}

    {Is $\mathbf{p}$ on the boundary of S^p?}
    for $i = 1, \ldots, 4$ and $occl < 1$ **do**

      {Is $\mathbf{p}$ on the line segment $\overline{d^i}$?}
      if $|\mathbf{w}^i| = 0$ **then**
        if $0 \leq \left((\mathbf{p} - \mathbf{c}_i) \cdot (\mathbf{d}^i) / |\mathbf{d}^i|^2 \right) \leq 1$ **then**
          $occl \longleftarrow \min(occl + \frac{1}{2}, 1)$
          break {from i-loop}

    {Does $\mathbf{p}$ lie within S^p?}
    if $\mathbf{w}^1 \cdot \mathbf{w}^j > 0 \quad \forall\, j = 2, 3, 4$ **then**
      $occl = 1$ {because $\mathbf{p}$ lies inside S^p}

if $occl = 0$ **then**
  $F_{12} = 0$
else
  $F_{12} = occl \times$ (computed view factor (Equation (4.39)))

of *sides* straight sides arbitrarily oriented with respect to S^m:

$$F_{mn} = \frac{1}{2\pi} \sum_{i=1}^{\substack{sides \\ of\ S^n}} \hat{\mathbf{n}}^m \cdot \frac{\boldsymbol{\omega}^i}{|\boldsymbol{\omega}^i|} \left[\arctan\left(\frac{\mathbf{d}^i \cdot \boldsymbol{\mu}^{i+1}}{|\boldsymbol{\omega}^i|} \right) - \arctan\left(\frac{\mathbf{d}^i \cdot \boldsymbol{\mu}^i}{|\boldsymbol{\omega}^i|} \right) \right] \tag{4.39}$$

where $\mathbf{d}^i = \mathbf{x}^{i+1} - \mathbf{x}^i$ evaluated on S^n, $\boldsymbol{\mu}^i = \mathbf{x}^i - \mathbf{c}^m$, and $\boldsymbol{\omega}^i = \mathbf{d}^i \times \boldsymbol{\mu}^i$. Physically, the vectors $\boldsymbol{\omega}^i$ represent the effect that the orientation of S^n relative to S^m has on the magnitude of F_{mn}. The more obliquely S^n is oriented relative to S^m the smaller will be $\boldsymbol{\omega}^i$, and hence, as expected, the smaller the view factor. The factors in square brackets represent the effect of separation between S^m and S^n. The larger the separation, the closer the vector $\boldsymbol{\mu}^{i+1}$ will be to $\boldsymbol{\mu}^i$ in both magnitude and direction.

The algorithm that was implemented to compute the entire database of non–zero view factors is listed in Algorithm 4.

Algorithm 4 View factor database computation with no symmetric facets

for $m = 1, \ldots, F_{\max} - 1$ **do**

{'forward' views}
for $n = m + 1, \ldots, F_{\max}$ **do**
Compute F_{mn} {using Algorithm 3 and Equation (4.39)}

{'backward' views}
for $n = 1, \ldots, m - 1$ **do**
$F_{mn} = \frac{A^n}{A^m} F_{nm}$ {reciprocity}

{Normalise views}
if $\sum_{n=1}^{F_{\max}} F_{mn} > 1$ **then**
Normalise views so that $\sum_{n=1}^{F_{\max}} F_{mn} = 1$

In the implementation, in order to minimise the use of storage space, only the non–zero view factors were stored, and the summations included the non–zero views only. The total number of computations required to compute the database is $O({F_{\max}}^3)$. Specifically it is proportional to

$$\begin{aligned} & \sum_{m=1}^{F_{\max}-1} \sum_{n=m+1}^{F_{\max}} \left(\sum_{p=1}^{m-1} + \sum_{p=m+1}^{n-1} + \sum_{p=n+1}^{F_{\max}} \right) 1 \\ = \; & \frac{1}{2} F_{\max}(F_{\max} - 1)(F_{\max} - 2) \end{aligned} \tag{4.40}$$

The size of the computation of the 'backward' views is insignificant and is therefore not included here.

4.3.4 Exploitation of Symmetry within the Cavity

The existence of planes of symmetry within the radiating cavity allows the radiant interaction in certain regions of the cavity to be inferred from other regions. Although the concept of symmetry is intuitively obvious, careful consideration is needed in order that it be exploited in this numerical model.

Reducing the Number of Radiosity Unknowns

Suppose that the assemblage of $F_{\max}$ facets comprising the cavity may now be partitioned into $F_{\mathcal{M}}$ *master* facets and $F_{\mathcal{S}}$ *slave* facets, so that

$$F_{\max} = F_{\mathcal{M}} + F_{\mathcal{S}} \tag{4.41}$$

As indicated in Figure 4.1, the radiating cavity comprises both the bounding surface (such as the casting furnace walls) and all interior surfaces (such as the exterior surfaces of the mould surrounding the solidifying metal).

A slave facet is one whose radiant behaviour may be inferred from the behaviour at one of the master facets. Physically, this inference may usually be attributed to a slave facets being geometrically symmetric to a master facet.

In this analysis the numbering of the facets will be ordered in such way that the set of master facets is given by $\{S^1, \ldots, S^{F_{\mathcal{M}}}\}$, and the set of slave facets is $\{S^{F_{\mathcal{M}}+1}, \ldots, S^{F_{\max}}\}$. Also, the slave facets of any given master facet will be numbered contiguously.

If $F_{\mathcal{S}}^n$ is the number of slaves that are symmetric to the n'th master facet, S^n, then by definition

$$F_{\mathcal{S}} = \sum_{n=1}^{F_{\mathcal{M}}} F_{\mathcal{S}}^n \tag{4.42}$$

The numbers $F_{\mathcal{S}}^n$ are not known at the start of the simulation. Indeed, for the analyst to prescribe all the master–slave relationships at the start of simulation would be an onerous task, especially if the geometry of the radiating cavity is large. One important objective in this work is to assist the analyst in this regard. The master–slave relationships will therefore be derived automatically at the start of the simulation from other data which pertain to the symmetries provided in the model definition. This will be discussed in detail later in this section.

With (4.41) and (4.42) it is then easy to see that the summation over all facets in (4.31) and (4.33) may be partitioned as:

$$\begin{aligned}\sum_{n=1}^{F_{\max}} G_{mn} q_o^n &= \sum_{n=1}^{F_{\mathcal{M}}} G_{mn} q_o^n + \sum_{n=1}^{F_{\mathcal{S}}} G_{m(F_{\mathcal{M}}+n)} q_o^{F_{\mathcal{M}}+n} \\ &= \underbrace{\sum_{n=1}^{F_{\mathcal{M}}} G_{mn} q_o^n}_{\text{master facets}} + \underbrace{\sum_{n=1}^{F_{\mathcal{M}}} \sum_{p=1}^{F_{\mathcal{S}}^n} G_{mI_{np}} q_o^{I_{np}}}_{\text{slave facets}}\end{aligned} \tag{4.43}$$

where further partitioning of the summation over the slaves was achieved using (4.42) and an index mapping function defined as[5]

$$I_{np} = F_{\mathcal{M}} + \sum_{q=1}^{n-1} F_{\mathcal{S}}^{q} + p \tag{4.44}$$

But, by symmetry

$$q_o^{I_{np}} = q_o^n \qquad \text{for } p = 1, \ldots, F_{\mathcal{S}}^n \text{ and } n = 1, \ldots, F_{\mathcal{M}}; \tag{4.45}$$

If (4.45) is inserted into (4.43), the system of equations in (4.33) may be decoupled as

$$\begin{aligned} \sum_{n=1}^{F_{\mathcal{M}}} G'_{mn} q_o^n &= \sigma \epsilon_m [T^m]^4 + \sigma \rho_m F_{ma} [T_a]^4 , \qquad m = 1, \ldots, F_{\mathcal{M}} \\ q_o^m &= \text{radiosity of a master counterpart,} \qquad m = F_{\mathcal{M}} + 1, \ldots, F_{\max} \end{aligned} \tag{4.46}$$

where now

$$G'_{mn} = G_{mn} + \rho_m \sum_{p=1}^{F_{\mathcal{S}}^n} F_{mI_{np}} \tag{4.47}$$

$F_{mI_{np}}$ is the view factor from the m'th master facet to the p'th slave of the n'th master. Therefore, even though the radiosities of the slave facets are strictly not needed, the symmetric slave regions of the cavity contribute to the heat balance in the master regions. This contribution is encapsulated in these view factors, and hence, the geometry of the symmetric regions must be accounted for in the models.

By exploiting symmetry in this way the number of unknowns has been reduced from $F_{\max}$ to $F_{\mathcal{M}}$, while the form of the equations for the unknown master radiosities has remained unchanged. Since most DS investment casting furnaces are axisymmetric in design, and since the components are usually cast in a clustered formation, it is often the case that $F_{\mathcal{M}} \ll F_{\max}$, resulting in substantial computational cost savings at each finite element time increment.

Algorithm 4 was modified accordingly by requiring that m sum from 1 to $F_{\mathcal{M}}$ instead of to $F_{\max} - 1$. The total number of computations required to create the database of view factors

[5]The integrity of this mapping function depends on contiguous numbering of the slave facets, as $F_{\mathcal{M}} + 1, F_{\mathcal{M}} + 2, \ldots, F_{\mathcal{M}} + F_{\mathcal{S}}^1, F_{\mathcal{M}} + F_{\mathcal{S}}^1 + 1, \ldots, F_{\mathcal{M}} + F_{\mathcal{S}}^1 + F_{\mathcal{S}}^2, \ldots, F_{\max}$. The value of I_{np} is then the global index of the p'th slave facet of the n'th master facet.

is now proportional to

$$\begin{aligned}
&\sum_{m=1}^{F_{\mathcal{M}}} \sum_{n=m+1}^{F_{\max}} \left(\sum_{p=1}^{m-1} + \sum_{p=m+1}^{n-1} + \sum_{p=n+1}^{F_{\max}} \right) 1 \\
&= \frac{1}{2} F_{\mathcal{M}} (2F_{\max} - F_{\mathcal{M}} - 1)(F_{\max} - 2) \\
&\longrightarrow \begin{cases} \frac{1}{2} F_{\max}(F_{\max} - 1)(F_{\max} - 2) & \text{as } F_{\mathcal{M}} \longrightarrow F_{\max} \\ (F_{\max} - 1)(F_{\max} - 2) & \text{as } F_{\mathcal{M}} \longrightarrow 1^{+} \end{cases}
\end{aligned} \tag{4.48}$$

Clearly then, as the number of symmetric faces increases, the number of computations reduces from $O({F_{\max}}^3)$ to $O({F_{\max}}^2)$

From (4.46) a modified Gauss–Seidel scheme may thus be written as shown in Algorithm 5.

Algorithm 5 Gauss–Seidel iterative scheme to exploit symmetry so that radiosities for only the $F_{\mathcal{M}}$ master facets need to be computed

$relError = relMaxResidual + 1$

while $relError > relMaxResidual$ **do**
  $relError = 0$

  for $m = 1, \ldots, F_{\mathcal{M}}$ **do**
    $q_o^m = \sigma \epsilon_m [T^m]^4 + \rho_m \sum_{\substack{n=1 \\ n \neq m}}^{F_{\mathcal{M}}} \left(F_{mn} + \sum_{p=1}^{F_S^n} F_{mI_{np}} \right) q_o^{*n} + \gamma \sigma \rho_m F_{ma} [T_a]^4$
    if $|q_o^m| > 0$ **then**
      if $|(q_o^m - q_o^{*m})/q_o^m| > relError$ **then**
        $relError = |(q_o^m - q_o^{*m})/q_o^m|$

    $q_o^{*m} = q_o^m$

The *Master–Slave* Relationship for Symmetric Facets

The exploitation of symmetry in (4.46) and Algorithm 5 is predicated on knowing F_S^m — the number of slaves for each master facet S^m. For large and complex cavities containing many planes of symmetry, manually specifying the F_S^m values and identifying which slave facets are symmetric to which master facets would be difficult and time–consuming, and may even negate the benefits of exploiting symmetry in the first place. To address this problem, a novel algorithm was developed to allow the analyst to specify the *master–slave* symmetry relationships at a high level without regard to relationships between individual facets. Using the interface to the software (Chapter 5), the analyst is only required to define for each symmetry: a master

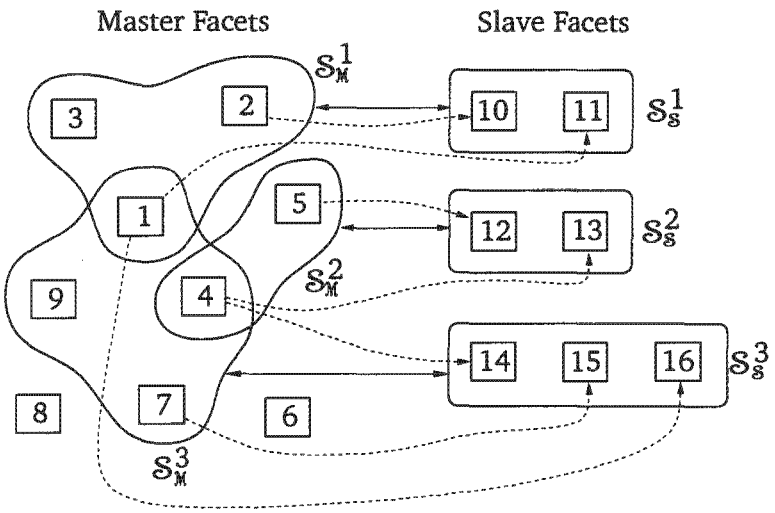

Figure 4.4: Three hypothetical *master–slave* set relations in a radiating cavity. The numbered boxes represent facet indices. The solid lines represent linkages that are provided by the analyst. The broken lines are possible linkages that are computed using Algorithm 6

facet set, a slave facet set, the type of symmetry, and other data specific to the symmetry type (Chapter 5).

In order to describe the algorithm fully, the following definitions are needed:

$$
\begin{array}{lll}
\mathcal{S}_{\max} & — & \text{total number of symmetries within the cavity} \\
\mathcal{S}^A & — & \text{the } A\text{'th symmetry operation} \\
\mathcal{S}_{\mathcal{M}}^A & — & \text{set of master facet indices for the } A\text{'th symmetry} \\
|\mathcal{S}_{\mathcal{M}}^A| & — & \text{the number of master facets in the set } \mathcal{S}_{\mathcal{M}}^A \\
\mathcal{S}_{\mathcal{M}b}^A & — & \text{the } b\text{'th facet index in the master set } \mathcal{S}_{\mathcal{M}}^A \\
\mathcal{S}_{\mathcal{S}}^A & — & \text{set of slave facet indices for the } A\text{'th symmetry} \\
|\mathcal{S}_{\mathcal{S}}^A| & — & \text{the number of slave facets in the set } \mathcal{S}_{\mathcal{S}}^A \\
\mathcal{S}_{\mathcal{S}b}^A & — & \text{the } b\text{'th facet index in the slave set } \mathcal{S}_{\mathcal{S}}^A
\end{array}
\tag{4.49}
$$

From these definitions it is clear that the numbers $F_{\mathcal{S}}^m$ $(= F_{\mathcal{S}}^{\mathcal{S}_{\mathcal{M}b}^A}$, for some not necessarily unique pair $(A, b))$, must be initialised by the algorithm. $\mathcal{S}_{\max}$ and the definition of each symmetry, $\mathcal{S}^A$, are specified by the analyst. This obviously includes specifying the master facet index set, $\mathcal{S}_{\mathcal{M}}^A$, for each $\mathcal{S}^A$. The slave facet index set, $\mathcal{S}_{\mathcal{S}}^A$, is either supplied by the analyst during model definition, or is generated automatically. This will be elaborated further below.

To illustrate the use of these definitions in (4.49), three symmetry set relations are shown diagrammatically in Figure 4.4. The relationships between the master and slave facets sets, as indicated by solid arrows, are specified by the analyst. In the figure $F_{\mathcal{S}}^1 = F_{\mathcal{S}}^4 = 2$, $F_{\mathcal{S}}^2 = F_{\mathcal{S}}^5 = F_{\mathcal{S}}^7 = 1$ and $F_{\mathcal{S}}^3 = F_{\mathcal{S}}^6 = F_{\mathcal{S}}^8 = F_{\mathcal{S}}^9 = 0$.

In order to compute these values for general symmetry relations, the algorithm proceeds by considering each slave facet, $S^{\mathcal{S}_{\mathcal{S}b}^A}$, of each symmetry in turn. Using the parameters defining

the type of symmetry, $S^{\mathcal{S}^A_{\mathcal{S}b}}$ is transformed geometrically (to $S'^{\mathcal{S}^A_{\mathcal{S}b}}$ say) onto the A'th symmetry's master set, $\mathcal{S}^A_{\mathcal{M}}$. Then the master facet in $\mathcal{S}^A_{\mathcal{M}}$ which is 'nearest' to $S'^{\mathcal{S}^A_{\mathcal{S}b}}$ is found (as $S^{\mathcal{S}^A_{\mathcal{M}c}}$ for some c, say) and is selected as being the master of the untransformed facet, $S^{\mathcal{S}^A_{\mathcal{S}b}}$. And the number, $F_{\mathcal{S}}^{\mathcal{S}^A_{\mathcal{M}c}}$, of slave facets of the master, $S^{\mathcal{S}^A_{\mathcal{M}c}}$, is therefore incremented by one. The implemented algorithm is shown in Algorithm 6.

Algorithm 6 Determination of the $F_{\mathcal{S}}^m$ *master–slave* linkages for each slave facet, as shown in Figure 4.4

{Initialise the $F_{\mathcal{S}}^m$ to zero}
for $m = 1, \ldots, F_{\mathcal{M}}$ **do**
  $F_{\mathcal{S}}^m = 0$

{Consider each slave facet of each symmetry}
for $A = 1, \ldots, \mathcal{S}_{\max}$ **do**
  for $b = 1, \ldots, \left|\mathcal{S}^A\right|$ **do**

    Define position and orientation of $S'^{\mathcal{S}^A_{\mathcal{S}b}}$ from $\mathcal{S}^A : S'_{\mathcal{S}^A_{\mathcal{S}b}} \mapsto S_{\mathcal{S}^A_{\mathcal{S}b}}$

    {Find master facet 'nearest' to $S'^{\mathcal{S}^A_{\mathcal{S}b}}$}
    $\Delta_{\min} = \infty$
    for $c = 1, \ldots, \left|\mathcal{S}^A_{\mathcal{M}}\right|$ **do**
      $\Delta =$ 'distance' between $S'^{\mathcal{S}^A_{\mathcal{S}b}}$ and $S^{\mathcal{S}^A_{\mathcal{M}c}}$ (Equation (4.50))
      if $|\Delta| < |\Delta_{\min}|$ **then**
        $m = \mathcal{S}^A_{\mathcal{M}c}$
        $\Delta_{\min} = \Delta$

    Register slave facet $S^{\mathcal{S}^A_{\mathcal{S}b}}$ as a slave to S^m

    {Increment number of facets which are slaves of master facet}
    $F_{\mathcal{S}}^m \longleftarrow F_{\mathcal{S}}^m + 1$

In the algorithm the 'distance' between two facets is defined as a weighted sum of the distance between the centroids and the distance between the two points located at the heads of the two normal vectors (Figure 4.5):

$$\Delta = \alpha_1 \sqrt{\left(\mathbf{c}'^n - \mathbf{c}^m\right)^2} + \alpha_2 \sqrt{\left[\left(\mathbf{c}'^n + \hat{\mathbf{n}}'^n\right) - \left(\mathbf{c}^m + \hat{\mathbf{n}}^m\right)\right]^2} \tag{4.50}$$

However, if the two facets point in opposite directions, so that $\hat{\mathbf{n}}^m \cdot \hat{\mathbf{n}}'^n < 0$, then the facets are considered far apart. The parameters α_1 and α_2 weigh the importance of position and orientation, respectively. In the software implementation, values for the parameters were set at $\alpha_1 = \alpha_2 = 1$.

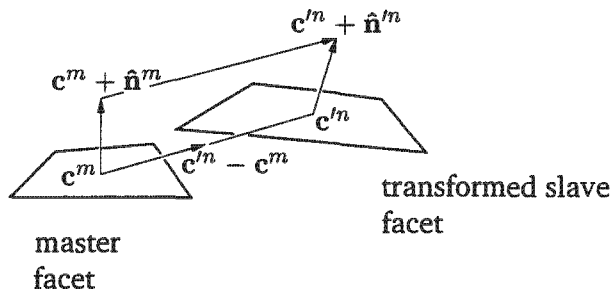

Figure 4.5: Nomenclature for calculating the 'distance' between two facets

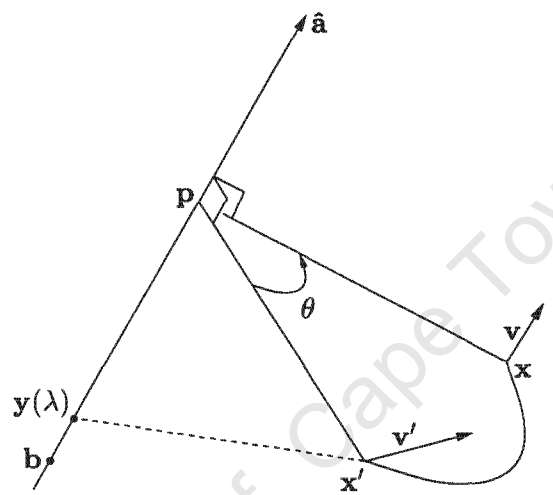

Figure 4.6: Rotation of a point and a vector in three dimensions

The handling of cyclic, tranlational and reflective symmetry will now be discussed. In all these three cases (4.50) will be used as a measure of nearness.

Cyclic Symmetry

Although Algorithm 6 does not depend on the type of symmetries present within the cavity, the most common type found within a DS casting furnace is cyclic symmetry.

A rotation in $\mathbb{R}^3$ from an arbitrary point $\mathbf{x}'$ to the point $\mathbf{x}$ is completely defined by: a unit vector, $\hat{\mathbf{a}}$, parallel to the axis of rotation; a point, $\mathbf{b}$, lying anywhere on the axis; and, an angle of rotation, θ, as shown in Figure 4.6.

Suppose, hypothetically, that the facet S'^m is known (as defined by the parameters in (4.37))[6], and that a symmetric facet, S^n, exists at or near the rotation of S'^m about the axis. Since the facet area, A'^m, is invariant under rotations, I need only determine the vector, $\hat{\mathbf{n}}$, and the

[6]Defining the rotation in a seemingly 'backward' fashion as rotating S'^n onto S^n is consistent with the analyst's intuitive idea of rotating a master facet set onto its slave set, and not the other way round. The analyst is then able define $\hat{\mathbf{a}}$, $\mathbf{b}$ and θ with respect to the master facet set.

coordinates of the centroid, $\mathbf{c}$, in order to relate S^n to S'^n. This will be carried out here by developing general formulae for the rotation of an arbitrary point and vector, and then by applying them to the centroid and normal vector.

The coordinates of the point $\mathbf{p}(\mathbf{x}')$ lying on the axis are first found as the focus of the arc swept through $\mathbf{x}'$. An arbitrary point, $\mathbf{y}(\lambda)$, lying on the axis is given by

$$\mathbf{y}(\lambda) = \mathbf{b} + \lambda\hat{\mathbf{a}} \qquad \text{for } \lambda \in \mathbb{R} \tag{4.51}$$

By minimizing the distance $|\mathbf{x}' - \mathbf{y}(\lambda)|$ so that

$$\frac{\mathrm{d}}{\mathrm{d}\lambda}\left|\mathbf{x}' - \mathbf{y}(\lambda)\right| = 0 \tag{4.52}$$

the coordinates of $\mathbf{p}$ as a function of $\mathbf{x}'$ are found to be

$$\mathbf{p}(\mathbf{x}') = \mathbf{b} + \big((\mathbf{x}' - \mathbf{b}) \cdot \hat{\mathbf{a}}\big)\hat{\mathbf{a}} \tag{4.53}$$

Defining the vector function $\mathbf{u}(\mathbf{x}') = \mathbf{p}(\mathbf{x}') - \mathbf{x}'$, the coordinates of the point $\mathbf{x}$ in Figure 4.6 are then determined using the following simple identities from analytic Euclidean geometry:

$$\begin{aligned} \mathbf{u}(\mathbf{x}') \cdot \big(\mathbf{p}(\mathbf{x}') - \mathbf{x}\big) &= |\mathbf{u}(\mathbf{x}')|^2 \cos(\theta) && \text{(dot product)} \\ \mathbf{u}(\mathbf{x}') \times \big(\mathbf{p}(\mathbf{x}') - \mathbf{x}\big) &= |\mathbf{u}(\mathbf{x}')|^2 \sin(\theta)\,\hat{\mathbf{a}} && \text{(cross product)} \\ \big(\mathbf{p}(\mathbf{x}') - \mathbf{x}\big) \cdot \hat{\mathbf{a}} &= 0 && \text{(vectors perpendicular)} \end{aligned} \tag{4.54}$$

The solution to the unknown $\mathbf{x}$ may be found easily as

$$\mathbf{x} = \mathbf{p}(\mathbf{x}') - \mathbf{u}(\mathbf{x}')\cos(\theta) + \big(\mathbf{u}(\mathbf{x}') \times \hat{\mathbf{a}}\big)\sin(\theta) \tag{4.55}$$

Interestingly, Equation (4.55) appears to be a generalization of a rotation in two dimensions. If $\mathbf{b} = \mathbf{p}(\mathbf{x}') = (x'_p, y'_p, 0)$, $\hat{\mathbf{a}} = (0, 0, -1)$ and $\mathbf{x}' = (x', y', 0)$, then (4.55) and (4.53) give

$$\mathbf{x} = \begin{bmatrix} x'_p \\ y'_p \\ 0 \end{bmatrix} - \begin{bmatrix} \cos(\theta) & \sin(\theta) & 0 \\ -\sin(\theta) & \cos(\theta) & 0 \\ 0 & 0 & 1 \end{bmatrix} \begin{bmatrix} x'_p - x' \\ y'_p - y' \\ 0 \end{bmatrix} = \mathbf{p}(\mathbf{x}') - \mathbf{R} \cdot \mathbf{u}(\mathbf{x}') \tag{4.56}$$

which is the usual formula for two–dimensional rotations.

To rotate an arbitrary vector $\mathbf{v}'$, the above analysis is applied to the points $\mathbf{x}'$ and $\mathbf{x}' + \mathbf{v}'$ to give

$$\begin{aligned} \mathbf{v} = [\mathbf{p}(\mathbf{x}' + \mathbf{v}') - \mathbf{p}(\mathbf{x}')] - [\mathbf{u}(\mathbf{x}' + \mathbf{v}') - \mathbf{u}(\mathbf{x}')]\cos(\theta) \\ + \big[\big(\mathbf{u}(\mathbf{x}' + \mathbf{v}') - \mathbf{u}(\mathbf{x}')\big) \times \hat{\mathbf{a}}\big]\sin(\theta) \end{aligned} \tag{4.57}$$

Using (4.53), (4.57) simplifies to

$$\mathbf{v} = \mathbf{v}'\cos(\theta) + \big(\mathbf{v}' \cdot \hat{\mathbf{a}}\big)\big(1 - \cos(\theta)\big)\hat{\mathbf{a}} - \big(\mathbf{v}' \times \hat{\mathbf{a}}\big)\sin(\theta) \tag{4.58}$$

If the A'th symmetry is a cyclical symmetry, then Equations (4.55) and (4.58) completely define the mapping $\mathcal{S}^A : S'^{\mathcal{S}^A_{\mathcal{S}b}} \mapsto S^{\mathcal{S}^A_{\mathcal{S}b}}$ for $b = 1, \ldots, \left|\mathcal{S}^A_{\mathcal{S}}\right|$. Therefore, in order to determine the position and orientation of $S'^{\mathcal{S}^A_{\mathcal{S}b}}$ in Algorithm 6, (4.55) and (4.58) are applied in reverse to the centroid and normal vectors of $S^{\mathcal{S}^A_{\mathcal{S}b}}$:

$$\begin{aligned} \mathbf{c}' &= \mathbf{p}(\mathbf{c}) - \mathbf{u}(\mathbf{c})\cos(-\theta) + \big(\mathbf{u}(\mathbf{c}) \times \hat{\mathbf{a}}\big)\sin(-\theta) \\ \hat{\mathbf{n}}' &= \hat{\mathbf{n}}\cos(-\theta) + \big(\hat{\mathbf{n}} \cdot \hat{\mathbf{a}}\big)\big(1 - \cos(-\theta)\big)\hat{\mathbf{a}} - \big(\hat{\mathbf{n}} \times \hat{\mathbf{a}}\big)\sin(-\theta) \end{aligned} \tag{4.59}$$

Translational Symmetry

If the DS casting furnace possesses translational symmetry then the position and orientation of $S'^{\mathcal{S}^A_{\mathcal{S}b}}$ are determined by

$$\begin{aligned} \mathbf{c}' &= \mathbf{c} + (-d)\hat{\mathbf{a}} \\ \hat{\mathbf{n}}' &= \hat{\mathbf{n}} \end{aligned} \tag{4.60}$$

where d is the distance along direction $\hat{\mathbf{a}}$ from a master facet set to its slave set.

Reflective Symmetry

By inspection of Figure 4.7 it is easy to see that the formulae for reflective symmetry are:

$$\begin{aligned} \mathbf{c}' &= \mathbf{c} - \big(2(\mathbf{c} - \mathbf{b}) \cdot \hat{\mathbf{a}}\big)\hat{\mathbf{a}} \\ \hat{\mathbf{n}}' &= \hat{\mathbf{n}} - (2\hat{\mathbf{n}} \cdot \hat{\mathbf{a}})\hat{\mathbf{a}} \end{aligned} \tag{4.61}$$

where $\mathbf{b}$ is any point on the plane and $\hat{\mathbf{a}}$ is the unit vector perpendicular to the mirror plane.

4.3.5 Symmetry between dissimilar Objects

The greatest benefit to be derived through the development of Algorithm 6 is the increased flexibility in the definition of symmetries in modelling DS casting processes. Planes of symmetry may be defined between geometrically non–identical regions of the mesh. In particular, for a given symmetry, the number of slave facets, $\left|\mathcal{S}^A_{\mathcal{S}}\right|$, need not equal the number of master facets, $\left|\mathcal{S}^A_{\mathcal{M}}\right|$; and therefore, the facet mesh density of the set $\mathcal{S}^A_{\mathcal{S}}$ could be much lower than that of $\mathcal{S}^A_{\mathcal{M}}$, as shown in Figure 4.8.

By representing the slave symmetric regions of the cavity with a coarser mesh, the total number of radiating facets, $F_{\max}$, may be substantially reduced, which, from (4.48), can result in large computational cost savings. The simulations presented in §6.4 demonstrate the effectiveness of this algorithm.

Careful handling of geometrical symmetries is one way in which the size of the radiant interaction computations has been reduced. However, in the case of modelling DS casting processes, an additional way is developed here. This will be discussed now.

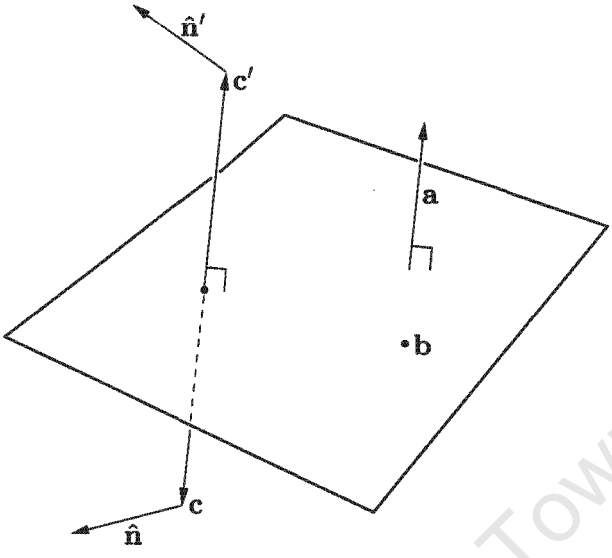

Figure 4.7: Reflection of a point and a vector about a mirror plane

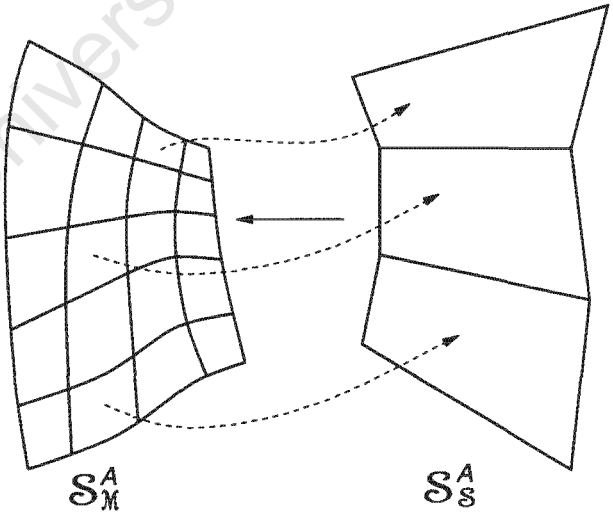

Figure 4.8: Symmetry between two dissimilar geometries

4.3.6 Modelling the Interactions within the DS Casting Furnace

As was discussed in §2.2, directional solidification is achieved by the prescribed irradiation of the casting and mould from the furnace heaters and walls while the supporting ram is lowered out of the furnace at a carefully controlled rate (Figure 2.4).

In order to simulate this radiation, the set of facets representing the furnace heaters and walls must be made to move relative to the remaining facets. Unfortunately, this incurs additional computational cost at each time increment because the view factor database must, in general, be recomputed whenever the geometry changes.

Depending on the nature of these changes, it may be possible to limit the computations to a subset of view factors. Indeed, with respect to a DS furnace cavity, the views between those facets which are coincident with the radiating surfaces of the casting geometry will not change with time, and therefore need not be recomputed at each time increment. However, it is difficult to predict reliably at the start of the simulation which of the remaining views will not change with time. For example, a view between a master facet and a symmetric slave facet that was obscured by an intermediate facet at an early time may cease to be obscured at a later time.

A simplification algorithm was developed in this work to eliminate this additional computational cost. It does, however, rely on being able to represent the furnace heaters and walls with a relatively simple facet mesh, as shown in Figure 4.9. The motion of the ram and the casting is simulated by varying the temperatures of the furnace and wall facets instead of varying the geometry. In this way, the view factor database then needs only to be computed once at the start of the simulation.

Initially the temperature of all except the lowest facets is set at T_h — the constant temperature of the furnace heaters. The lowest facets are set to T_c — the constant temperature of the furnace walls. This is equivalent to the baffle being located below the casting at an axial position, b_0, say. If the ram is lowered at a rate $\mathbf{v}_w(t) = v_w(t)\,\hat{\mathbf{n}}_w$, then the baffle position at any time relative to the casting geometry in the direction $(-\hat{\mathbf{n}}_w)$ is given by

$$b(t) = b_0 + \int_0^t v_w(t')\,\mathrm{d}t' \tag{4.62}$$

In directional casting procedures it is common to sub–divide the withdrawal stage into $n_{\max}$ sub–intervals, $\{(t_{n-1}, t_n] \,|\, n = 1, \ldots, n_{\max}\}$, with $v_w(t) = v_{wn}$ for $t \in (t_{n-1}, t_n]$. The expression for the baffle position in (4.62) then reduces to

$$b(t) = b_{n-1} + v_{wn}(t - t_{n-1}) \quad \text{for } t_{n-1} < t \leq t_n \tag{4.63}$$

with $b_{n-1} = b_0 + \sum_{i=1}^{n-1} v_{wi}(t_i - t_{i-1})$.

During the simulation, temperatures of the furnace facets are specified depending on the position of the facet's centroid relative to the position of the baffle. Temperatures are reduced

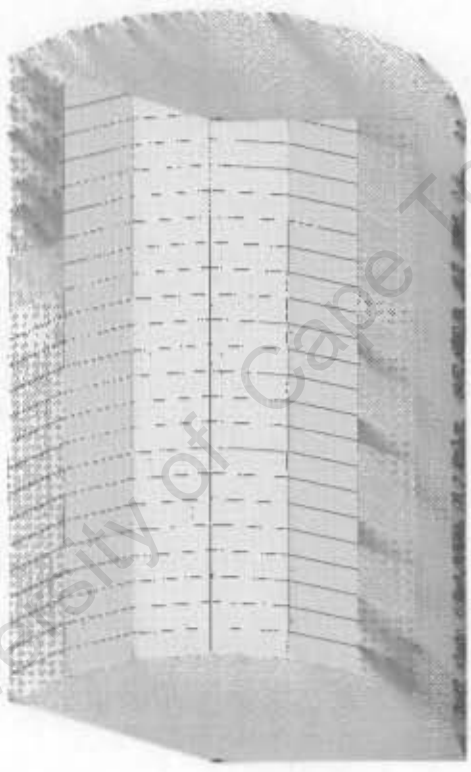

Figure 4.9: Partial view of a typical facet mesh representing the furnace heaters and walls

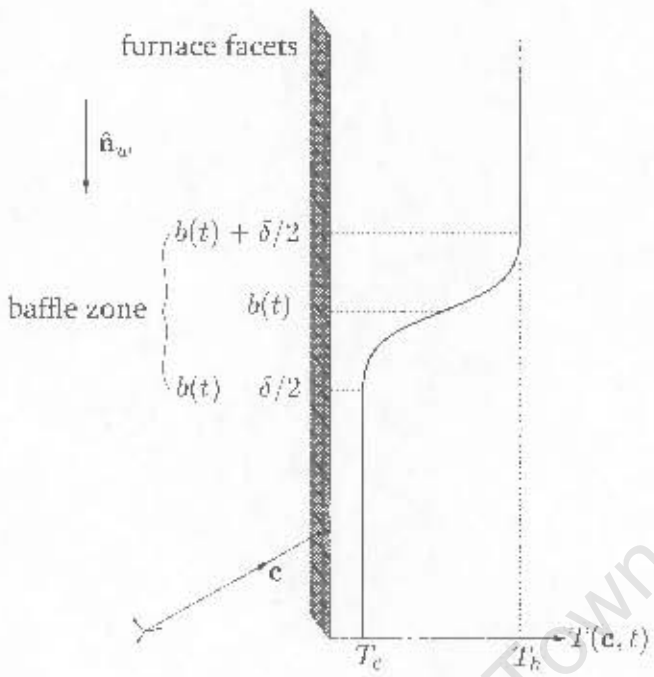

Figure 4.10: Temperature variation in direction $(-\hat{\mathbf{n}}_w)$ at time t on the facets representing the furnace heaters and walls

gradually from T_h to T_c in an axial zone centred at the baffle position. For a furnace facet with centroid located at $\mathbf{c}$ the prescribed temperature is then

$$T(\mathbf{c}, t) \begin{cases} T_h; & \bar{c} > b(t) - \delta/2 \\ \dfrac{T_h + T_c}{2} + \dfrac{T_h - T_c}{2} \sin\left(\pi \dfrac{\bar{c} - b(t)}{\delta}\right); & b(t) - \delta/2 \leq \bar{c} \leq b(t) + \delta/2 \\ T_c; & \bar{c} < b(t) - \delta/2 \end{cases} \tag{4.64}$$

)

where $\bar{c} = \mathbf{c} \cdot (-\hat{\mathbf{n}}_w)$ is the projection of $\mathbf{c}$ in the direction $(-\hat{\mathbf{n}}_w)$, and δ is the height of the baffle zone, as shown Figure 4.10.

Values for the following constants are to be supplied when setting up a model: T_h, T_c, b_0, $\hat{\mathbf{n}}_w$, δ, and the set of sampling points $\{(t_n, v_{wn}) \ n = 1, \ldots, n_{\max}\}$.

It must be noted that this algorithm represents a specialisation applicable only to directional casting processes in which:

- the geometry of the furnace, namely, the heaters, walls, baffle plate, ceiling, and floor (Figure 2.4), is sufficiently simple that its effect on the transient heat fluxes can reasonably be accounted for with a furnace mesh of the form shown in Figure 4.9

- the temperature of the various surfaces comprising geometry of the furnace chamber is held constant, i.e., is independent of the temperature evolution of the exterior mould surfaces. In the experimental programme accompanying this simulation work, measurements of the furnace surface temperatures confirmed this constancy.

Refinement of the modelling of DS furnaces would require the existence of the furnace ceiling to be accounted for as being distinct from the heating elements. It is likely that, even after a state of thermal equilibrium in the hot zone has been reached, the temperature of the ceiling is lower than the temperature of the heating elements. However, the results shown in §6.4 appear not to be sensitive to this lack of refinement. A comparison of computed and measured histories at points higher up along the cast bar might have indicated otherwise.

4.3.7 Temperature–Dependent Emissivity

The dependence of emissivity on temperature is modelled by a set of piecewise continuous sub–intervals $\{(T_{m-1}, T_m] \,|\, m = 1, \ldots, m_{\max}; T_{m-1} \neq T_m\}$. The emissivity is assumed to vary linearly over each sub–interval so that

$$\epsilon(T) = \frac{T_m - T}{T_m - T_{m-1}}\epsilon_{m-1} + \frac{T - T_{m-1}}{T_m - T_{m-1}}\epsilon_m \quad \text{for } T_{m-1} < T \leq T_m \tag{4.65}$$

with $\epsilon_m \equiv \epsilon(T_m)$ for $m = 0, \ldots, m_{\max}$.

Since the radiating cavity is comprised of different material surfaces, with each material surface having its own dependence on emissivity, a set of sampling points, $\{(T_m, \epsilon_m) \,|\, m = 1, \ldots, m_{\max}\}$, must be provided for each material surface.

4.4 Coupling Radiation and Conduction Calculations during Transient Analysis

The numerical model of radiant interactions described in §4.3 is independent of the finite element model of conduction within the casting (see §4.2), except for a coupling between the two models at the material interfaces. In order for the former to provide reliable heat flux values as a boundary condition to the latter, the coupling must ensure that:

- each radiating exterior elemental face in the finite element mesh exactly coincides with one master facet in the mesh of the radiating cavity
- thermal data at each coincident facet must be kept up to date for the duration of the transient finite element calculations
- the radiation calculations provide reliable estimates of not only the average heat flux over each elemental face, but also the flux at the integration points.

4.4.1 Extrapolation to the Integration Points

The finite element model will supply the radiation model with the current temperature at an integration point, α, of an exterior elemental face. If the face coincides with the m'th facet, S^m, then $q^{m\alpha}$—an approximate value for the net heat flux at the integration point—is found by truncating a Taylor expansion about the average facet temperature, T^m, as[7]

$$\begin{aligned} &q^m(T^1,\ldots,T^{m-1},T^m+\Delta T^{m\alpha},T^{m+1},\ldots,T^{F_{\mathcal{M}}}) \\ &\approx q^{m\alpha} \equiv q^m(\ldots,T^{m-1},T^m,T^{m+1},\ldots)+\left[\frac{\partial q^m}{\partial T^m}(\ldots,T^{m-1},T^m,T^{m+1},\ldots)\right]\Delta T^{m\alpha} \end{aligned} \tag{4.66}$$

where $T^{m\alpha}$ is the temperature of the α'th integration point supplied to the facet S^m by the finite element calculation, and $\Delta T^{m\alpha} \equiv T^{m\alpha} - T^m$ is the temperature 'correction'. The 'corrected' quantity $q^{m\alpha}$ is precisely that which is supplied back to the finite element calculation as the radiation heat flux at the integration point. It is exactly the quantity required by (4.23) and (4.12).

From (4.35), the derivative in (4.66) is

$$\frac{\partial q^m}{\partial T^m} = \begin{cases} \dfrac{\mathrm{d}}{\mathrm{d}T^m}\left(\dfrac{\epsilon_m}{\rho_m}\right)\left[\sigma[T^m]^4 - q_o^m\right] + \dfrac{\epsilon_m}{\rho_m}\left[4\sigma[T^m]^3 - \dfrac{\partial q_o^m}{\partial T^m}\right] & \rho_m \neq 0 \\ \dfrac{\mathrm{d}\epsilon_m}{\mathrm{d}T^m}\left[\sigma[T^m]^4 - q_i^m\right] + \epsilon_m\left[4\sigma[T^m]^3 - \dfrac{\partial q_i^m}{\partial T^m}\right] & \text{otherwise} \end{cases} \tag{4.67}$$

How are $\partial q_o^m/\partial T^m$ and $\partial q_i^m/\partial T^m$ evaluated? Recall that in Algorithm 5 (§4.3.4) an iterated estimate for q_o^m was given by:

$$q_o^m = \sigma\epsilon_m[T^m]^4 + \rho_m \sum_{\substack{n=1 \\ n\neq m}}^{F_{\mathcal{M}}} \left(F_{mn} + \sum_{p=1}^{F_{\mathcal{S}}^n} F_{mI_{np}}\right) q_o^{*n} + \gamma\sigma\rho_m F_{ma}[T_a]^4$$

Since the radiosity, q_o^m, depends most strongly on T^m, the derivatives $\partial q_o^{*n}/\partial T^m$ for all $n \neq m$ are neglected. Hence

$$\begin{aligned} \frac{\partial q_o^m}{\partial T^m} \approx{}& \sigma\frac{\mathrm{d}\epsilon_m}{\mathrm{d}T^m}[T^m]^4 + 4\sigma\epsilon_m[T^m]^3 \\ &+ \frac{\mathrm{d}\rho_m}{\mathrm{d}T^m}\sum_{\substack{n=1 \\ n\neq m}}^{F_{\mathcal{M}}}\left(F_{mn} + \sum_{p=1}^{F_{\mathcal{S}}^n} F_{mI_{np}}\right) q_o^{*n} + \gamma\sigma\frac{\mathrm{d}\rho_m}{\mathrm{d}T^m}F_{ma}[T_a]^4 \end{aligned} \tag{4.68}$$

Similarly, by inspection of (4.36) it is easy to deduce that

$$\frac{\partial q_i^m}{\partial T^m} \approx 0 \tag{4.69}$$

[7]The functional notation used here follows that introduced in (4.28), and emphasises the fact that q^m depends implicitly on the temperatures of *all* facets.

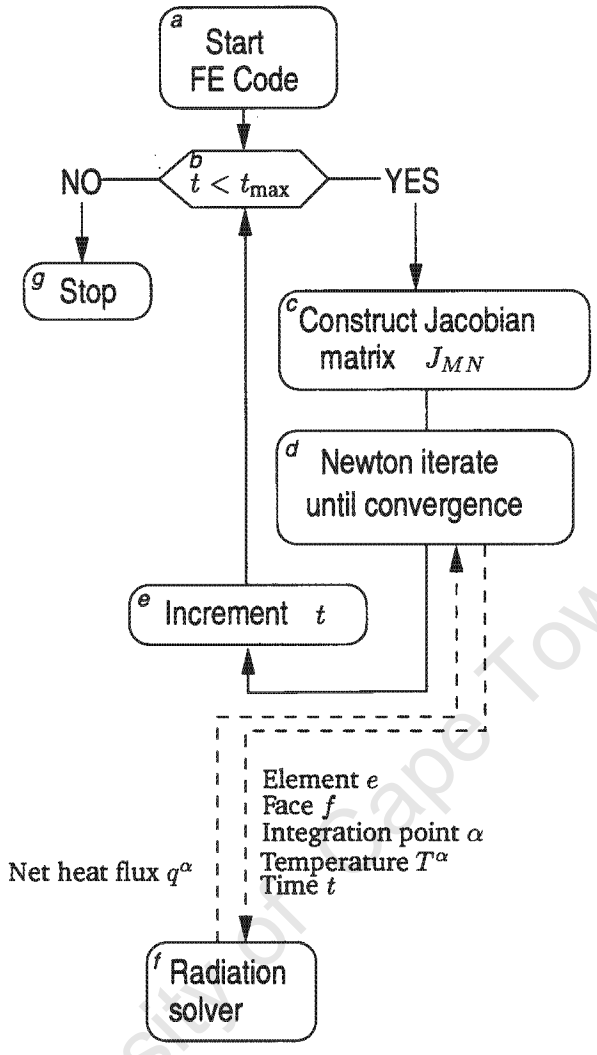

Figure 4.11: Flow diagram for the finite element solver

With (4.67), (4.68) and (4.69) inserted into (4.66), an important result is obtained in that the radiation calculations are able to provide accurate estimates to the net heat flux at the integration points even though the calculations themselves assume the facets to be isothermal. Indeed, without the implementation of this algorithm, the number of iterations for each time increment of the finite element computations was found to be high (refer to Chapter 6).

4.4.2 The Flow Diagrams

The coupling between the FE computation and the radiation computation (Algorithm 5) is shown schematically in Figure 4.11.

The algorithm to extend the standard finite element analysis to address the radiation computations is shown diagramatically in Figure 4.12. The various algorithms discussed in §4.3 are implemented. At the start of the simulation (Box *a*, Figure 4.12) the basic radiating system

is set up (Box *b*), and a database of view factors is created. If the geometry of the cavity has not changed from a previous simulation, then the database will simply be uploaded from secondary storage (Box *d*). At the start of each finite element iteration (Box *f*) the average thermal quantities (Equation (4.28)) of each master radiating facet which is coincident with an elemental face will be updated using the most up-to-date values at the integration points on the elemental face (Box *j*). The thermal quantities of each symmetric facet will then also be updated by its corresponding master facet. The temperatures of the furnace facets are then updated (Box *h*) according to (4.63) and (4.64). The average radiosities and net heat fluxes for the master facets for the iteration are then computed (Box *i*). Regardless of whether the radiation solver was entered at the start of an FE iteration, the average net heat flux is extrapolated to the integration point (Box *k*) which is then submitted to the FE solver (Box *l*).

4.5 Summary

A numerical solution to the transfer of heat energy during vacuum investment casting processing was developed in this chapter. A finite element model of conduction within the casting was coupled to a *net–radiation* model applied within the furnace cavity.

A Galerkin isoparametric finite element formulation using first–order hexahedral elements was developed. The well–known backward–difference temporal algorithm, together with a modified Newton iterative method, was used to solve the non–linear equations at selected instants during the solidification history of a casting.

The basic finite element model was then extended to account for the radiant interactions. Modelling these interactions is known to be notoriously expensive computationally. Special attention was therefore given to the development of an efficient radiation model—a model which avoids the need to compromise on numerical accuracy and stability.

In modelling the interactions, the geometry of the DS furnace was assumed to be comprised of any number of bilinear facets, with some of these facets being exactly coincident with some of the exterior elemental faces of the finite element mesh. By further assuming that the radiant quantities do not vary significantly over each facet, the description of the interactions was reduced to a system of linear equations for the unknown radiosities.

The Gauss–Seidel relaxation method is able to exploit the diagonal dominance of the resulting system matrix. It was therefore chosen to approximate updates to the facet radiosities at the start of each Newton iteration.

The major part of the computational cost is attributable to computing the database of view factors. The cost is roughly proportional to the cube of the number of facets. A reduction of this cost was achieved along three fronts, namely: reducing the number of required view factors; reducing the cost of calculating each view factor; and, reducing the cost associated with each Newton iteration.

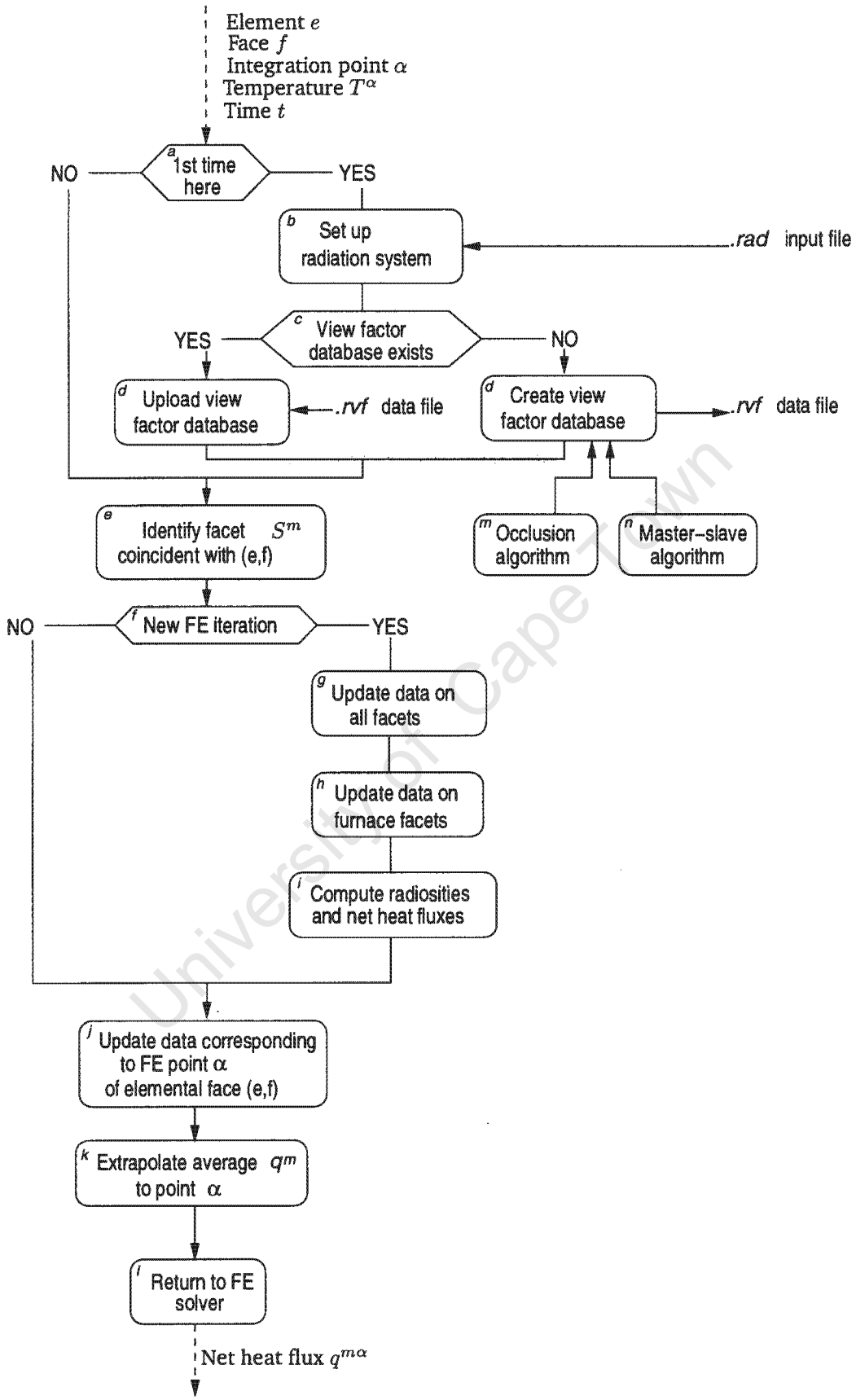

Figure 4.12: Flow diagram for the radiation solver

By applying a reciprocal relationship between view factors, and then by developing a novel algorithm for exploiting symmetry within the cavity, the number of required view factors was reduced.

The 'symmetry algorithm' provided flexibility in the definition of symmetries which may be present in the model geometries. Planes of symmetry may be defined between regions of the mesh which are geometrically non–identical. Symmetric *slave* regions of the geometry may be represented with facet meshes that are coarser than the corresponding *master* regions. This substantially reduces the size of the view factor database when compared with representing the symmetric regions with identical geometries. Furthermore, the algorithm allows the analyst to specify symmetry at a higher abstracted level without regard to the relationships between individual facets.

The cost associated with each view factor calculation was reduced firstly by deriving an analytic expression for the view factor itself, and secondly by developing an efficient algorithm to check for the presence of occlusion. In the algorithm a series of 'tests' are conditionally applied, with the cheapest tests applied first.

Finally, the cost associated with each Newton iteration was reduced by eliminating the need to recompute the view factor database at the start of the iteration. This was achieved by selectively varying the temperatures of the facets representing the furnace geometry instead of varying the geometry itself.

An inherent source of numerical inaccuracy and instability rests with the coupling between the finite element and radiation calculations at the exterior elemental face. The former assumes a bilinear variation of the thermal quantities over the surface around the integration points, while the latter assumes no variation at all. By extrapolating the computed average net heat flux to the integration point, an accurate estimate at the integration point was computed. This extrapolation was achieved by truncating the Taylor expansion of the heat flux about the average facet temperature to the temperature at the integration point.

Chapter 5

Software Model

5.1 Introduction

FORTRAN is arguably still the predominant computer language used to write numerical modelling programs. Extensive numerical software libraries written in FORTRAN are widely available. Indeed, many of these are freely available from the Internet [84, 85].

However, despite its popularity, standard FORTRAN has certain limitations which obfuscate coding and subsequent maintenance of the code, and which reduce the efficiency of the resulting compiled executables. For this reason it was decided to implement the models presented in the previous chapter using the C language.

Many of the data required to represent and compute the numerical models were structured hierarchically using facilities provided by C. The advantages of this structured approach are:

- Code readability is enhanced
- The ability to isolate 'bugs' is enhanced
- Most importantly, the performance of the code may be enhanced though more efficient computer memory management and data manipulation.

In this chapter, aspects of the software implementation which pertain to this organisation of data will be discussed. The validity of the third point above will be demonstrated, the user interface will be discussed.

A knowledge of C is presumed, as well as an understanding of the idea that a C pointer variable stores a computer memory address.

5.2 Dynamic Structured Data

The most important data types will be presented in this section.

5.2.1 Facets, Nodes and Views

All data pertaining to a radiating facet were encapsulated using a new C variable type called a FACET, defined as follows:

```
1  typedef unsigned int POSINT;     /* Positive integers */
2  typedef double REAL;             /* Real variables are stored in */
3                                   /*      double precision */
4  typedef struct {
5     POSINT num,                   /* Facet number */
6     REAL T, emiss,                /* Facet temperature and emissivity */
7          q0, dq0_dT, d2q0_dT2,    /* Average radiosity and derivatives */
8          q,  dq_dT,  d2q_dT2,     /* Average net heat flux and derivatives */
9          area,
10         normal[3], centroid[3],
11         viewSum;
12    POSINT nodes;                 /* Number of nodes on the facet */
13    NODE *(*node);                /* Dynamic array of pointers to NODEs */
14    POSINT totalViews,
15           forwardViews;
16    VIEW *view;                   /* Dynamic array of VIEWs from this facet */
17    POSINT symmFacets;            /* Number of symmetric slave FACETs */
18    FACET **symmFacet;            /* Dynamic array of pointers to FACETs */
19                                  /*      which are symmetric to this FACET */
20    INTEGPOINT *integPoint;       /* Dynamic array of integration point data */
21 } FACET;
```

By dynamically allocating memory to store $F_{\max}$ FACETs, the exact amount space is automatically allocated for all the data. This raises to a higher level the management of the computer memory needed to store the facet data. The m'th radiating facet, S^m, then corresponds exactly with the m'th FACET, `facet[m]`, in the dynamic array, `facet`.

A given node in the facet mesh can be shared by numerous facets. This raises the problem of duplication of nodal data across FACETs. If, in a separate structure called a NODE, each nodal number is associated with the nodal coordinates, then this duplication is avoided. Each FACET simply maintains a dynamic array of NODE memory addresses rather than an array of NODEs themselves. With a NODE defined as:

```
22 typedef struct {
23    POSINT num;                   /* Node number */
24    REAL x[3];                    /* Nodal coordinates */
25 } NODE;
```

the node field in the FACET structure is the dynamic array of nodes *pointers* to NODEs, so that, for example, the nodal data for the third node on the m'th facet is pointed to by[1]

[1] In C all arrays start with 0 as the first index, so that the third node as written is actually the fourth node in the array, and the m'th facet as written is actually the $(m+1)$'th facet.

```
*((facet+m)->node+3)
```

The position vector for this node is then

```
(*((facet+m)->node+3))->x
```

The value of the second coordinate is pointed to by

```
(*((facet+m)->node+3))->x+2
```

and the value itself is therefore

```
*((*((facet+m)->node+3))->x+2)
```

This expression can be written more simply in C as either

```
(*(facet[m].node[3])).x[2]
```

or

```
facet[m].node[3]->x[2]
```

Storing pointers to NODEs on each FACET has an additional advantange. If any nodal data were to change during a simulation, then the changes would remain local to the NODEs while still being registered in the FACETs.

The data for each integration point is grouped together in the INTEGPOINT structure, defined as:

```
26 typedef struct {
27    POSINT num;                  /* Integration point number */
28    REAL T,                      /* Temperature at integration point */
29         q;                      /* Net heat flux at */
30 } INTEGPOINT;
```

A VIEW of a given facet is defined as the association of the value of a view factor and a pointer to a FACET, where the FACET field corresponds to a second radiating facet which is visible by the first:

```
31 typedef struct {
32    FACET *viewedFacet;          /* Pointer to a viewed FACET */
33    REAL value;                  /* View factor value */
34 } VIEW;
```

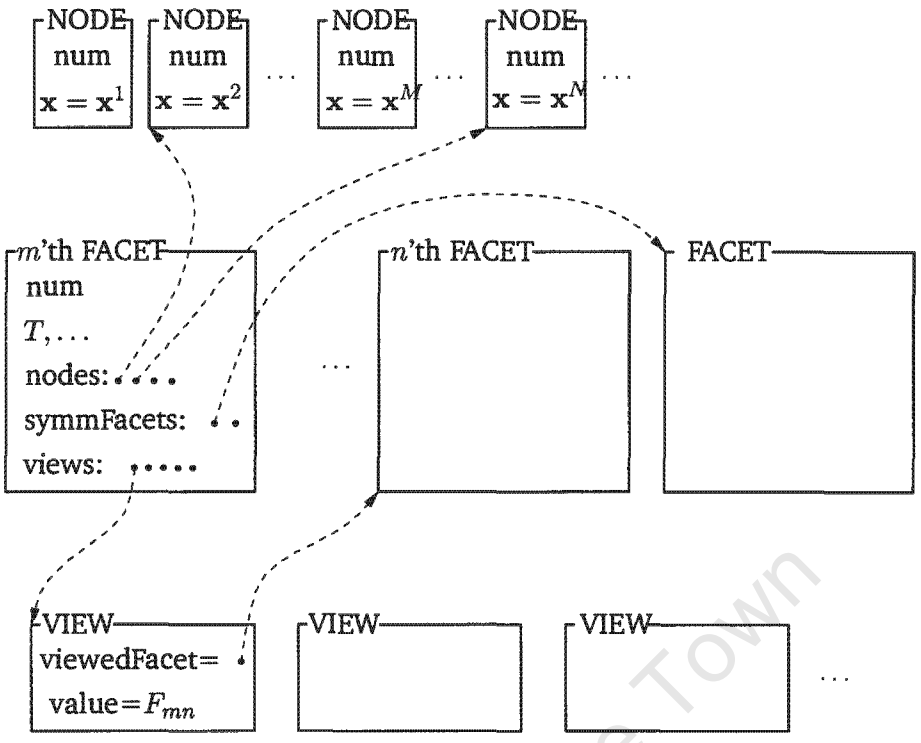

Figure 5.1: Typical relationships between the FACET, NODE and VIEW data types. The larger dots represent pointers, and the broken lines represent the values of these pointer variables

The total number of views for each facet, S^m, will be computed and stored at `facet[m].totalViews`. A dynamic array of VIEWs from `facet[m]` will then be allocated and initialised using the `view` field of the FACET structure. From facet S^m all the data of a visible facet is then immediately available without making recourse to arrays of indices, as is often done with FORTRAN. For example, the number of the q'th facet visible from S^m is

```
((facet+m)->view+q)->viewedFacet->num
```

or simply

```
facet[m].view[q].viewedFacet->num
```

and the actual value of the view factor is

```
facet[m].view[q].value
```

Typical pointer–mediated relationships between the structures discussed in this section are shown diagrammatically in Figure 5.1. All the pointer arrays are allocated and initialised at the start of the simulation (Box *b*, Figure 4.12, §4.4.2).

5.2.2 Symmetries

If a furnace cavity has $\mathcal{S}_{\max}$ planes of geometric symmetry, then the data for these symmetries are stored in a dynamic array of length $\mathcal{S}_{\max}$, where each member of the array is a structure defined as follows:

```
35 typedef struct {
36     char type[MAXSTRLEN],        /* Cyclic, translational or reflective */
37          condition[MAXSTRLEN];   /* Generated or based on proximity */
38     FACETSET *master,            /* Pointer to master FACET set */
39              *slave;             /* Pointer to slave FACET set */
40     REAL vector[3],
41          point[3],
42          distance,
43          angle;
44 } SYMMETRY;
```

A set of FACETs is defined using the following structure:

```
45 typedef struct {
46     char name[MAXSTRLEN];        /* Name of FACET set */
47     POSINT facets;               /* Number of FACETs in the set */
48     FACET *(*facet);             /* Dynamic array of pointers to FACETs */
49 } FACETSET;
```

From these structured definitions, the A'th symmetry type is, for example, stored as `symm[A].type`, and the number of the b'th slave facet of the A'th symmetry is[2]

$$\mathcal{S}^A_{\mathcal{S}b} = \texttt{symm[A].slave->facet[b]->num.}$$

At the start of the simulation the fields `vector`, `point`, `distance` and `angle` will be assigned values that are appropriate for the symmetry `type` (§4.3.4). If, for a given symmetry, the value of the `condition` field is equal to the string `"GENERATE"`, then a mesh representing the symmetric slave part will be generated automatically. The additional FACETs will be placed in a unique FACETSET, and the `slave` pointer will be set equal to the address of this new FACETSET. The `master` pointer will point to a FACETSET containing FACETs which correspond to radiating facets which must have been defined by the analyst beforehand (see §5.4).

If, on the other hand, the value of `condition` is equal to `"PROXIM"`, then the symmetric slave geometry will *not* be generated, and both the `master` and `slave` FACETSETs must be defined by the analyst. The `condition` field was introduced specifically to cater for the specification of planes of symmetry between dissimilar geometrical objects, as discussed in §4.3.5.

Using Algorithm 6, for each FACET a dynamic array of pointers to the symmetric slave FACETs is allocated and initialised, so that for a given radiating master facet, S^m, $F^m_{\mathcal{S}}$= `facet[m].symmFacets`, and the temperature of the q'th facet symmetric to S^m is accessible as `facet[m].symmFacet[q]->T`.

[2]The facet number $\mathcal{S}^A_{\mathcal{S}b}$ was defined in Equation (4.49) of §4.3.4.

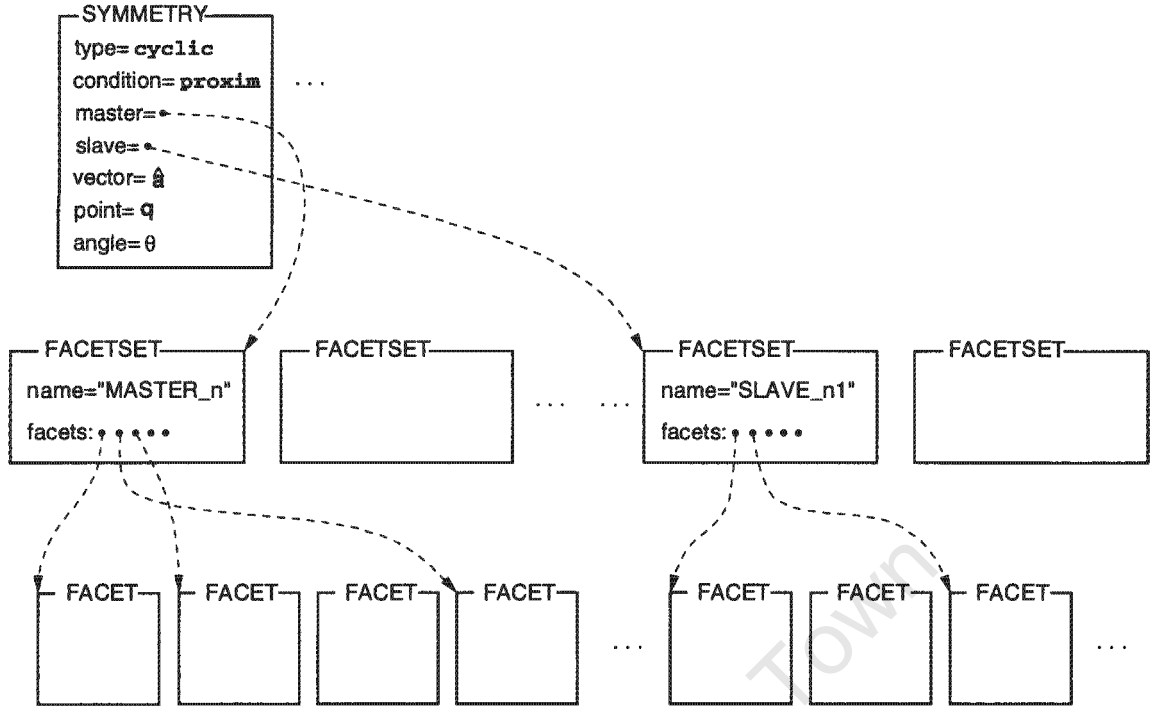

Figure 5.2: Hierarchical organisation of geometric symmetries using sets of FACETs

5.2.3 The DS Casting Furnace

All the variables defined in §4.3.6 that are required to simulate the motion of the ram relative to the furnace are encapsulated in a variable conveniently known as `furn` which is of type `DSFURNACE`. This type is defined as follows:

```
50 typedef struct {
51     REAL direction[3],              /* Withdrawal direction vector */
52          Tcold, Thot,
53          baffleZoneWidth;
54     POSINT baffleSamples;           /* Number of (position,time) samples */
55     REAL *bafflePosn, *baffleTime;
56     POSINT facets;                  /* Number of FACETs representing the furnace */
57     FACET *(*facet);                /* Dynamic array of pointers to these FACETs */
58 } DSFURNACE;
```

The number of radiating facets representing the DS furnace walls is then stored as `furn.facets`, and the temperature of the q'th facet, for example, is accessed as `furn.facet[q]->T`. The motivation for implementing this structured approach for the furnace data is the same as in the case of the definition of `FACETs` and `NODEs` above. Any changes (such as a change in facet temperature) that may be applied to the set of facets defining the furnace geometry will imediately be registered in the `furn` variable via the pointer `furn.facet`.

The required samples for the variation in time of the baffle position (Equation (4.63)) are stored in the arrays `furn.bafflePosn` and `furn.baffleTime` which are both of length `furn.baffleSampl`

5.2.4 Temperature–Dependent Emissivity

To introduce temperature–dependent emissivities into the computations, as discussed in §4.3.7, recourse is made to the FACETSET type defined above (source line 45). An instant of type FACETSET is associated with the set of sampling points, $\{(T_m, \epsilon_m] \mid m = 1, \ldots, m_{\max}; T_{m-1} \neq T_m\}$, in a new variable of type EMISSIVITY, defined as:

```
59 typedef struct {
60    FACETSET *facetset;          /* FACETs defining material surface */
61    REAL *T,                     /* Array of temperature samples */
62         *value;                 /* Array of emissivity samples */
63    POSINT samples;              /* Number of samples in arrays */
64 } EMISSIVITY;
```

An array, to be named emiss, and of length equal to the number of different material surfaces, is then set up with its entries each of type EMISSIVITY. The m'th sampling point for the emissivity of the b'th material surface is then stored in the array as (emiss[b].T[m],emiss[b].value[m]).

5.3 Efficient Data Manipulation

It is easy to show that, starting from the facet array, to access the value of a nodal coordinate as facet[m].node[3]->x[2] requires no less than 9 operations involving either addition or pointer dereferencing. Similarly, to access the temperature of the q'th symmetric facet using facet[m].symmFacet[q]->T requires 7 such operations.

This high overhead negatively affects the performance of the computations. However, by making careful use of temporary local pointer variables during the computations, this overhead may be reduced. These pointers are 'local' in the sense that they have just sufficient scope to be able, for the required duration, to point to variables within the organisational hierarchy.

To illustrate this, the number of computations required to update the thermal quantities of the symmetric slave facets using data at the master facets will be considered here. The thermal quantities are temperature, emissivity, radiosity, and the radiosity's first and second derivatives with respect to temperature. Without recourse to local pointers, the updating is done using a statement of the form

facet[m].symmFacet[q]->*quantity* = facet[m].*quantity*

and the number of computations is (using (4.41) and (4.42))

$$\sum_{m=0}^{F_{\mathcal{M}}-1} \sum_{q=0}^{F_{\mathcal{S}}^m-1} 10 \times 5 = 50 F_{\mathcal{S}} \tag{5.1}$$

In the following C code recourse *is* made to local pointers, so that the updating is done using a statement of the form

symmFacet->*quantity* = facet->*quantity*

```
1  void UpdateSymmFacets( FACET *facetStart,       /* Array of */
2                                                  /* master FACETs */
3                         POSINT masterFacets )    /* Number of */
4                                                  /* master FACETs */
5  {
6    FACET *facet,          /* Temporary local pointer to a FACET */
7          *symmFacet,      /* Temporary local pointer to a */
8                           /*      symmetric slave FACET */
9          *(*pSymmFacet); /* Temporary local pointer to the address */
10                          /*      of a symmetric slave FACET */
11   POSINT m,q;
12
13   /*
14    * Start at the beginning of the array
15    * of master FACETs
16    */
17   facet = facetStart;
18
19   for( m = 0;  m < masterFacets;  m++ ) {
20
21      /*
22       * Start at the beginning of the array
23       * of addresses of slave FACETs
24       */
25      pSymmFacet = facet->symmFacet;
26
27      /*
28       * Update attributes of each slave
29       */
30      for( q = 0;  q < facet->symmFacets;  q++ ) {
31
32         /*
33          * Work with contents of the current
34          * slave FACET address
35          */
36         symmFacet = *pSymmFacet;
37
38         /*
39          * Update the slave's attributes by
40          * dereferencing symmFacet appropriately
41          */
42         symmFacet->T         = facet->T;
43         symmFacet->emiss     = facet->emiss;
44         symmFacet->rad       = facet->rad;
```

```
45          symmFacet->dRad_dT   = facet->dRad_dT;
46          symmFacet->d2Rad_dT2 = facet->d2Rad_dT2;
47
48          /*
49           * Point to the next slave FACET address
50           */
51          pSymmFacet++;
52
53        }
54
55        /*
56         * Point to the next master FACET
57         */
58        facet++;
59    }
60
61    return;
62 }
```

The required number of computations is then

$$\sum_{m=0}^{F_{\mathcal{M}}-1}\left[2+\sum_{q=0}^{F_{\mathcal{S}}^{m}-1}(1+5\times 4+1)+1\right]=3F_{\mathcal{M}}+22F_{\mathcal{S}} \tag{5.2}$$

and therefore, from (5.1) and (5.2), the use of local pointers will produce computational cost savings whenever $3F_{\mathcal{M}}+22F_{\mathcal{S}}<50F_{\mathcal{S}}$, i.e., whenever $F_{\mathcal{S}}>\frac{3}{28}F_{\mathcal{M}}$.

5.4 The User–Interface

The radiating cavity is completely defined in a single input file. The format of this file was designed to closely resemble the 'free' format of an ABAQUS input file [23]. Third–party finite element mesh generators which are capable of producing ABAQUS input files could then be used with minimum effort to generate a facet mesh [3].

The input file may by broken down into five sections. These sections will be described briefly as follows, using extracts from an actual input file:

Global Data

```
1  ** This line is a comment
2  *RADIATION, %RESIDUAL=0.1, CYCLES=50
```

[3] In fact, the commercial software MSC/ARIES was used to generate a mesh for the model of a clustered casting simulation discussed in §6.4. The mesh for this model is shown in Figure 6.24. The automatic mesh generation capabilities of MSC/ARIES made it possible to specify, with minimum effort, the existence of the internal material boundaries between the metal, the mould and the chill plate.

The value of %RESIDUAL×100 is equal to *relMaxResidual* in Algorithm 2 and Algorithm 5. The parameter CYCLES is the maximum allowable number of iterations to reach convergence. The code will exit with an error if more iterations are required.

Geometry Data

```
3  *NODE
4     1,  1.1, 2.2, 3.3
5     2,  4.4, 5.5, 6.6
6     .   .   .
7     .   .   .
8  *FACET, TYPE=DGR3D4, FSET=SHELL
9     1,  7,8,9,10
10    2,  8,2,6,4
11    .   .   .
12    .   .   .
13 *FACET, TYPE=DGR3D3, FSET=SHELL
14    11,  11,33,55
15    .   .   .
16    .   .   .
17 *FACET, TYPE=DGR3D4, FSET=SLAVE1
18    22,  71,81,91,101
19    .   .   .
20    .   .   .
21 *FACET, TYPE=DGR3D4, FSET=FURNACE
22    33,  72,18,92,102
23    .   .   .
24    .   .   .
```

Both 3-noded and 4-noded facets may be specified. In this case facets belonging to three sets have been created, namely SHELL, SLAVE1 and FURNACE.

Thermal Properties

```
25 *SIGMA
26    5.729e-12
27 ** W/cm^2/K^4
28 *ABSOLUTE ZERO
29    -273.16
30 ** so that I can work in the centigrade scale
31 *AMB TEMP
32    20.0
33 *TEMP
34    SHELL,   850.
35    FURNACE, 1460.
36    11,      905.
```

```
37     .   .   .
38     .   .   .
39 *EMISSIVITY, FSET=SHELL
40     0.8  , 300.
41     0.85 , 800.
42     0.515, 1300.
43     0.45 , 2000.
44 *EMISSIVITY, FSET=FURNACE
45     0.5  , 650.
46     0.9  , 1600.
```

A value for the Stefan–Boltzmann constant is specified using the *SIGMA line. If a value for a constant ambient temperature is given using the *AMB TEMP line, then the boolean switch, γ, in Algorithm 5 (§4.3.4) will set to unity, and a view, F_{ma}, to the ambient environment will be computed. Using *TEMP initial temperatures are specified either for all facets belonging to a facet set or for individual facets. Four sampling points (§4.3.7) were given for the emissivity of the facets in the SHELL set, and two were given for the FURNACE facets.

Symmetry Definitions

Suppose a plane of cyclic symmetry (§4.3.4) exists between the geometries of the facet sets SHELL and SLAVE1. If the axis of rotation, $\mathbf{a} = (0,0,1)$, passes through the point $\mathbf{b} = (0,0,0)$, and if SHELL and SLAVE1 are 60° apart, with SHELL as the master set, then the symmetry must be defined as follows:

```
47 *SYMMETRY, TYPE=ROTATE, CONDITION=PROXIM
48     SLAVE1,  SHELL,  0,0,0,  0,0,1,  60
49 ** slave,    master,    b,       a,    theta
```

If, on the other hand, a symmetric slave geometry has not been defined explicity, but is to be generated automatically at an angle 120° from the SHELL, then the symmetry is defined as:

```
60 *SYMMETRY, TYPE=ROTATE, CONDITION=GENERATE
51     SHELL,  0,0,0,  0,0,1,  120
52 ** master,    b,       a,    theta
```

Directional Casting Specification

```
53 *DIRECTIONAL CASTING, FSET=FURN, DIRECTION=(0,0,1)
```

The facets in the FURN set comprise the DS furnace geometry. The furnace moves in the direction $-\hat{\mathbf{n}}_w = (0,0,1)$ relative to the casting (see §4.3.6).

```
54 *INITIAL BAFFLE POSN
55    1.1
56 *BAFFLE, SPEED, INC
57 ** cm, seconds
58 ** 5 min hold time
59    0, 300
60 ** 0.4cm/min forever
61    .006666666, 99999
```

The initial baffle position along the direction $-\hat{\mathbf{n}}_w$ is $b_0 = 1.1$cm; and two samples of the withdrawal speed, v_w, are specified.

```
62 *WALL TEMP
63    20.0
64 *FURNACE TEMP
65    1460.0
66 *BAFFLE RANGE
67    6.3
68 **
69 *END
```

The furnace wall and heater temperatures are given as 20 °C and 1460 °C respectively, and the width of the baffle zone is 6.3cm.

5.5 Summary

Many of the data required to represent and compute the numerical models were structured hierarchically. Numerous abstract data types were defined using facilities provided by the C language in order that closely related data items may be associated in a single variable. The defined types included:

- `FACET` — An encapsulation of: a facet number; basic thermal quantities, e.g., temperature and radiosity; geometric quantities, e.g., facet area and centroid; nodes; views; and symmetric slave facets
- `FACETSET` — An array of facet addresses and a set name
- `NODE` — A node number and its coordinates
- `VIEW` — A viewed facet address and the view factor value
- `INTEGPOINT` — An integration point
- `EMISSIVITY` — Temperature dependent emissivity associated with a facet set

- `SYMMETRY` — An association between the type of the symmetry, the real–valued data defining it, and a master and slave facet set
- `DSFURNACE` — Data required to simulate directional solidification and a set of facet addresses defining the furnace geometry.

This hierarchical organisation of data enabled more efficient management of the computer memory. This, however, may incur a higher computational cost than in the case of an unstructured organisation of data because many pointer dereferences and additions may be needed to access a datum located at a low level in the hierarchy. To eliminate this extra cost, extensive use was made of temporary 'local' pointer variables. This was illustrated by considering C code to update the thermal quantities of the symmetric slave facets.

The format of the single input file was discussed briefly by considering extracts from an actual source file.

In the next chapter specific examples of casting models will be presented.

Chapter 6

Results and Discussion

Four models are considered, in order of increasing geometric complexity and computational problem size. In the first model a simple radially insulated conducting rod in considered to be losing heat via radiation at one end to a flat plate. This model serves merely to validate the numerical solution scheme against a radiating boundary condition which can be expressed analytically.

The second model is of a simple hypothetical equiaxed investment casting of one and two rectangular bars. The third model is of a directional casting of two axisymmetric objects which were cast as single components. Finally, a model of a directional casting consisting of a cluster of six components will be considered.

An experimental programme was carried out in tandem with the numerical modelling effort. The vacuum investment casting facilities at the Division for Materials Science and Technology—a division of the CSIR[1]—were used.

Results of both the experimential and modelling work have been recorded in a series of CSIR reports. These reports have not been published in the public domain, but are accessible on request to the CSIR [86]–[92].

A technological objective of the Specialty Metals Programme within the Division is to improve the performance of Nickel-based superalloy components, such as those found in many modern turbine jet engines. To this end, attention in the Programme is directed at casting process design, cast component design, and superalloy design. The thrust of the work in this thesis naturally lies in the domain of casting process design.

An essential piece of equipment in the experimental programme was the actual directional vacuum investment casting furnace. The furnace is essentially identical to that shown in Figure 2.4 on page 9. Experimentally measured data were obtained by rigging actual casting runs with 'Type R' (Pt/Pt-Rh) thermocouple wiring.

[1] Council for Scientific and Industrial Research, South Africa

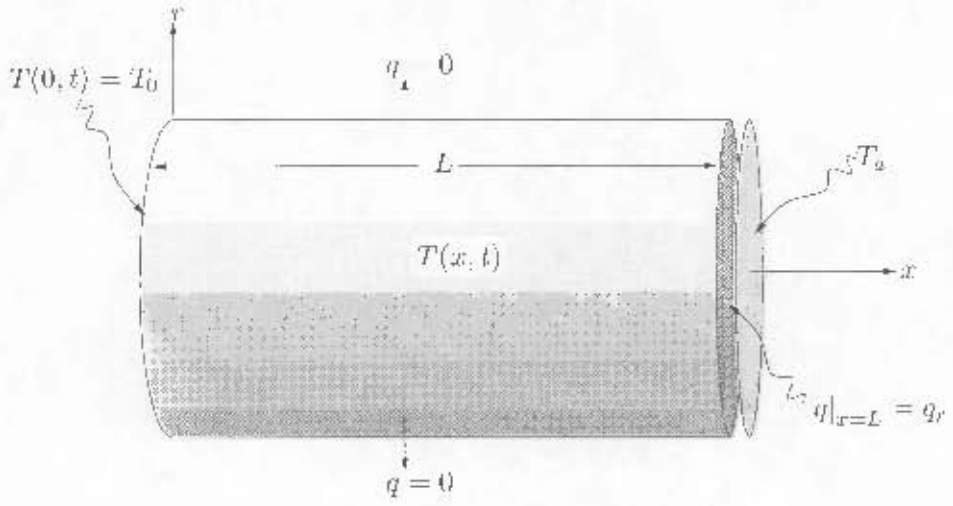

Figure 6.1: Simple longitudinally conducting rod, insulated radially and radiating at one end. (Not to scale)

6.1 Simple Radially Insulated Conducting and Radiating Rod

Figure 6.1 represents a simple conduction/radiation configuration in which the radiant interaction can be expressed analytically. This serves as a useful test case against which certain aspects of the numerical treatment of radiation in §4.3 can be compared.

Model Description

As shown in Figure 6.1, a radially insulated axisymmetric rod loses heat at one end via radiation to a flat plate whose temperature is fixed at T_a. The plate is assumed to be located close enough against one end of the rod that the interaction between the rod and the plate accounts for all the radiation. The initial temperature of the rod is T_0, and the temperature at $x = 0$ is assumed to be fixed at T_0.

Equation (3.6) predicts the evolution of the temperature field in the conducting rod. Assuming that the thermal conductivity of the rod is constant, and applying the simple change of variables

$$\xi(x) = \frac{1}{L}\,x, \quad \tau(t) = \frac{k}{\rho_m C_p L^2}\,t$$

where L is the length of the rod, (3.6) may be expressed as

$$\frac{\partial^2 T(\xi,\tau)}{\partial \xi^2} = \frac{\partial T(\xi,\tau)}{\partial \tau} \quad \text{for } 0 < \xi < 1, \quad \text{and } \tau \geq 0 \tag{6.1}$$

subject to the initial condition $T = T_0$ for $\tau = 0$. The boundary condition (3.16) at $x = 0$ becomes $T = T_0$ at $\xi = 0$, while the boundary condition at $x = L$ becomes $q = q_r$ at $\xi = 1$.

This radiating boundary condition may be expressed in an approximate closed form. The system of equations (4.31) for the radiosities of a set of radiating facets comprising a radiating cavity is now expressed simply as

$$q_{oL} - (1 - \epsilon_L)q_{oa} = \sigma\epsilon_L T_L^4$$
$$q_{oa} - (1 - \epsilon_a)q_{oL} = \sigma\epsilon_a T_a^4$$

where q_{oL} is now the radiosity of the butt end of the rod at $x = L$, ϵ_L is the rod's total hemispherical emissivity at $x = L$, and $T_L(\tau)$ stands for $T(1, \tau)$—the temperature of the rod at $x = L$. The corresponding quantities q_{oa}, ϵ_a and T_a apply to the flat radiating plate butted against (but not touching) the rod at $x = L$. The temperatures T_L and T_a are expressed in units Kelvin.

The solution in terms of the as yet unknown temperature, T_L, is

$$\begin{aligned} \frac{\epsilon_L + \epsilon_a - \epsilon_L\epsilon_a}{\sigma} q_{oL} &= \epsilon_L T_L^4 + \epsilon_a(1 - \epsilon_L)T_a^4 \\ \frac{\epsilon_a + \epsilon_L - \epsilon_a\epsilon_L}{\sigma} q_{oa} &= \epsilon_a T_a^4 + \epsilon_L(1 - \epsilon_a)T_L^4 \end{aligned} \tag{6.2}$$

But the radiosity of a radiating surface element is the sum of the directly emitted and the reflected incident energies (Equation (3.54)):

$$\begin{aligned} q_{oL} &= \sigma\epsilon_L T_L^4 + (1 - \epsilon_L)q_{iL} \\ \Rightarrow \quad q_{iL} &= \frac{1}{1 - \epsilon_L}(q_{oL} - \sigma\epsilon_L T_L^4) \end{aligned} \tag{6.3}$$

where q_{iL} is the total incident energy per unit surface area at $x = L$.

Finally, using (6.2) and (6.3), the net radiant heat transfer per unit surface area at $x = L$ is

$$\begin{aligned} q_r(T_L) &= q_{oL} - q_{iL} \\ &= \sigma\frac{1}{1/\epsilon_L + 1/\epsilon_a - 1}(T_L^4 - T_a^4) \equiv \sigma\epsilon_{\text{eff}}(T_L^4 - T_a^4) \end{aligned}$$

And the "natural" boundary condition at $x = L$ may thus be expressed explicitly as

$$-\frac{k}{L}\left.\frac{\partial T(\xi, \tau)}{\partial \xi}\right|_{\xi=1} = \sigma\epsilon_{\text{eff}}\left[T^4(\xi, \tau)\big|_{\xi=1} - T_a^4\right] \tag{6.4}$$

The presence of the fourth power in temperature in (6.4) complicates the quest for an analytical solution to (6.1). Indeed, standard techniques, such as variable separation and integral transforms, cannot be applied. An alternative numerical solution to (6.1) for the simple configuration shown in Figure 6.1 is therefore developed here, against which the numerical scheme of Chapter 4 may be compared.

Explicit Finite Difference Solution

If T_τ^n is an approximation to the temperature field, $T(\xi^n, \tau)$, for some position ξ^n, $0 \leq n \leq N$, where $N-1$ is the number grid points spanning $[0, L]$, then, applying the standard explicit finite difference formulae [80] for all points $\xi^n = n\Delta\xi$, with $\Delta\xi \equiv 1/N$ and $1 \leq n \leq N-1$, gives

$$\begin{aligned} \left.\frac{\partial^2 T}{\partial \xi^2}\right|_{\xi^n,\tau} &= \frac{T_\tau^{n-1} - 2T_\tau^n - T_\tau^{n-1}}{(\Delta\xi)^2} + O[(\Delta\xi)^2] \\ \left.\frac{\partial T}{\partial \tau}\right|_{\xi^n,\tau} &= \frac{T_{\tau+\Delta\tau}^n - T_\tau^n}{\Delta\tau} + O[\Delta\tau] \end{aligned} \tag{6.5}$$

Obviously, (6.5) cannot be applied at the point ξ^N, since it would depend on a quantity T_τ^{N+1} which does not exist. So the point ξ^N is considered specially. A backward Taylor expansion about the point ξ^N is

$$\begin{aligned} T(\xi^{N-1}, \tau) &= T(\xi^n - \Delta\xi, \tau) \\ &= T(\xi^n, \tau) - \Delta\xi \left.\frac{\partial T}{\partial \xi}\right|_{\xi^n,\tau} + \frac{(\Delta\xi)^2}{2} \left.\frac{\partial^2 T}{\partial \xi^2}\right|_{\xi^N,\tau} - O[(\Delta\xi)^3] \end{aligned} \tag{6.6}$$

But (6.4) prescribes $\partial T/\partial\xi|_{\xi^n,\tau}$, so that

$$\left.\frac{\partial^2 T}{\partial \xi^2}\right|_{\xi^N,\tau} = \frac{2}{(\Delta\xi)^2}\left[T(\xi^{N-1}, \tau) - T(\xi^N, \tau) - \frac{\Delta\xi\, L\sigma\epsilon_{\text{eff}}}{k}\left(T^4(\xi^N, \tau) - T_a^4\right)\right] + O[\Delta\xi] \tag{6.7}$$

Applying the approximation $T(\xi^N, \tau) \approx T_\tau^N$ gives

$$\left.\frac{\partial^2 T}{\partial \xi^2}\right|_{\xi^N,\tau} \approx \frac{2}{(\Delta\xi)^2}\left[T_\tau^{N-1} - T_\tau^N - \frac{\Delta\xi\, L\sigma\epsilon_{\text{eff}}}{k}\left((T_\tau^N)^4 - T_a^4\right)\right] \tag{6.8}$$

Thus, applying the diffusion equation at the grid points $n = 0, \ldots, N$ to the approximations (6.5) and (6.8) results in Algorithm 7.

Algorithm 7 Finite difference calculation for the configuration shown in Figure 6.1

for $n = 0$ **do**

$T_{\tau-\Delta\tau}^0 = T_0$

$\Lambda \equiv \Delta\tau/(\Delta\xi)^2$

for $n = 1, \ldots, N-1$ **do**

$T_{\tau-\Delta\tau}^n = \Lambda T_\tau^{n-1} + (1 - 2\Lambda)T_\tau^n + \Lambda T_\tau^{n-1}$

for $n = N$ **do**

$T_{\tau-\Delta\tau}^N = 2\Lambda T_\tau^{N-1} - (1 - 2\Lambda)T_\tau^N - \dfrac{2\Lambda\,\Delta\xi\, L\sigma\epsilon_{\text{eff}}}{k}\left[1 - (T_a/T_\tau^N)^4\right](T_\tau^N)^4$

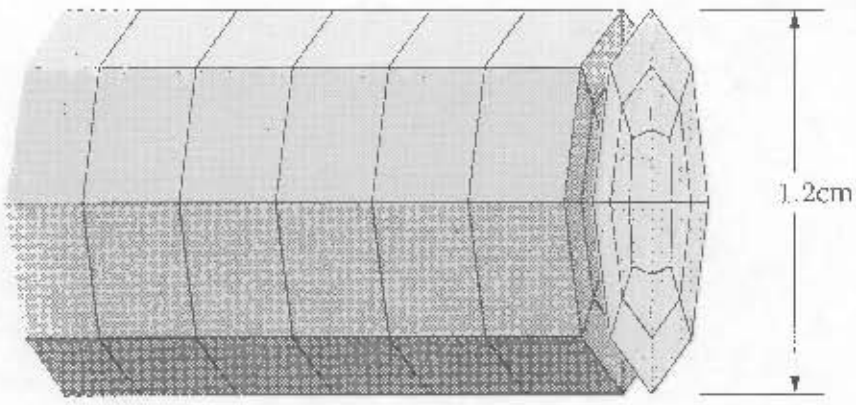

Figure 6.2: Finite element mesh of simple longitudinally conducting rod, insulated radially and radiating at one end. The apparent axial separation between the plate and the bar is fictitious—included merely to indicate the presence of the plate.

Table 6.1: Thermophysical properties for simple conducting/radiating rod

Conductivity (k) (W/cm/K)	Specific heat (C_p) (J/g/K)	Density (ρ_m) (g/cm^3)	Rod Emissivity (ϵ_L)	Plate Emissivity (ϵ_a)
0.2	0.5	8.0	0.5	1.0

Carnahan *et al* [80] show that discretisation error is minimised (to $O[(\Delta\xi)^4]$) whenever the normalised timestep is constrained to satisfy

$$\Delta\tau = \frac{1}{6}(\Delta\xi)^2 \tag{6.9}$$

Finite Element Solution

A finite element model was set up in which the radiation boundary condition at $x = L$ was accounted for using the net-radiation scheme described in §4.3. As shown in Figure 6.2, a total of 20 radiating facets were used to represent the radiating plate located at $x = L$. The length of the rod was divided into 50 elements.

Properties

Thermophyisical properties and configuration parameters for the conducting and radiating system shown in Figure 6.1 are listed in Tables 6.1 and 6.2.

Results

Temperature profiles across the length of the rod at four specific time instants are shown in Figure 6.3. The profiles were computed numerically using Algorithm 7 with 51 grid points

Table 6.2: Configuration paramaters for simple conducting/radiating rod

Length of rod, L	10cm
Diameter of rod	1.2cm
Fixed temperature of radiating plate, T_a	273K
Fixed temperature at $x = 0$cm, T_0	1773K
Initial rod temperature, T_i	1773K

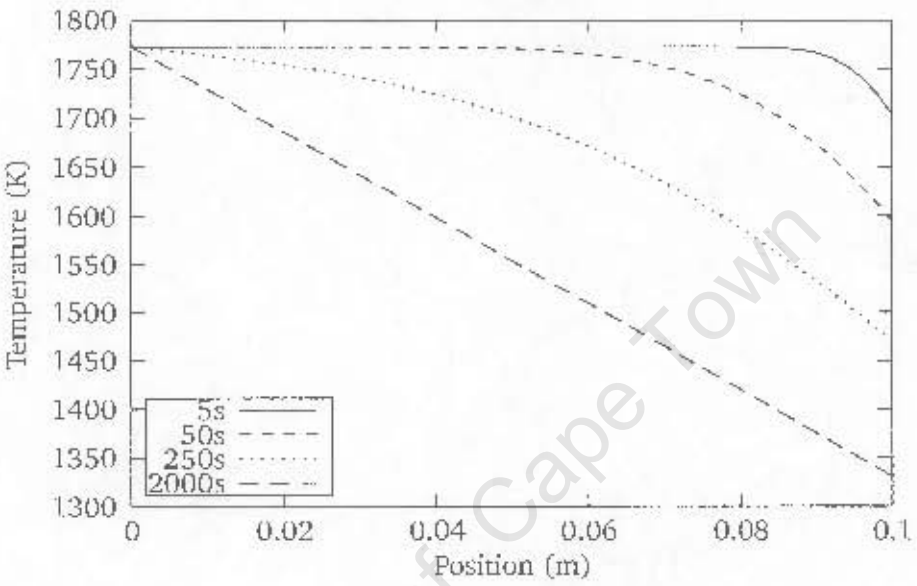

Figure 6.3: Temperature profiles across simple conducting rod at four time instants, showing progression to expected steady state linear profile (51 grid points)

(i.e. $N = 50$).

Temperature histories at five equidistant points along the length of the rod are shown in Figure 6.4. As with the profiles, the histories were computed using Algorithm 7 with 51 grid points.

Both the computed profiles and the histories exhibit the correct qualitative behaviour. But are they sufficiently accurate that they can be used to verify the finite element solution? Unfortunately, an analytical solution for the temperature evolution in the rod was not obtained in order to answer this question unequivocally. (In fact, an analytical solution would have obviated the need for the finite difference calculations entirely)

However, a steady state analytical analysis is straightforward. From (6.1) the steady state temperature field, T_{ss}, is governed by $\partial^2 T_{ss}/\partial x^2 = 0$. The solution is simply

$$T_{ss}(x) = \left(1 + \alpha \frac{x}{L}\right) T_0 \quad \text{for } 0 \leq x \leq L \tag{6.10}$$

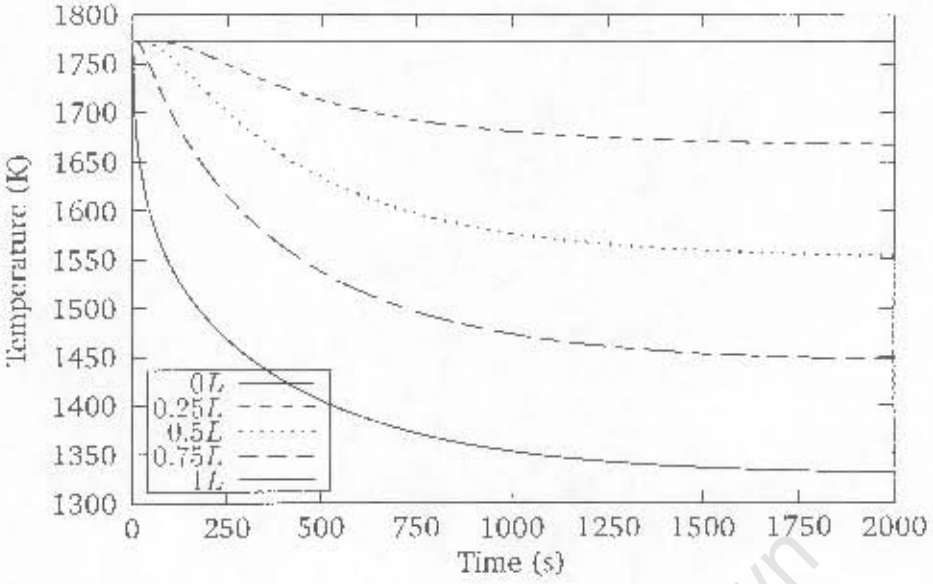

Figure 6.4: Temperature histories at five equidistant points along length of simple conducting rod. (51 grid points)

and where, from (6.4), α is the larger root of the fourth-order polynomial

$$(\alpha+1)^4 - \left(\frac{k}{L\sigma\varepsilon_{\text{eff}}T_0^3}\right)\alpha + \left(\frac{T_a}{T_0}\right)^4 \quad 0 \tag{6.11}$$

The larger root is $\alpha = 0.2509$, so that the exact steady state temperature at $x = L$ is predicted to be 1329K.

On the other hand, Algorithm 7 with $N = 50$ predicted a steady state temperature at $x = L$ of 1330K. The closeness of this solution to the exact solution provides some degree of confidence in the results which were computed using Algorithm 7 with $N = 50$.

This confidence is boosted further by studying the variation of discretisation error as a function of the number of finite difference grid points. The discretisation error at a point $x = \frac{3}{4}L$ and a time 250s is plotted in Figure 6.5, clearly indicating that such an error becomes of secondary importance as $N \quad > 50$.

Finally, the evolution of the relative difference between the finite element and the finite difference calculations at a point $x = \frac{3}{4}L$ is plotted in Figure 6.6, indicating that the relative difference in the solutions stabilises at about 1.2%. This result serves to validate (at least for this relatively simple conducting/radiating configuration) the coupled finite element/net-radiation numerical scheme described in Chapter 4.

6.2 Simple Equiaxed Investment Casting

A mesh of a hypothetical equiaxed casting of a rectangular bar was generated as shown in Figure 6.7 (shaded region). The objective of this model was to study the efficacy of both the

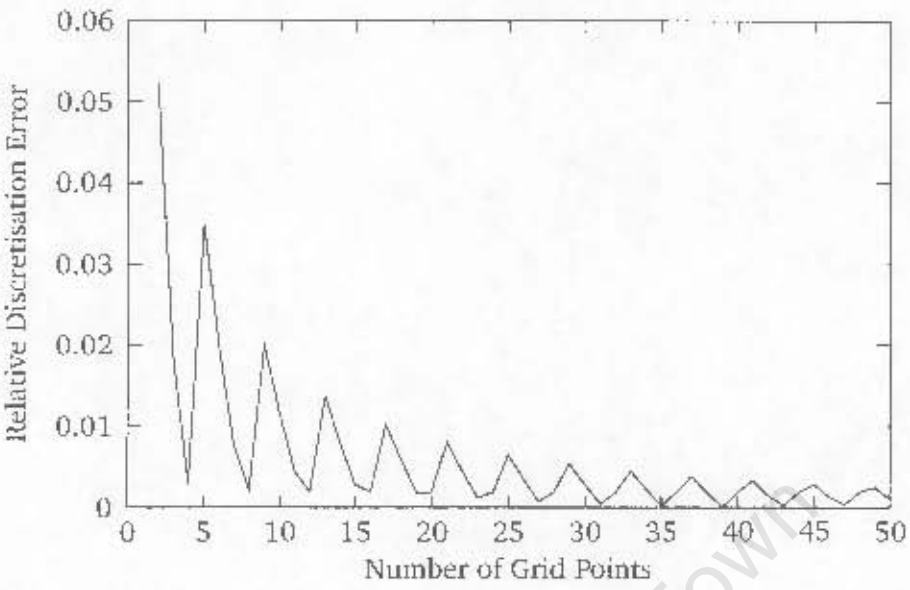

Figure 6.5: Grid refinement study for simple conducting rod. A relative spatial discretisation error is plotted at ($x = \frac{3}{4}L, t$ 250s) as function of number of grid points (N), relative to solution for $N = 51$

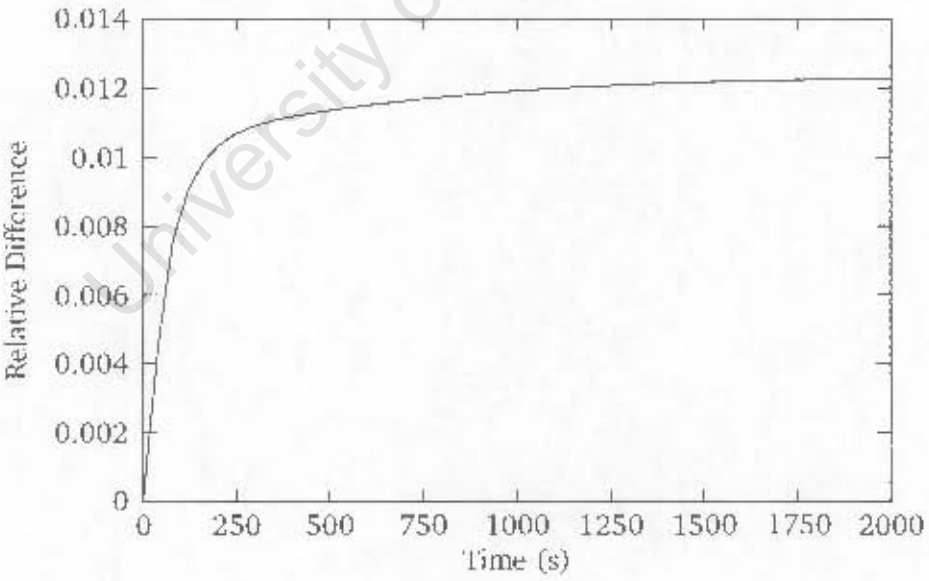

Figure 6.6: Comparison of finite element solution with finite difference solution. Relative difference between finite element solution and explicit finite difference solution is plotted at $x = \frac{3}{4}L$. Relative difference is 1.2% at steady state (51 finite difference grid points, 50 finite elements along rod length)

Table 6.3: Thermophysical properties for the metal

Conductivity (W/cm/°C)	Specific heat (J/g/°C)	Density (g/cm^3)
0.2	0.5	8.0

Table 6.4: Thermophysical properties for the mould

Conductivity (W/cm/°C)	Specific heat (J/g/°C)	Density (g/cm^3)	Emissivity
0.03	1.3	3.0	0.5

cavity radiation model developed in §4.3 as well as its coupling to the finite element model (§4.4). Thermophysical data for the metal and the mould are listed in Tables 6.3 and 6.4. Simulation parameters are listed in Table 6.5.

Three simulations were performed subject to different radiation boundary conditions. In the first simulation a single bar was assumed to lose energy to a blackbody environment via the simple Stefan formula (3.28). In the second simulation the numerical model developed in Chapter 4 was invoked. Computed temperature histories at the point marked with a 'Y' in Figure 6.7 are shown in Figure 6.8. The point 'Y' is located on the mould surface of the first bar.

These histories verify, for a single bar, the close correspondence of the numerical result with the analytical result for this simple geometry. The time increment interval was set at $2\frac{1}{2}$s, and the average number of Newton iterations per increment for the finite element computation was 3. However, when the coupling algorithm described in §4.4 was not applied, so that the net heat flux values at the integration points were assumed to equal the average value over the elemental face, the average number of iterations was 7.

In the third simulation a symmetric slave geometry (unshaded region, Figure 6.7) was generated using the *SYMMETRY option (source line 50, page 82). The temperature history at the point 'Y' (which now is directly exposed to the symmetric geometry) confirms the retardation of the simulated cooling of the first bar due to the radiant interaction between the two bars.

6.3 Single Axisymmetric Directional Castings

The objective in the following two models was to address the complexities that arise in modelling actual directional casting processes, where such complexities do not stem from the radiant interactions. Castings were therefore selected in which the radiant interactions are relatively simple.

Table 6.5: Casting parameters for hypothetical simple equiaxed casting

Initial metal temperature	1000 °C
Initial mould temperature	1000 °C
Ambient temperature	20 °C
Height of bar	10cm

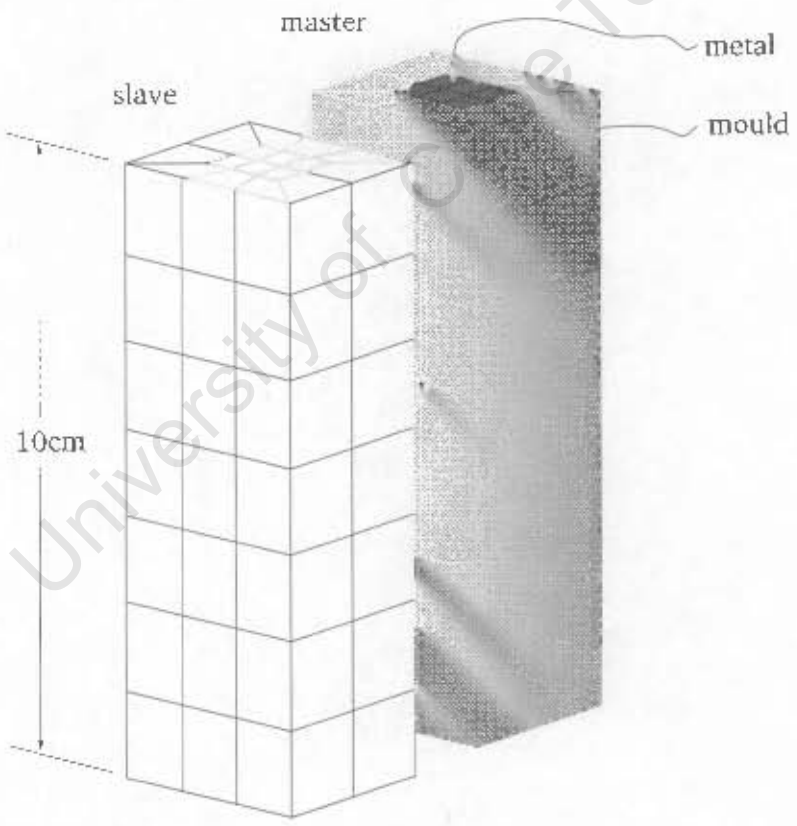

Figure 6.7: Finite element mesh of equiaxed casting of rectangular bar (shaded) and facet mesh of symmetric slave bar (unshaded). The point at which temperature histories are recorded is marked with a 'Y'

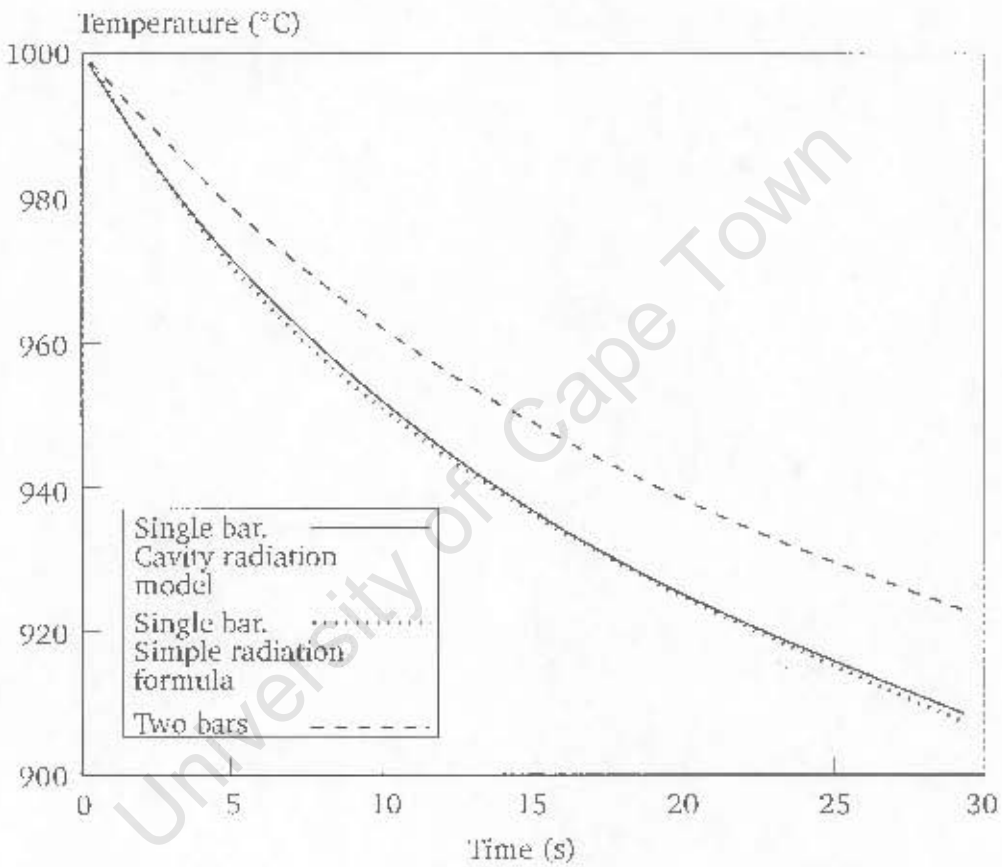

Figure 6.8: Temperature histories at nodal point 'Y' in Figure 6.7

6.3.1 Cylindrical Bar

An actual directional casting rig and a resulting solidified cylindrical bar is shown in Figures 6.9 and 6.10. Type 'R' (Pt/Pt-Rh) thermocouples were used to obtain readings at selected intervals along the length of the bar.

Model Description

An idealised geometry, a finite element mesh, boundary conditions, and a few dimensions are all shown in Figure 6.11.

A simplified model of the radiant interactions suitable only for castings having simple axisymmetric geometries was applied. In this model the net heat flux at all points on the surface of the mould was assumed to have the form

$$q_R(T, \mathbf{x}, t) \quad \sum_{n}^{3} F_{mn}(x, z, t) \frac{\sigma}{1/\epsilon_n + 1/\epsilon(x, z, t) - 1} \left(T(x, z, t)^4 \quad [T^m]^4\right) \tag{6.12}$$

with the coordinates defined in Figure 6.11, and where F_{m1}, F_{m2} and F_{m3} are, respectively, the view factors from any point on the mould surface to the furnace heaters above the baffle, the furnace walls below the baffle, and the horizontal mould surface above the chill plate. The emissivities of the three regions are respectively ϵ_1, ϵ_2 and ϵ_3.

This formula is an approximation in the sense that it accounts for the multiple reflections between a facet on the mould surface and each of the abovementioned zones, but it neglects any interaction between the zones themselves.

The simple radiation system must account for discrete changes in the values of the view factors, F_{mn}, as the baffle moves upward past the chill plate.[2] With the nomenclature in Figure 6.11 this was achieved using Algorithm 8. The resulting variation of the view factors as a function of position along the length of the bar is plotted in Figure 6.12.

Material Properties and Casting Parameters

The cast metal is MAR-M200 — a nickel–base superalloy that was commonly used in the manufacture of gas turbine rotors in the early 70s [4, p 7] (see also Figure 2.1). Its composition by percentage weight is: 58.28 Ni, 0.15 C, 9.0 Cr, 10 Co, 5.0 Al, 2.0 Ti, 12.5 W, 1.0 Nb, 0.05 Zr, 0.02 B, and 2.0 Hf [28]. Hafnium, in particular, was introduced as a grain–boundary strengthener. Its temperature capability is 1040 °C.[3] Thermophysical data for the metal are listed in Table 6.6.

[2] In the numerical model discussed in §4.3.6 such discrete changes in the view factor values are accounted for implicitly.

[3] 100 hours to rupture at 140 MPa

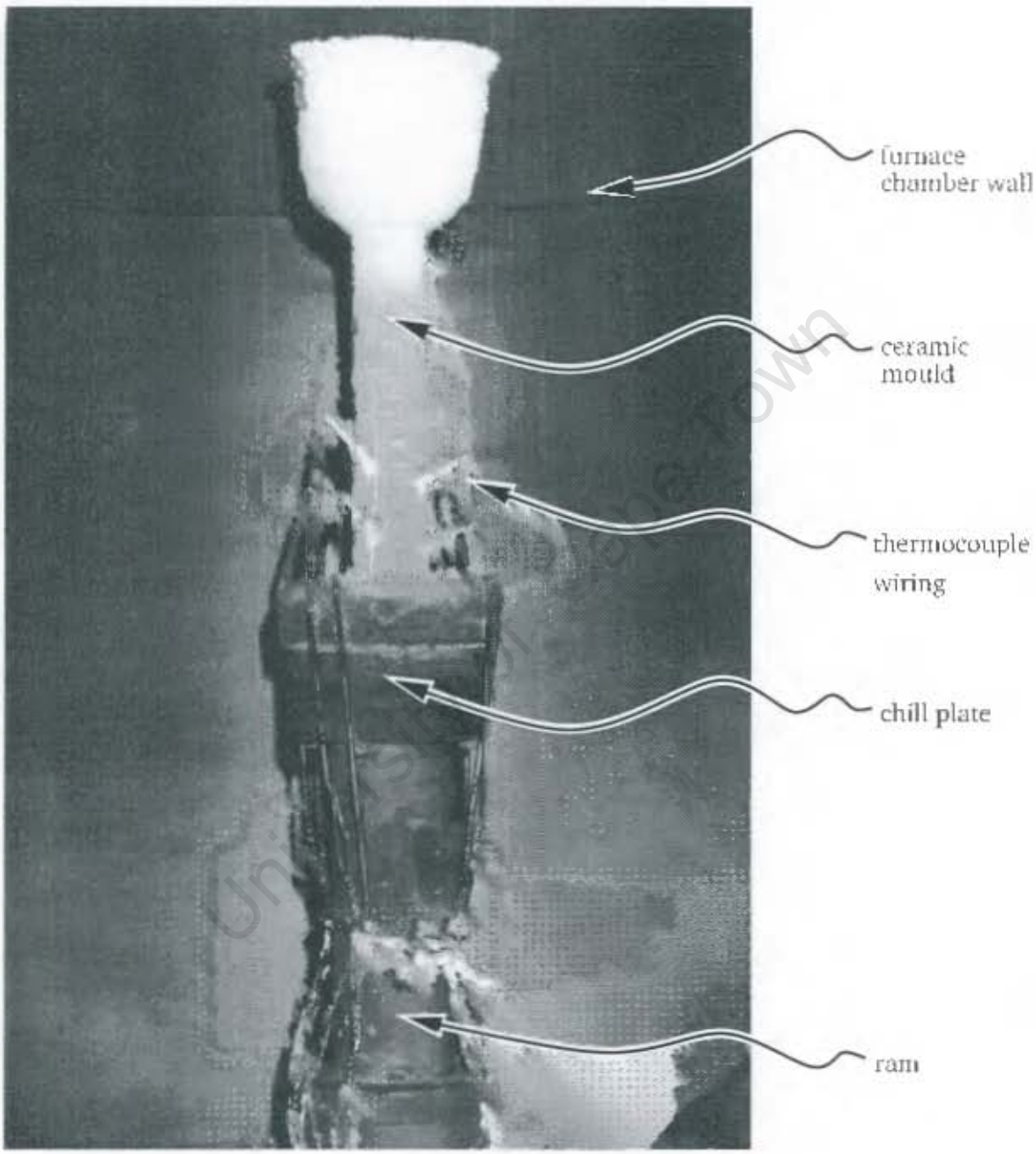

Figure 6.9: Photograph of instrumented DS bar casting rig

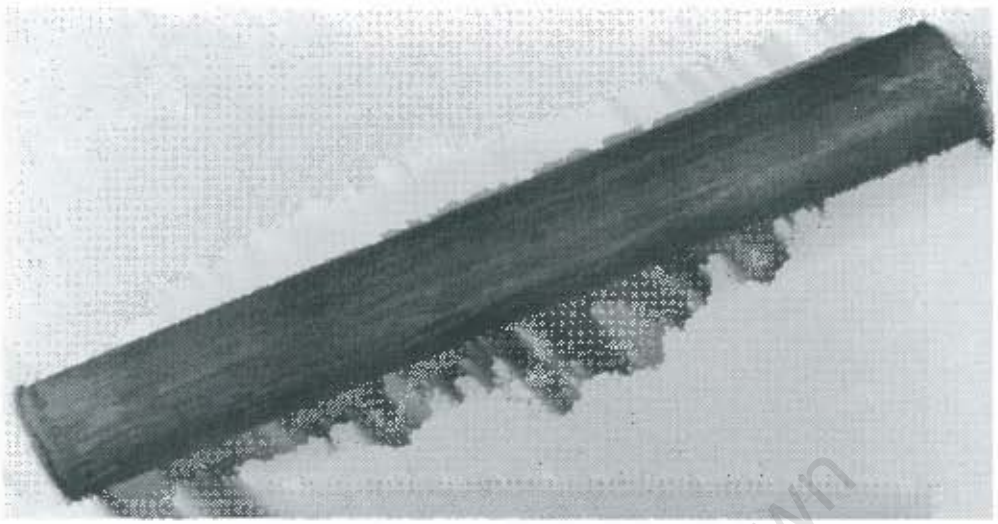

Figure 6.10: Photograph of DS cast bar

Algorithm 8 View factors for the directional casting of objects having simple axisymmetric geometries

if $z \geq z_c$ **then**

$$S_b(x,z,t) \equiv \sin(\theta_b(x,z,t)) = \frac{z - b(t)}{\sqrt{(z-b(t))^2 + (x-x_b)^2}}$$

$$S_c(x,z,t) \equiv \sin(\theta_c(x,z,t)) = \frac{z - z_c}{\sqrt{(z-z_c)^2 + (x-x_c)^2}}$$

$F_{m3} = \frac{1}{2}(1 - S_c)$

if $\theta_b \leq \theta_c$ **then**

$F_{m1} = \frac{1}{2}(1 + S_b)$

$F_{m2} = \frac{1}{2}(S_c - S_b)$

else

$F_{m1} = \frac{1}{2}(1 + S_c)$

$F_{m2} = 0$

else

$F_{m1} = \frac{1}{2}(1 + S_b)$

$F_{m2} = \frac{1}{2}(1 - S_b)$

$F_{m3} = 0$

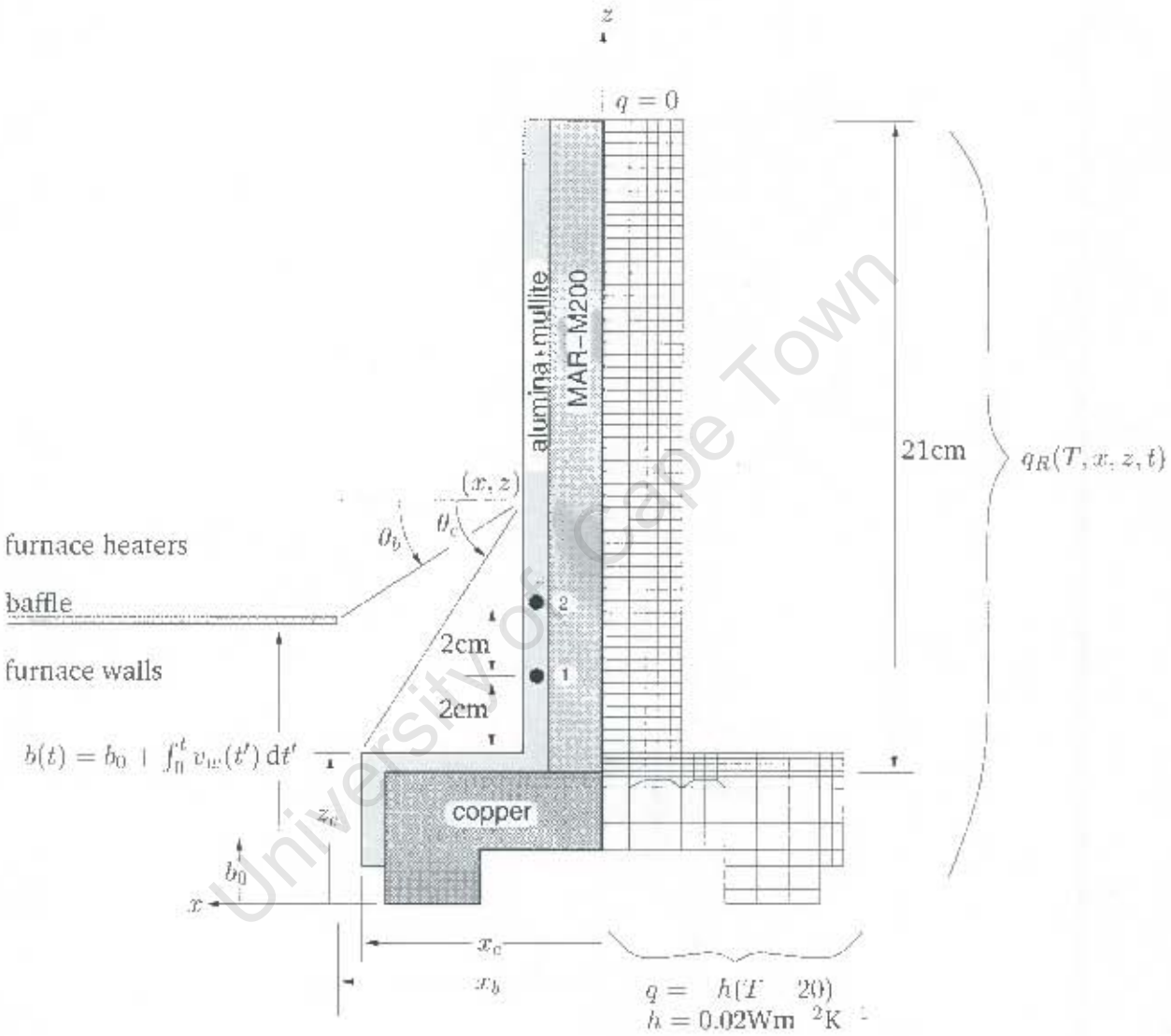

Figure 6.11: Idealised geometry and finite element mesh of directional casting of axisymmetric bar. Thermocouple locations indicated with a '•'

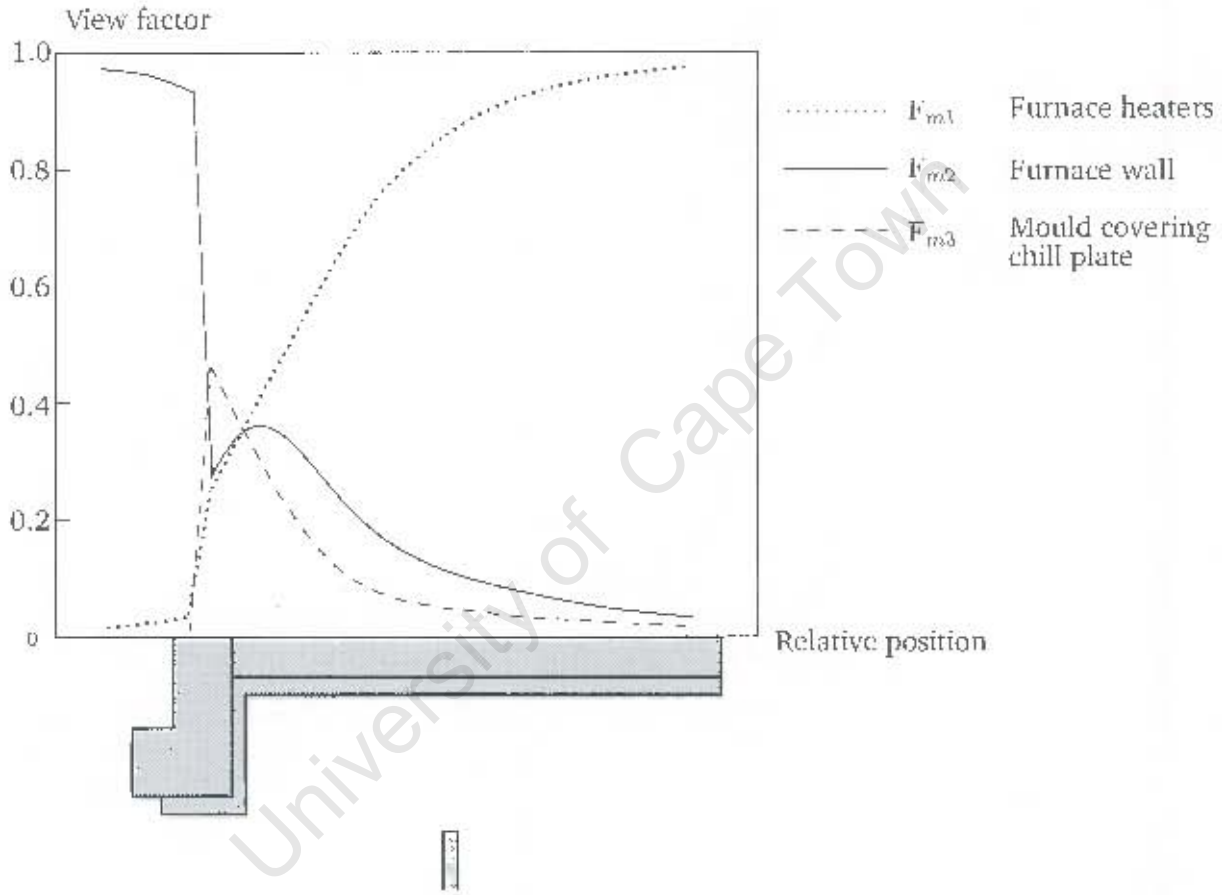

Figure 6.12: View factors for points on mould surface of directional casting of an axisymmetric bar. Baffle assumed to have moved 10cm along length of bar

Table 6.6: Thermophysical properties for MAR-M200 [93, pp 248,271]

Temperature (°C)	Conductivity (W/cm/°C)	Specific heat (J/g/°C)	Density (g/cm^3)	Latent heat (J/g)	Solidus (°C)	Liquidus (°C)
21	0.127	0.4	8.53	200	1295	1375
93	0.130	0.4				
205	0.135	0.395				
315	0.138	0.42				
425	0.151	0.44				
540	0.152	0.42				
650	0.173	0.46				
760	0.140	0.48				
870	0.216	0.5				
980	0.249	0.525				
1090	0.297	0.565				
1200		0.580	8.53			
1227	0.308		8.10			
1290		0.580				
1327	0.326					
1375		0.610				
1392	0.338					
1500	0.335	0.650	8.10			

Thermophysical data for the ceramic mould material and the copper chill plate are listed in Tables 6.7 and 6.8. The values for the conductivity and density of the mould have been reduced by 15% to account for the presence of porosity in the mould.

The emissivity values of the mould surface and the furnace heaters and walls are recorded in Figure 6.13; and by virtue of the diffuse–grey approximation (§3.3.4), the values for the reflectivities are immediately available using (3.44).

Table 6.7: Thermophysical properties for 75% Aluminium dioxide (Al_2O_3) + 25% Mullite ($3Al_2O_3.2SiO_2$) [94, p 31]

Temperature (°C)	Conductivity (W/cm/°C)	Specific heat (J/g/°C)	Density (g/cm^3)
0		1.101	2.975
20		1.120	
100		1.165	
200		1.203	
232	0.0756		
300		1.254	
317	0.0669		
322	0.0711		
400	0.0626	298	
500		1.351	
535	0.0558		
600		1.419	
601		1.343	
650	0.0487		
700		1.312	
800		1.260	
827		1.332	
907	0.0417		
927		1.351	
1015	0.0402		
1027		1.368	
1127		1.384	
1200	0.0399		
1300	0.0383		
1327		1.416	
1527		1.446	
1600	0.0402		

Table 6.8: Thermophysical properties for Copper [93, p 395]

Conductivity (W/cm/°C)	Specific heat (J/g/°C)	Density (g/cm^3)
3.46	0.38	8.94

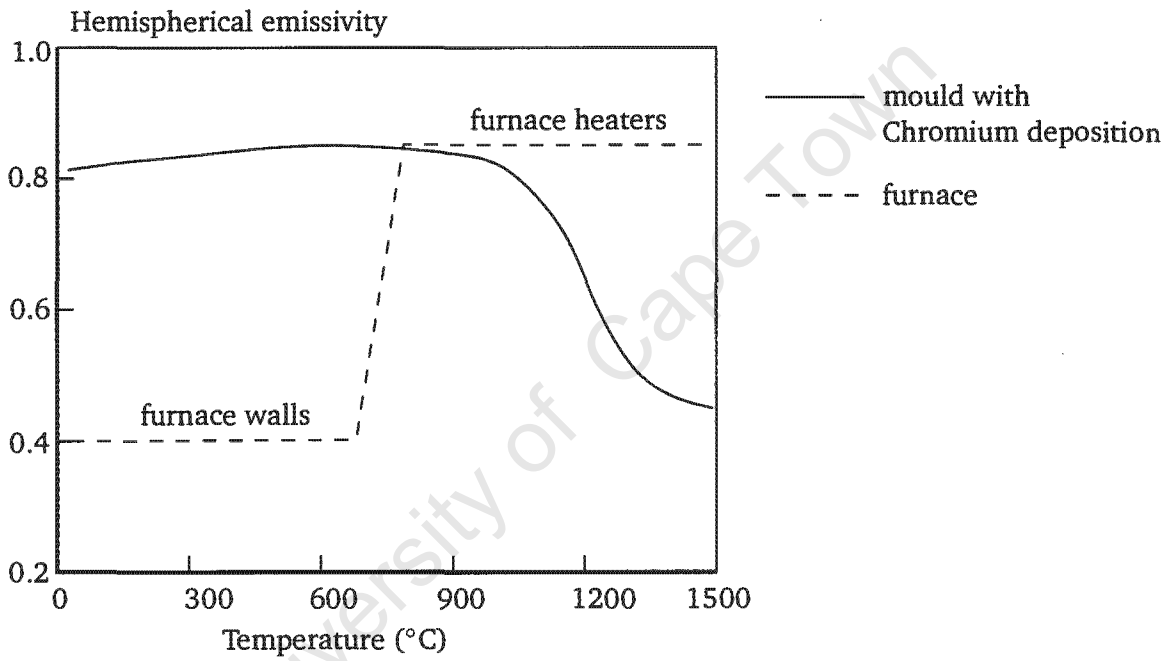

Figure 6.13: Emissivity of mould surface, furnace heaters and furnace walls [94]. The variation of mould emissivity accounts for deposition of chromium on mould surface

Table 6.9: Casting parameters for cylindrical bar

Initial metal temperature	1480 °C	
Initial mould temperature	1480 °C	
Initial chill plate temperature	20 °C	
Furnace heater temperature	1480 °C	
Furnace wall temperature	20 °C	
Initial vertical baffle position	1.8cm	
	Δt (min)	v_w (mm/min)
Casting withdrawal sequence	5	0
	∞	4

The remaining casting parameters are listed in Table 6.9. The simulation begins just after the molten metal is poured into the mould. An initial 'resting' period was simulated by specifying a zero withdrawal rate for the first 5 minutes, as listed.

Results

Computed and measured temperature histories at the thermocouple locations labelled in Figure 6.11 are shown in Figure 6.14. A comparison between the computed and measured results suggests that the numerical model simulates too great a heat loss from the casting during the early stages of withdrawal. Therefore, to assume that the metal and mould material make direct contact with the copper chill plate is incorrect. As the molten metal is poured into the mould cavity it strikes the water–cooled chill plate, solidifying very rapidly in an axial zone located just above the chill plate. As it solidifies this zone shrinks, retracting marginally from the chill plate, thereby forming a thermal gap. This gap then persists for the duration of the casting process, leaving radiation as the only mechanism for the transfer of heat energy between the cast metal and the chill plate.

A 'thermal gap' at the interface between the metal and the chill plate and between the mould and the chill plate was therefore introduced using the following expression for the radiant heat flux across the gaps:

$$q_g = \frac{\sigma}{1/\epsilon_{ga} + 1/\epsilon_{gb} - 1} \left(T_{gb}^4 - T_{ga}^4\right) \tag{6.13}$$

The subscripts 'a' and 'b' denote the surfaces on the a'th and b'th materials, respectively. Emissivity values of 0.6, 0.6, and 0.55 were used for the cast metal, the chill plate, and the mould material, respectively.

Temperature histories were again computed, as shown in Figure 6.15. The surprisingly good agreement between the computed and measured results at early simulation times testifies to the significance of the thermal gaps that may exist between materials.

But what then of the presence of a thermal gap between the metal and the mould after the metal solidifies? Numerical studies were conducted to investigate this, the results of which

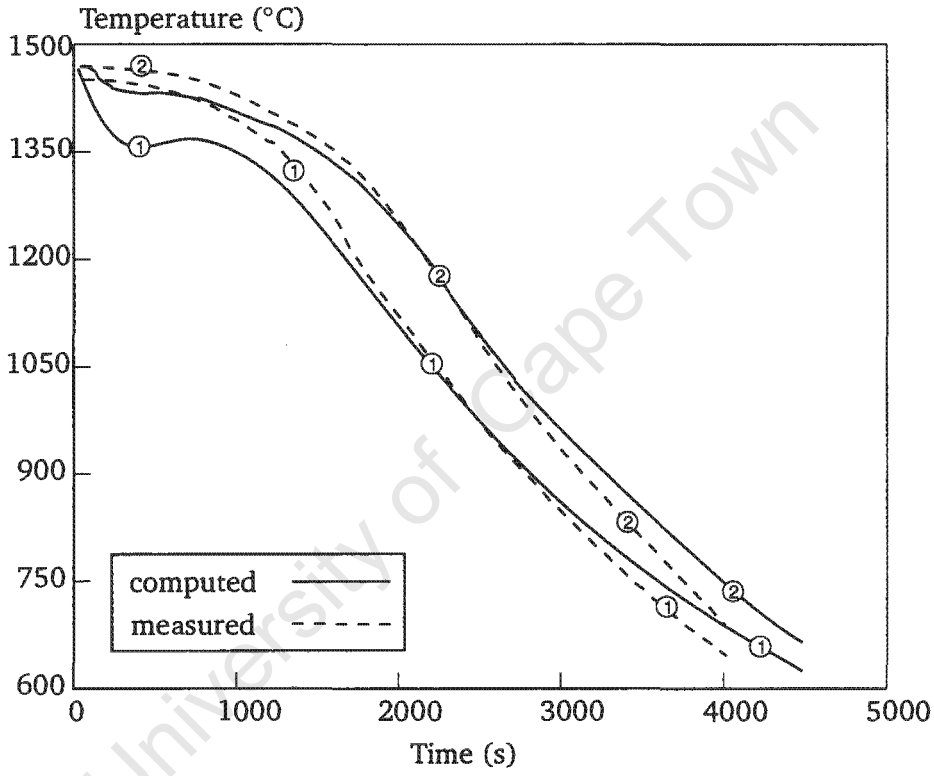

Figure 6.14: Temperature histories at thermocouple locations labelled in Figure 6.11. Existence of a 'thermal gap' between bar and chill plate *not* simulated

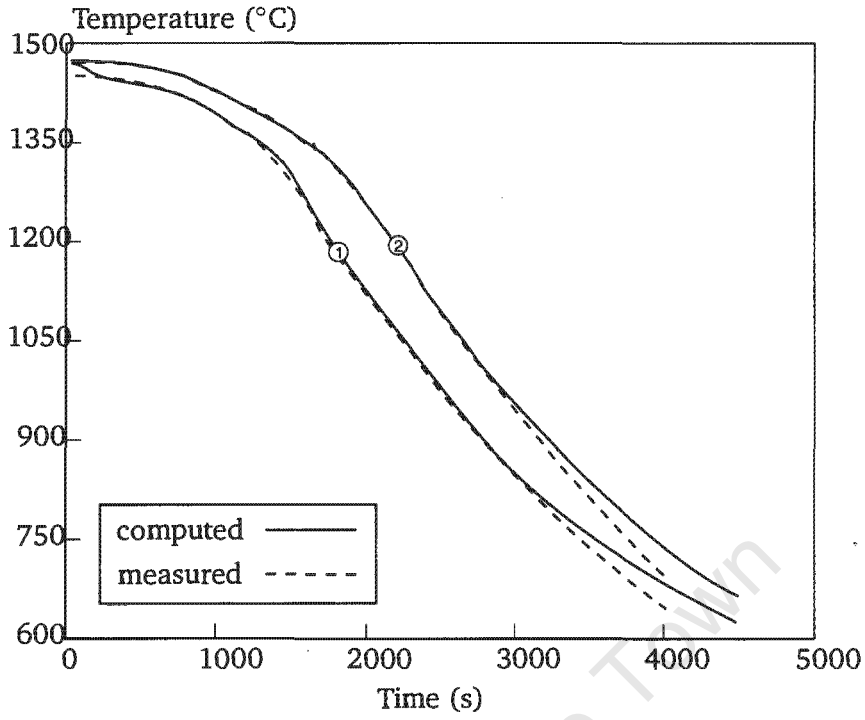

Figure 6.15: Temperature histories at thermocouple locations labelled in Figure 6.11. Existence of a 'thermal gap' between bar and chill plate modelled using Equation (6.13)

are shown in Figure 6.16. Comparison with Figure 6.15 indicate that the *absence* of such a metal–mould gap in the model produced the most accurate results. This suggests that, at least for early times after solidification, no such physical significant gap exists betweeen the metal and the mould.

However, the thermal expansion coefficients of the metal and the mould are non–identical. Therefore a thermal gap between the metal and the mould must indeed form at later times after more of the metal has solidified. The existence of this gap would impede the radial flow of heat energy from the metal to the mould, allowing the mould material to cool quicker.

To model the effect of this gap formation it must be known exactly when the gap forms and how pronounced it is. Addressing this requires the introduction of a mechanical component into the analysis. This is beyond the scope of this study. However, the deviation between the computed and measured temperature histories at later times (Figure 6.15) empirically supports the explanation of the previous paragraph. Recently Lewis and Ransing [95] studied the formation of such gaps in detail. They derived an empirical equation to describe the interfacial heat transfer coefficients. An interesting possibility for future study would be to apply the results of their work to the types of simulations described here.

Finally, as part of a parametric study, a simulation was carried out in which the effect of multiple reflections between a facet on the mould surface and the three radiating zones (Equation (6.12)) was neglected. In the simulation, the 'effective' emissivity in (6.12) was replaced

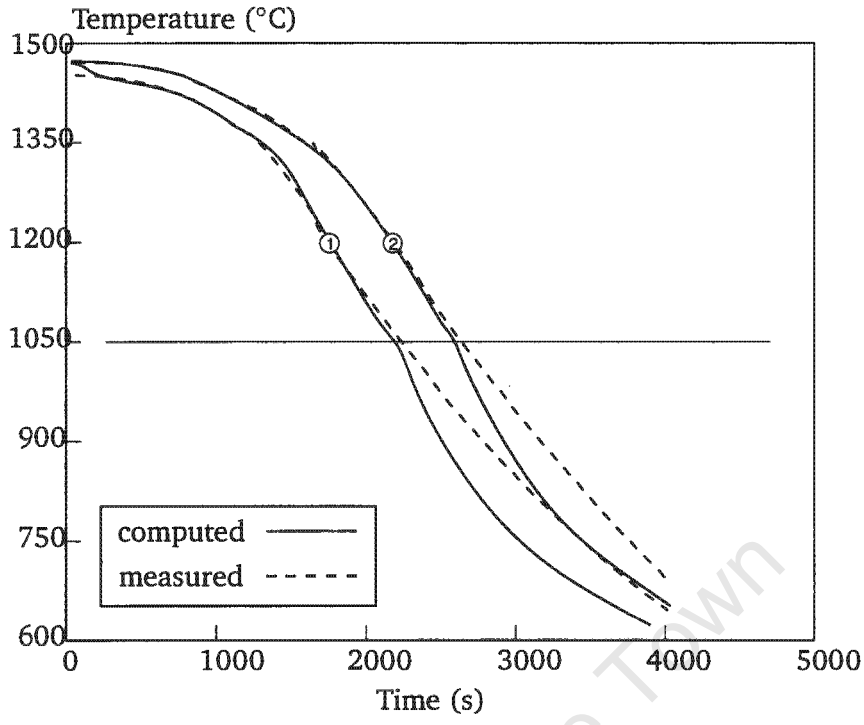

Figure 6.16: Temperature histories at thermocouple locations labelled in Figure 6.11. Existence of a 'thermal gap' between bar and chill plate modelled using Equation (6.13). Metal/mould gap forms at 1050 °C

simply with the hemispherical emissivity of the mould surface, varying as per Figure 6.13. Two resultant temperature histories are shown in Figure 6.17. A comparison of the histories in Figure 6.17 with those in Figure 6.15 highlights the importance of addressing cavity radiation effects in such casting models, even when the geometries are relatively simple.

6.3.2 Tensile Test Specimen

The standard tensile test specimen is an ideal candidate with which to study the influence of solidification behaviour on the resultant microstructure. The geometry of a specimen is axisymmetric and simple, so that the simplified radiation model (6.12) developed for the cylindrical bar can be applied. The geometry does however contain sufficient variability in order that its influence on the microstructure (see page 9) can be studied. Such a study will be carried out in this section by considering a numerical model of the process.

Model Description

An idealised geometry and mesh are shown in Figure 6.18.

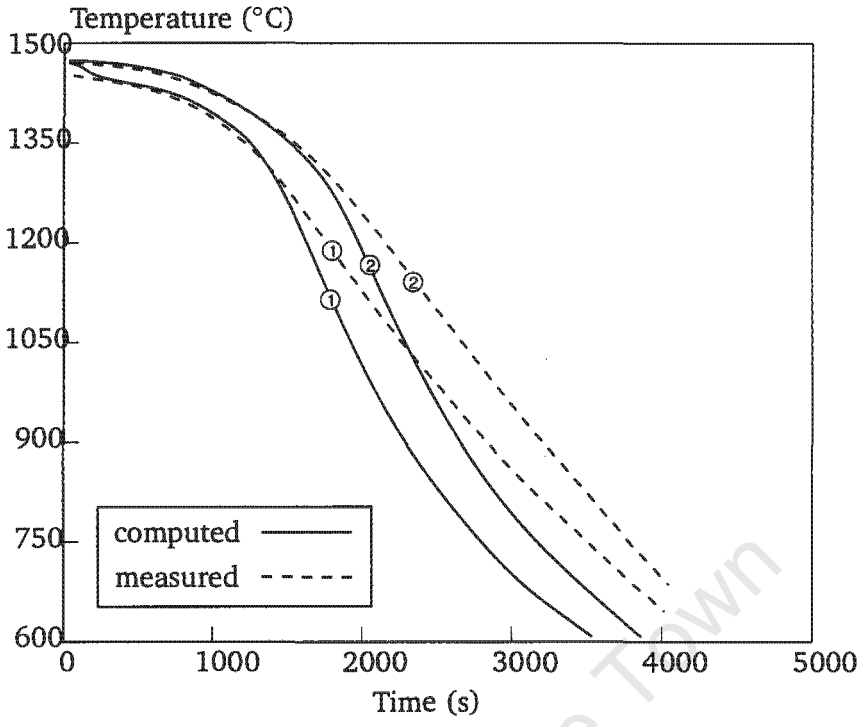

Figure 6.17: Temperature histories at thermocouple locations labelled in Figure 6.11. Existence of a 'thermal gap' between bar and chill plate modelled using Equation (6.13). Multiple reflections *not* accounted for as per (6.12).

Material Properties and Casting Parameters

The cast metal is CMSX-6—a nickel–base superalloy that was developed specifically for the production of single–crystal castings. The development of the single–crystal casting process made it possible to eliminate grain–boundaries in the casting, and therefore to simplify alloy compositions by removing or reducing the volume fraction of grain–boundary strengthening elements [28]. The role of the helical single–crystal seeding device (commonly called the 'pig's tail') in the casting design (Figure 6.18) is to promote competitive growth between the grains so that a single grain is left as the mushy zone emerges out of the seeder.

The helical geometry of the pig's tail was not included in the finite element mesh. Because of its relatively long and narrow dimensions, the conduction of heat down the pig's tail to the chill plate is proportionally low, when compared with radiation transfer to the furnace walls.

Unfortunately, not all the thermophysical data for CMSX-6 were available. However, since the composition of CMSX-6 is similar to that of MAR-M200 the data tabulated in Table 6.6 were used instead, with the exception of the solidus and liquidus temperatures. The solidus and liquidus temperatures were taken to be 1288 °C and 1321 °C, respectively.

The casting parameters are those listed in Table 6.10

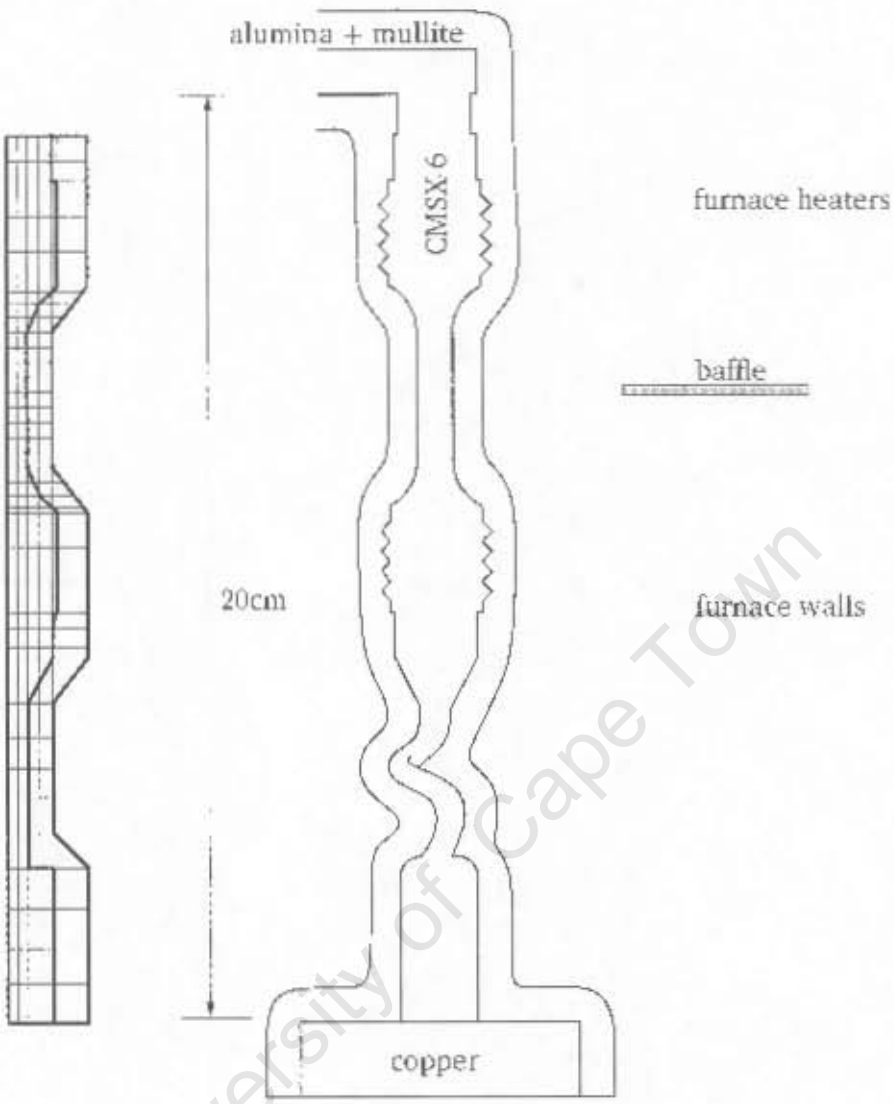

Figure 6.18: Finite element mesh and geometry of a single-crystal casting of a tensile test specimen

Table 6.10: Casting parameters for tensile test specimen

Initial metal temperature	1520 °C	
Initial mould temperature	1520 °C	
Initial chill plate temperature	20 °C	
Furnace heater temperature	1520 °C	
Furnace wall temperature	20 °C	
Initial vertical baffle position	1.8cm	
	Δt (min)	v_w (mm/min)
Casting withdrawal sequence	5	0
	7	4
	21	3
	∞	3.5

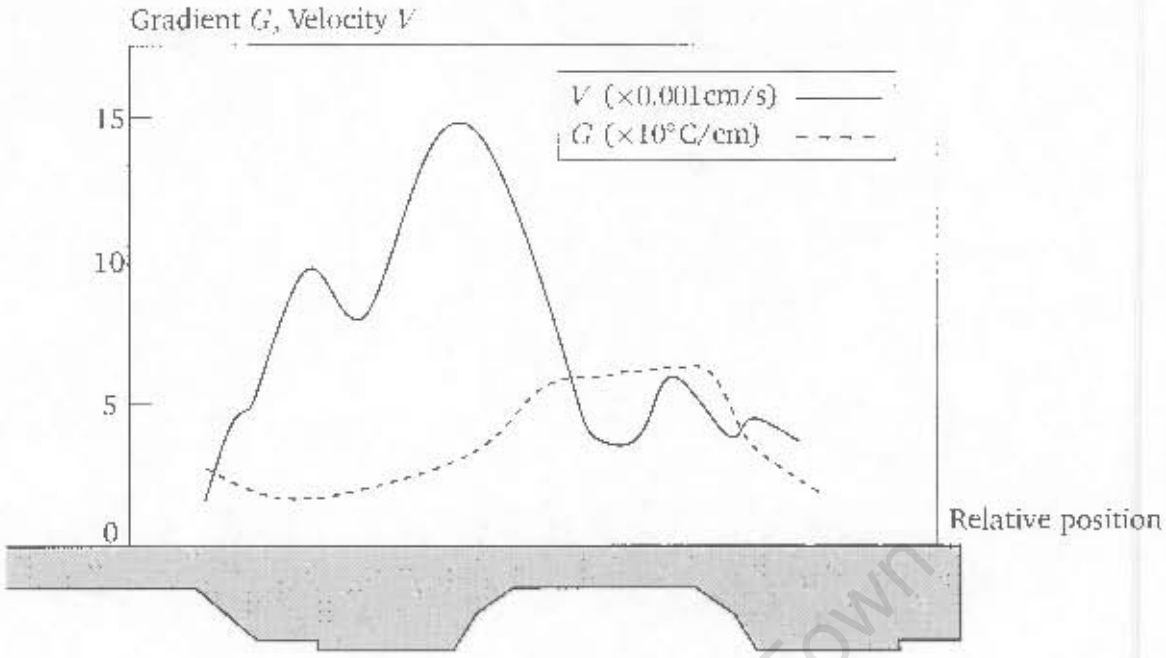

Figure 6.19: Computed variation of the average thermal gradient, G, across the mushy zone and solidus front velocity, V_S

Results

As discussed in §2.3, the nature of the cast microstructure is strongly influenced by the thermal gradient, G, across the mushy zone and the solidus front velocity, V_S. Computed variations of these quantities are plotted in Figure 6.19. It is interesting to note that although the withdrawal rate is held approximately constant at 4mm/min, the solidus front velocity varies markedly around the value of the withdrawal rate. Consequently, the microstructure is likely to vary markedly along the length of the specimen.

The primary dendrite arm spacing (PDAS) was measured. Several sections were cut from a cast specimen, polished and chemically etched, as shown in Figurefeff:samples. Values for the PDAS at all the sections were then measured using a digital image analyser. Typical dendrite structure is shown in the cross–sectional micrograph in Figure 6.21.

Recall from §2.3 (page 11) that the PDAS may be related to G and V_S in the following formula:

$$\text{PDAS} = A\,\frac{1}{(V_S G^2)^{1/4}} \qquad \text{for some constant } A \tag{6.14}$$

With $A \quad 258\mu\text{m}[^\circ\text{C}^2\,\text{cm}^{-1}\text{s}^{-1}]^{1/4}$, a variation of the PDAS along the length of the specimen was computed (Figure 6.22). The reasonable correlation between the computed and measured results is significant in that it demonstrates the use of numerical models to correlate the casting process with the resultant microstructure.

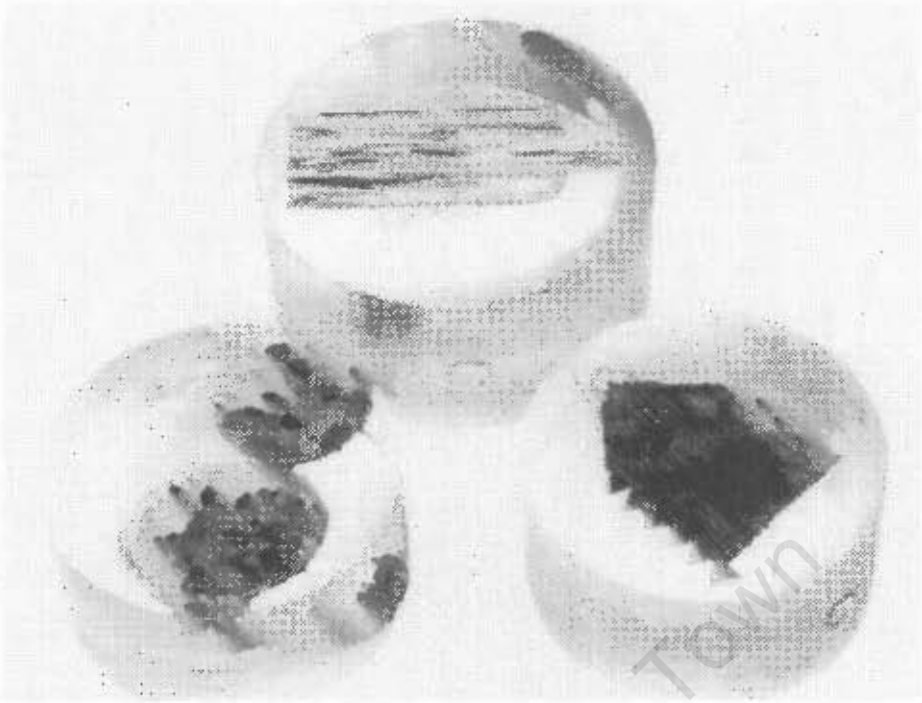

Figure 6.20: Mounted longitudinal and cross–sections samples from a tensile test specimen showing multiple grain–boundary formation below the pig's tail (*top, left*) and single crystal growth above (*right*)

6.4 Clustered Directional Casting

The geometries of the axisymmetric castings considered above were simple enough that radiant interactions between surface elements on the mould surface could largely be neglected. In this section it will be shown unequivocally that these interactions cannot be neglected if more complex non -axisymmetric geometries are to be considered.

The geometry of the mould shown in Figure 6.23 is one such geometry. The casting in this case is a cluster of six directionally solidified bars arranged cyclically around a central sprue.

Model Description

A finite element mesh of the casting, as shown in Figure 6.24, was created using the commercial software MSC/ARIES. The software has powerful automatic mesh generation capabilities, making it possible, for example, to specify the existence of the internal material boundaries between the metal, the mould and the chill plate.

Clearly, planes of cyclic symmetry are exploited in this model. By doing so the number of elements was reduced from 58100 to 9685.

A discretization of the radiating cavity was then defined using the facet mesh shown in Fig-

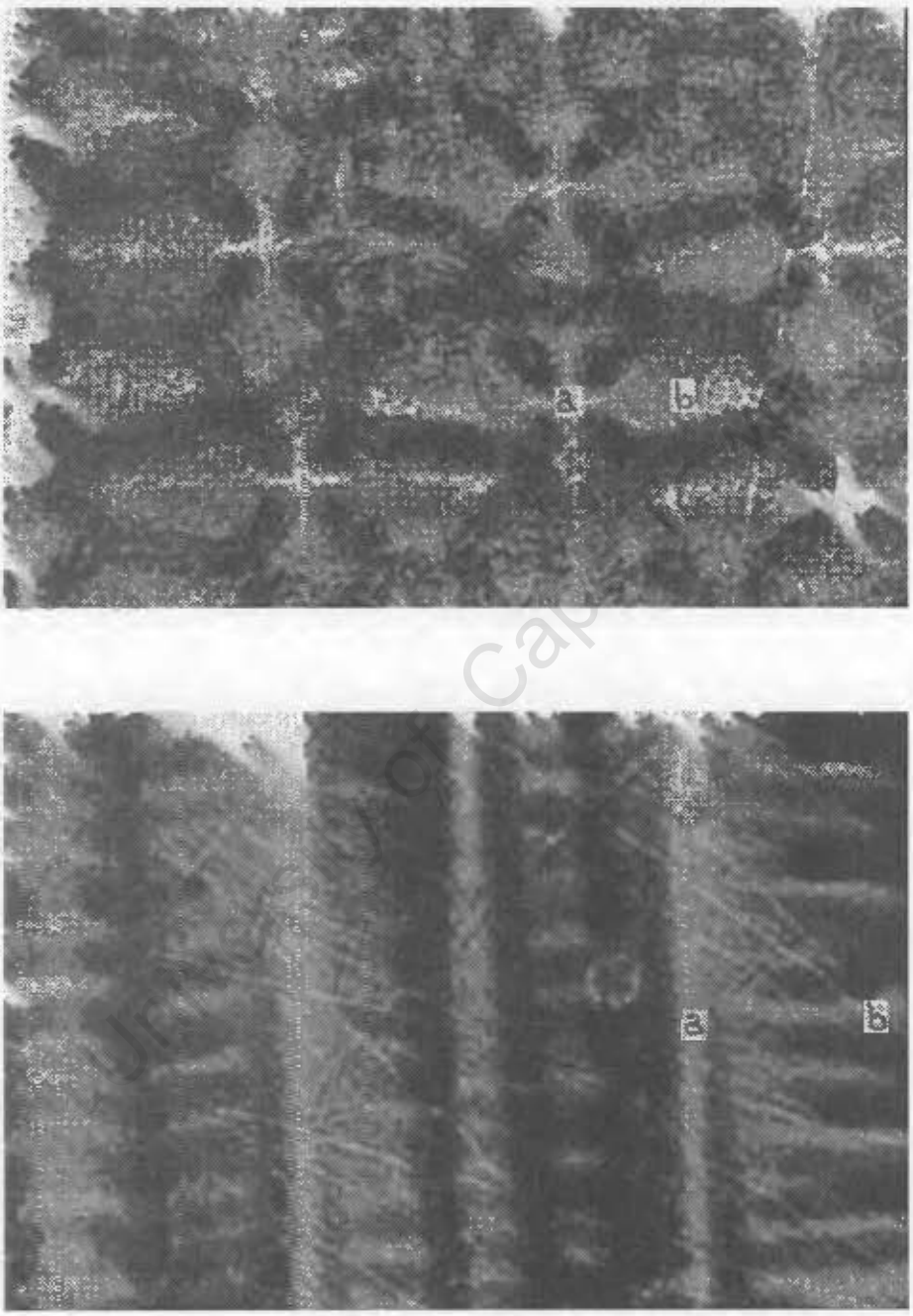

Figure 6.21: Sectional micrograph of typical dendrite structure. Primary dendrite at 'a' and secondary dendrite arm at 'b' (Magnification: 50×)

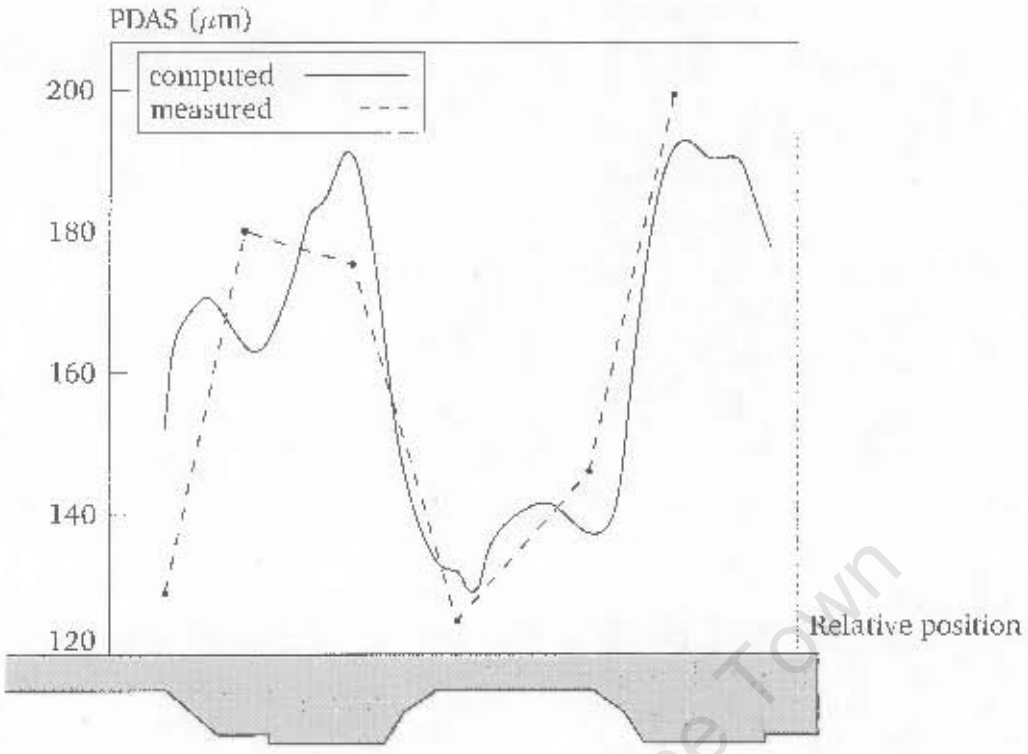

Figure 6.22: Computed (Equation (6.14)) and measured variation of primary dendrite arm spacing (PDAS) along length of tensile specimen

ture 6.25. The master facet set (as defined in §4.3.4) is comprised of the radiating exterior elemental faces of the mould surface of the finite element mesh (Figure 6.24) and a single column of facets representing a section of the furnace. The remaining symmetric parts of the casting are represented by a coarser facet mesh, as shown. The remaining parts of the furnace are represented by 19 additional columns of facets which are constrained to be symmetric to the first column. The facet mesh consists of 2222 master facets with 1605 slave facets for the casting, and 29 master facets with 551 slave facets for the furnace.

A comparative analysis of the cost savings accrued in applying the symmetry algorithms of §4.3.4 is summarised in Table 6.11. The analysis starts with the case in which symmetry conditions are *not* applied, and in which the entire geometry of the radiating cavity is represented with a fine mesh. The cost of computing the view factor database is reduced by a factor 3.25 if the cyclic symmetry conditions are then applied over this mesh. If on the other hand, part of the geometry is represented with a coarser facet mesh (Figure 6.25), then the cost is reduced by a factor 30. Finally, if part of the geometry is represented with a coarser facet mesh, and if symmetry conditions are then applied to this coarser mesh, then the original cost is reduced by a factor 39.4.

The relative costs of updating thermal data of the symmetric slave facets using data at the master facets are also listed in Table 6.11. The use of *local pointer* variables (as discussed in §5.3) reduces this cost by approximately 2.1.

Figure 6.23: Photograph of ceramic mould of DS clustered bar casting

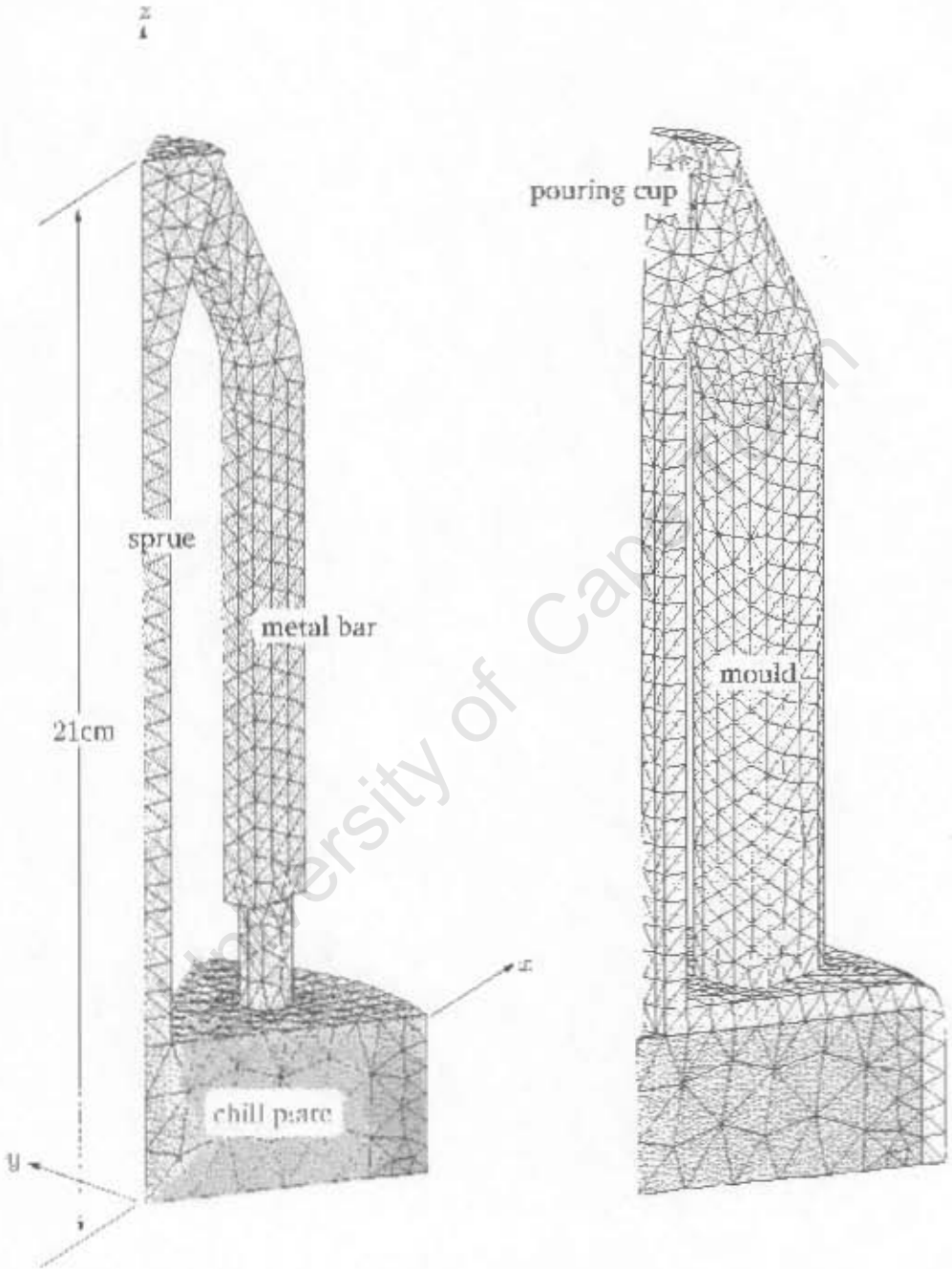

Figure 6.24: Finite element mesh of a sector of a clustered DS bar casting

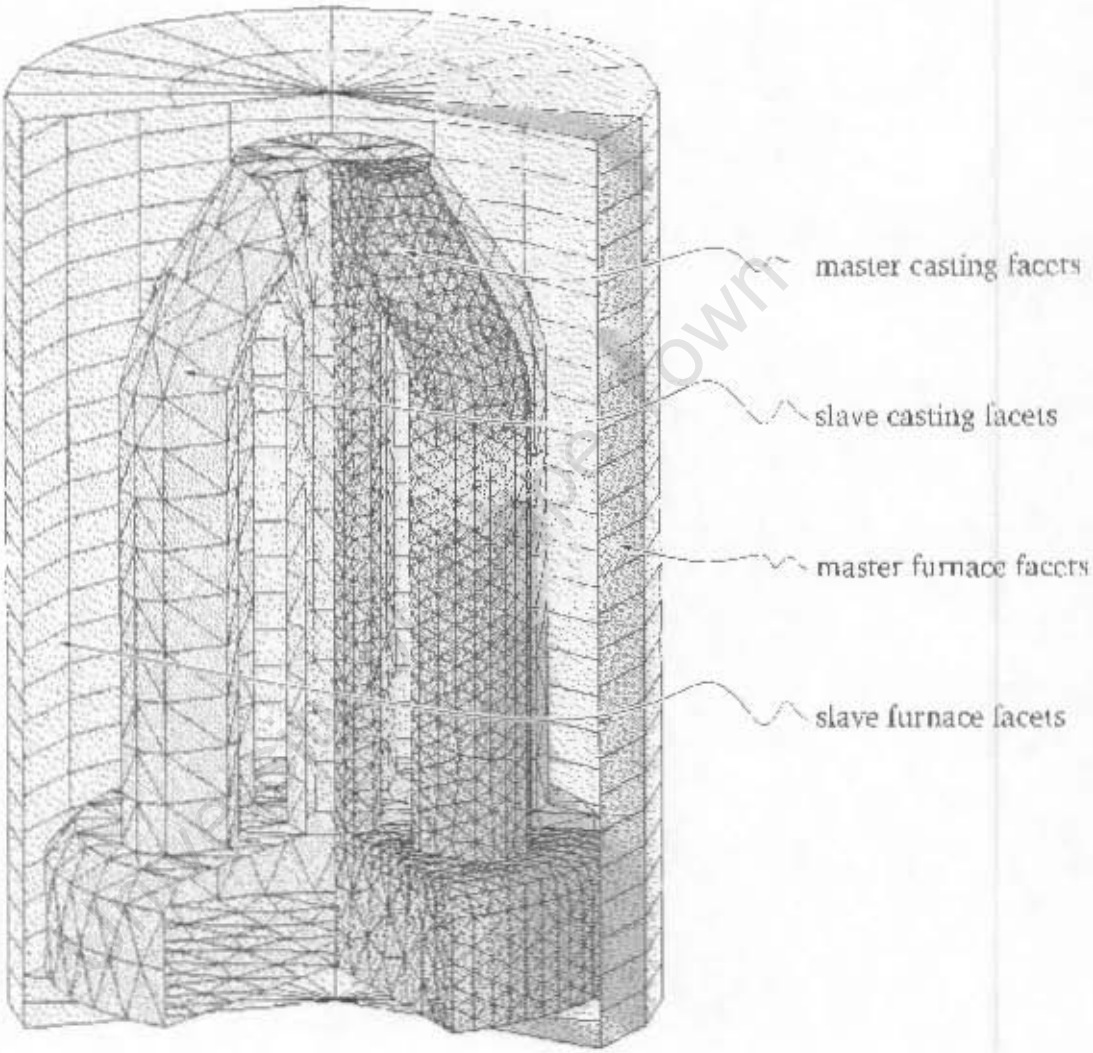

Figure 6.25: Section of radiation cavity comprising a clustered DS bar casting and furnace. Master radiating facets are shaded darkly. Facets of the fifth slave bar and many furnace facets have been removed for visual clarity

Table 6.11: Relative costs of computing the view factor database (see §4.3.3 and §4.3.4) and of updating symmetric thermal data (see §4.3.3). Cost reductions effected by invoking symmetry and by using a coarse slave facet mesh are considered separately. In each case the number of computations is proportional to the entries tabulated in the fourth, fifth and sixth columns according to the cited equations

Description	F_M	F_S	F_{max}	View factor database Eq. (4.48)	Symmetric data updates Local pointers were: not used (Eq. (5.1))	used (Eq. (5.2))
Fine slave mesh No symmetry	13912	0	13912	1.3×10^{12}	n/a	n/a
Fine slave mesh Symmetry	2251	11661	13912	4.0×10^{11}	583050	263295
Coarse slave mesh No symmetry	4407	0	4407	4.3×10^{10}	n/a	n/a
Coarse slave mesh Symmetry	2251	2156	4407	3.3×10^{10}	107800	54185

The *master–slave* symmetry linkages between the master casting facets and those of the first adjacent symmetric bar were computed using Algorithm 6. The geometries of the remaining four symmetric bars were then generated automatically from the first symmetric bar. In this way all the symmetry conditions were specified simply by inserting the following lines into the input file:

```
1  *SYMMETRY, TYPE=ROTATE, CONDITION=PROXIM
2    BAR2, BAR1,  0.,0.,0.,  0,0,1,  60.0
3  *SYMMETRY, TYPE=ROTATE, CONDITION=GENERATE
4    BAR2, 0.,0.,0.,  0,0,1,  60.0
5    BAR2, 0.,0.,0.,  0,0,1, 120.0
6    BAR2, 0.,0.,0.,  0,0,1, 180.0
7    BAR2, 0.,0.,0.,  0,0,1, 240.0
```

Material Properties and Casting Parameters

The thermophysical data are listed in Tables 6.6, 6.7, 6.8, and 6.12. The variations of emissivity of the mould surface and the furnace heaters and walls is shown in Figure 6.13.

Results

Computed temperature histories were compared with measured histories at the four locations shown in Figure 6.26. Inspection of the measured histories at these locations confirms the existence of large radial thermal gradients across each bar (dotted lines in Figures 6.27, 6.28, 6.29 and 6.30). At the lower axial height (points '1' and '2') the measured radial gradient

Table 6.12: Casting parameters for clustered directional casting

Initial metal temperature	1420 °C	
Initial mould temperature	1420 °C	
Initial chill plate temperature	20 °C	
Furnace heater temperature, T_h	1460 °C	
Furnace wall temperature, T_c	20 °C	
Casting withdrawal direction, $\hat{\mathbf{n}}_w$	$(0, 0, -1)$	
Width of the baffle zone, δ	6.3cm	
Initial vertical baffle position, b_0	1.1cm	
	Δt (min)	v_w (mm/min)
Casting withdrawal sequence	5	0
	∞	4

remains negative for first 2500s. At the higher axial height (points '3' and '4') the measured radial gradient changes sign.

By analysing two sets of simulated results it will be shown here that not only does the exchange of radiant energy between the casting and the furnace contribute to the existence of these gradients, but also the exchange of energy between the bars and the sprue themselves.

Two numerical simulations were performed. In the first simulation, the simplified radiation model presented earlier was applied. The expression in Equation (6.12) for the radiation heat flux was applied only to those facets on the mould surface which face the furnace heaters and walls directly. As before, view factors for these facets were computed using Algorithm 8. The remaining facets on the mould surface were assumed simply not to radiate at all.

Inspection of the computed histories for this simulation (dashed lines in Figures 6.27 and 6.28) shows a failure of the model to adequately predict the evolution of temperature at points on the inner side of each bar, and consequently the measured radial thermal gradients were also not predicted.

In the second simulation, the rigorous radiation model developed in Chapter 4 was applied. At the start of the simulation the database of view factors was computed and stored on disk (see Figure 4.12) in order for the database to be used in subsequent simulation runs. A subset of these views is represented in Figure 6.31. In this figure the facets which are 'visible' from a single facet are shaded darkly.

The computed histories for this simulation (solid lines in Figures 6.29 and 6.30) show better agreement between the measured and the simulated results when compared with the previous simulated results. In particular, the evolution of temperature at points on the inner side of each bar is now predicted adequately, and hence, the existence of the radial thermal gradients is also predicted.

With the results from the two simulations taken together, it can be concluded that the accuracy of numerical simulations of investment castings having complex shapes depends on the

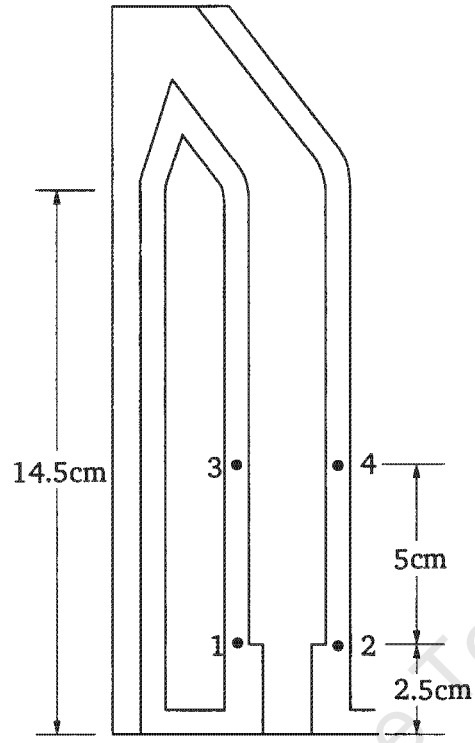

Figure 6.26: Thermocouple locations for DS clustered bar casting

accuracy with which the radiant interactions are modelled. The analyst is therefore left with no option but to treat such interactions rigorously, and to bear the consequences of a computational cost penalty.

Computed temperature distributions over the mould and the metal at two instants are shown in Figures 6.32 and 6.33. The computed shape and evolution of the mushy zone over the time interval [1300s,2500s] is shown in Figure 6.34.

Plots of this nature can provide useful information. For example, observe that the predicted solidus isotherm slants away from the central sprue. Since the primary dendrites grow in a direction perpendicular to the solidus isotherm, their growth is not vertical. Futhermore, the outward slanting of the solidus isotherm means that points on the inner side of the bar closest to the sprue are possible sites of nucleation of secondary grains. These secondary grains are undesirable in that their presence conflicts with the desired directionality of DS cast microstructure.

6.5 Summary

Four finite element models were considered. In the first model the cooling of a hypothetical equiaxed investment casting of a rectangular bar was considered. For the case of this simple geometry, the cavity radiation model developed in Chapter 4 reproduced simple blackbody

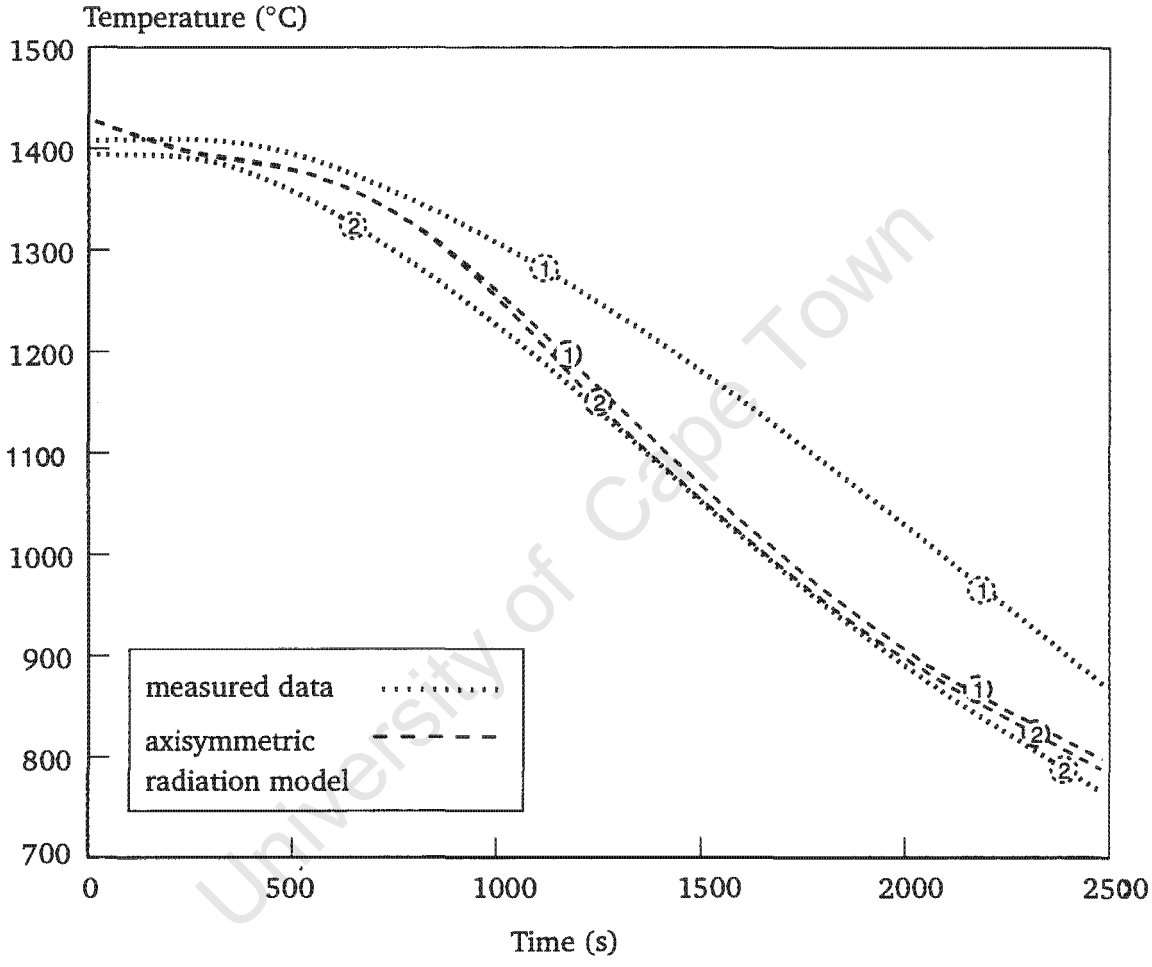

Figure 6.27: Computed and measured temperature histories at thermocouple locations '1' and 2 (*c.f.* Figure 6.26). The computed results were obtained using the simple axisymmetric radiation model

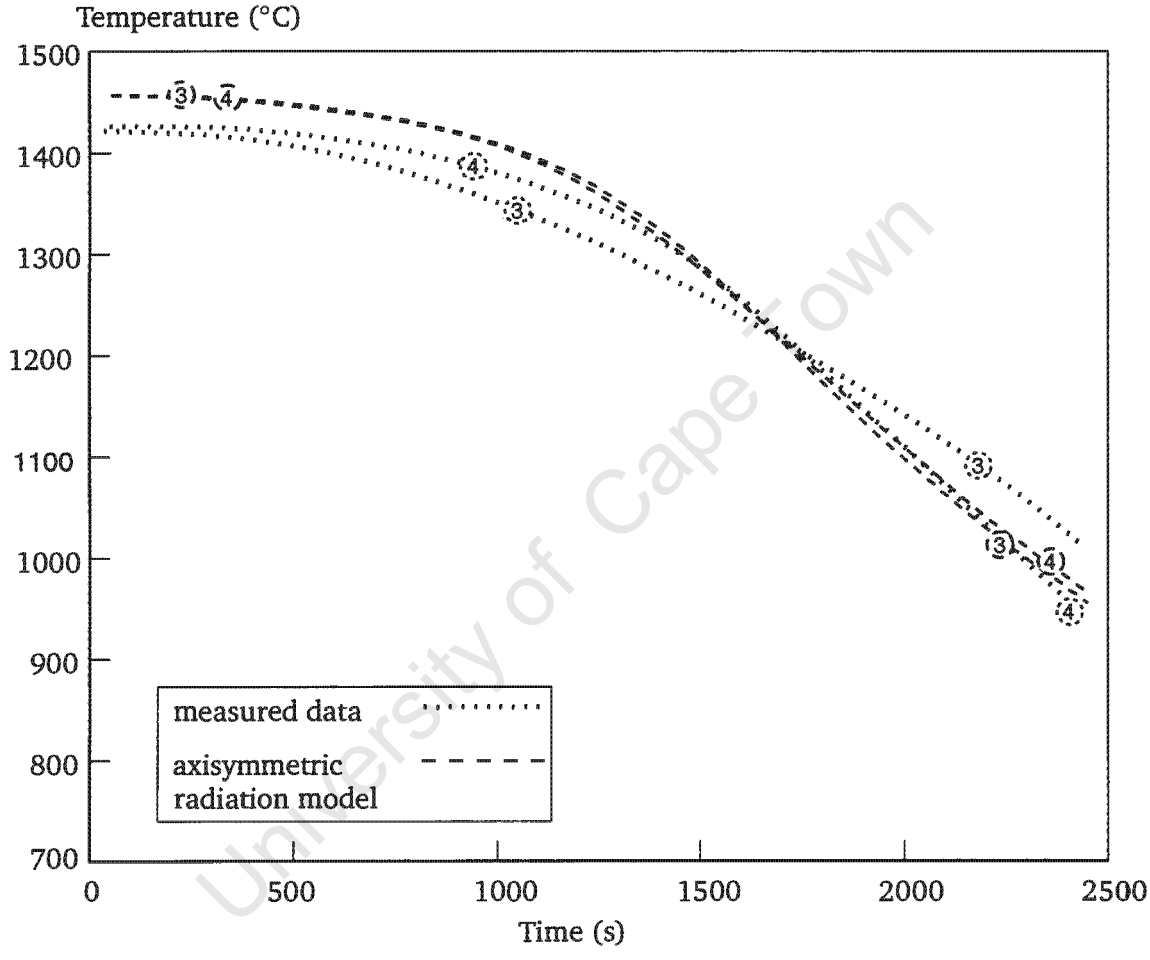

Figure 6.28: Computed and measured temperature histories at thermocouple locations '3' and 4' (*c.f.* Figure 6.26). The computed results were obtained using the simple axisymmetric radiation model

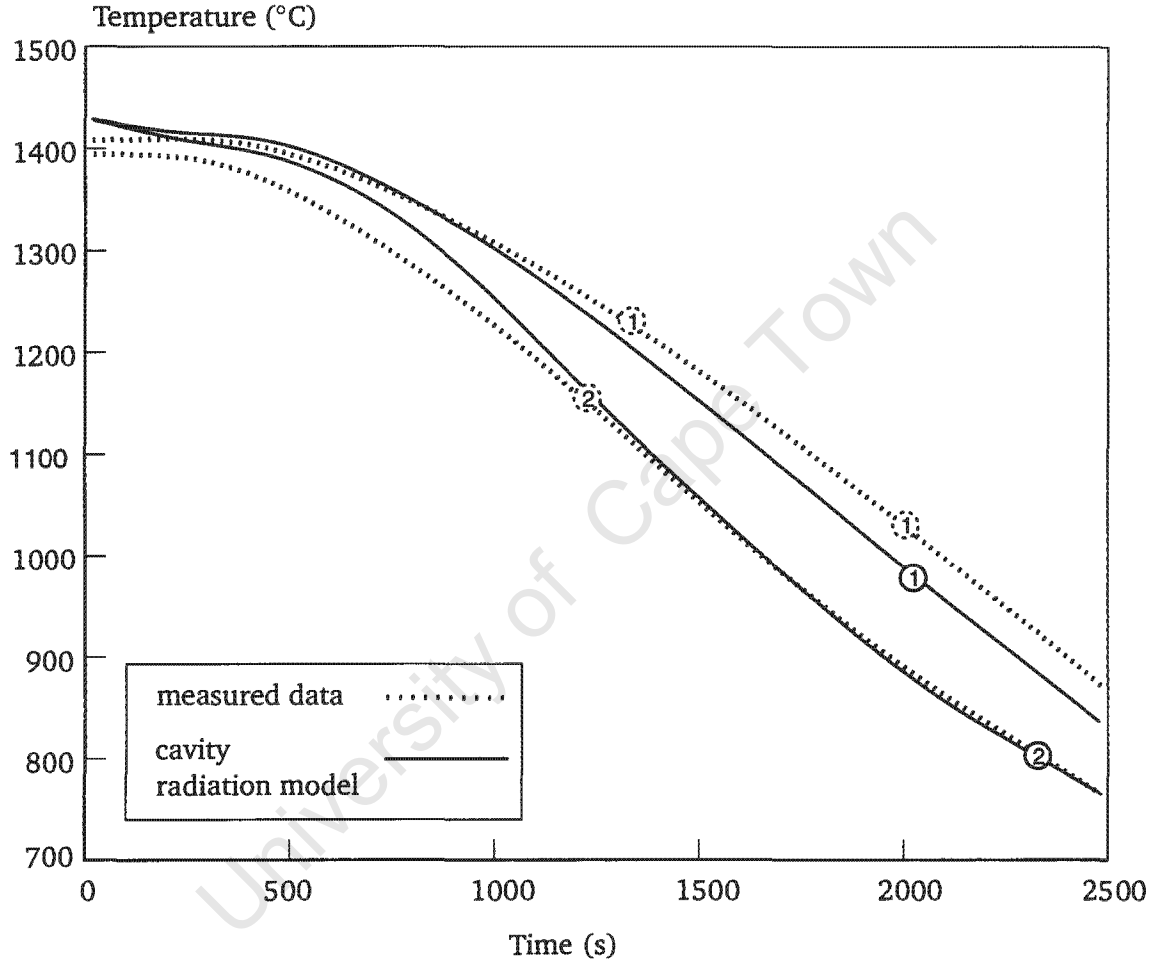

Figure 6.29: Computed and measured temperature histories at thermocouple locations '1' and 2' (*c.f.* Figure 6.26). The computed results were obtained using the 3-D cavity radiation model (Chapter 4)

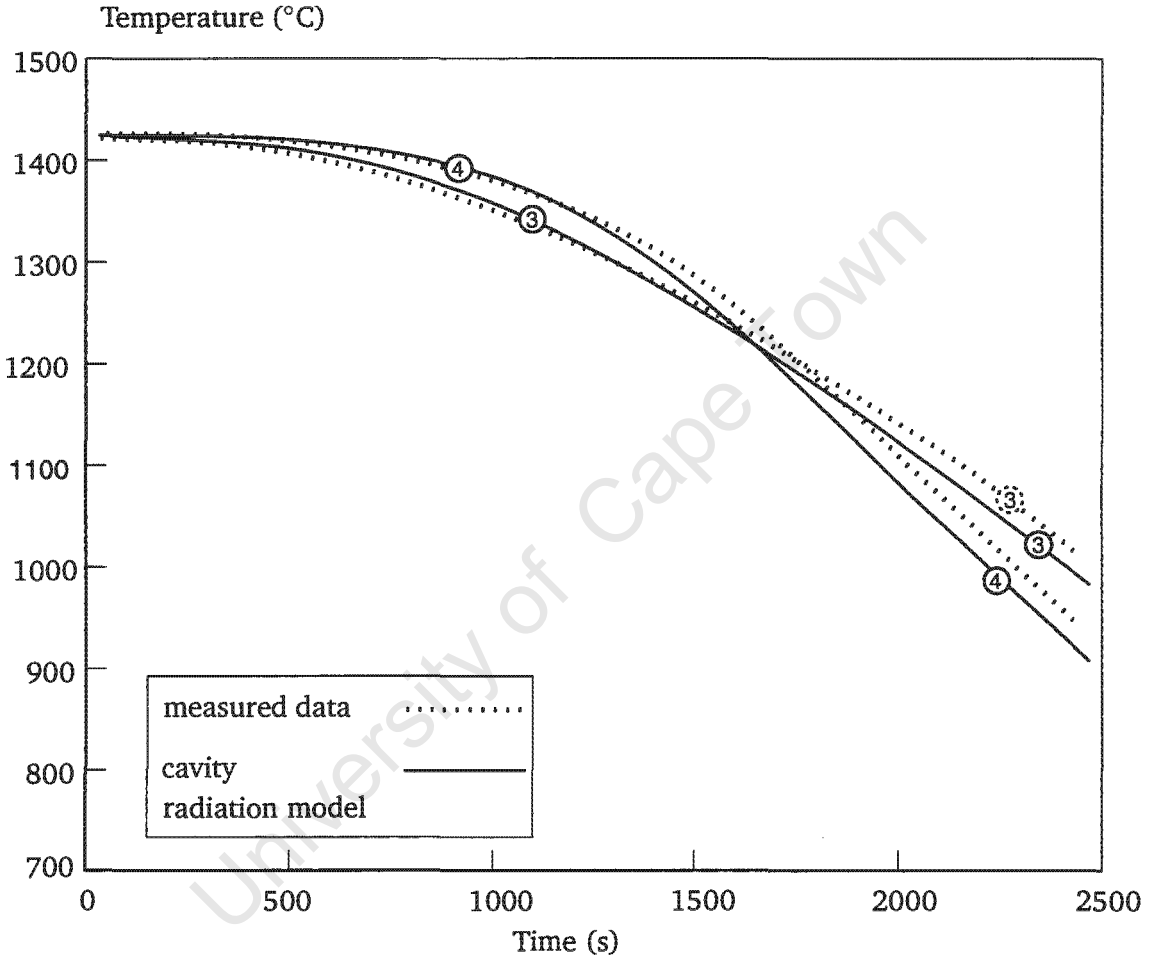

Figure 6.30: Computed and measured temperature histories at thermocouple locations '3' and 4' (*c.f.* Figure 6.26). The computed results were obtained using the 3-D cavity radiation model (Chapter 4)

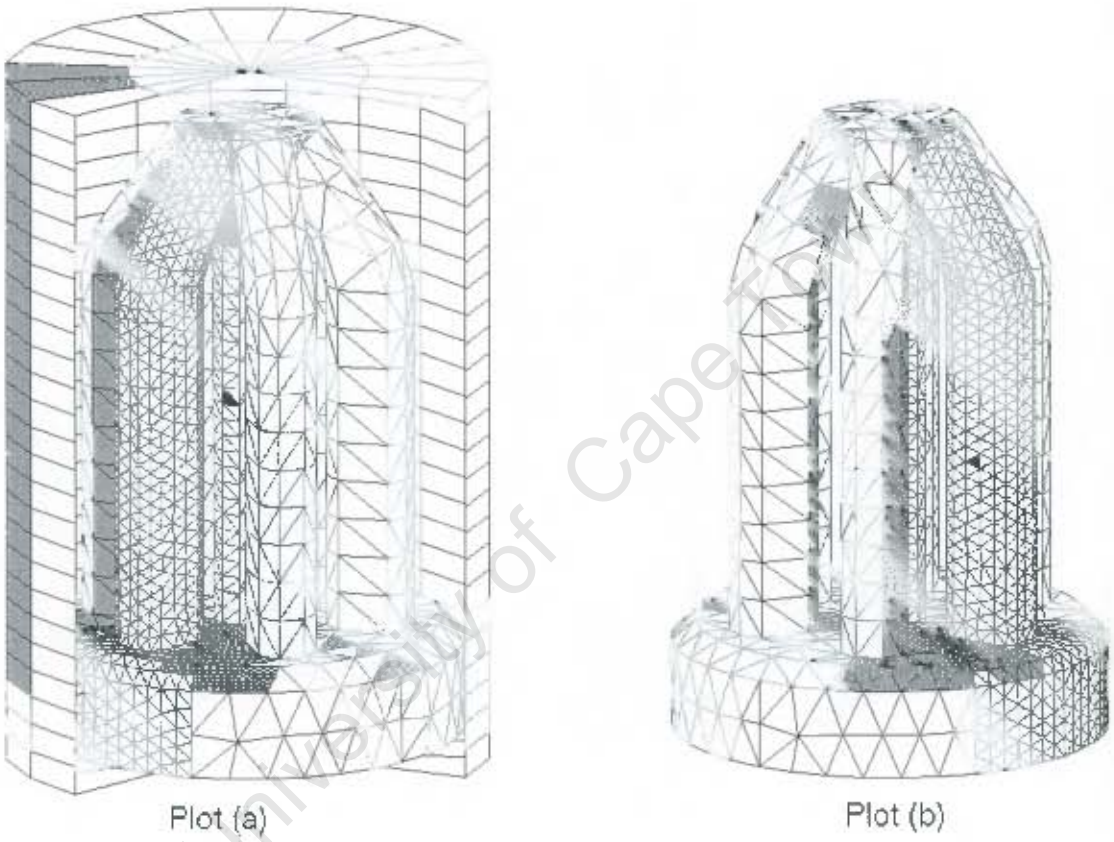

Figure 6.31: Views (shaded facets) as 'seen' from a single radiating facet (coloured black). Views computed using Algorithm 3 (§4.3.3. In Plot (a), the single facet is located on the central sprue. For visual clarity, part of furnace is excluded in Plot (a), and furnace geometry is completely excluded in Plot (b)

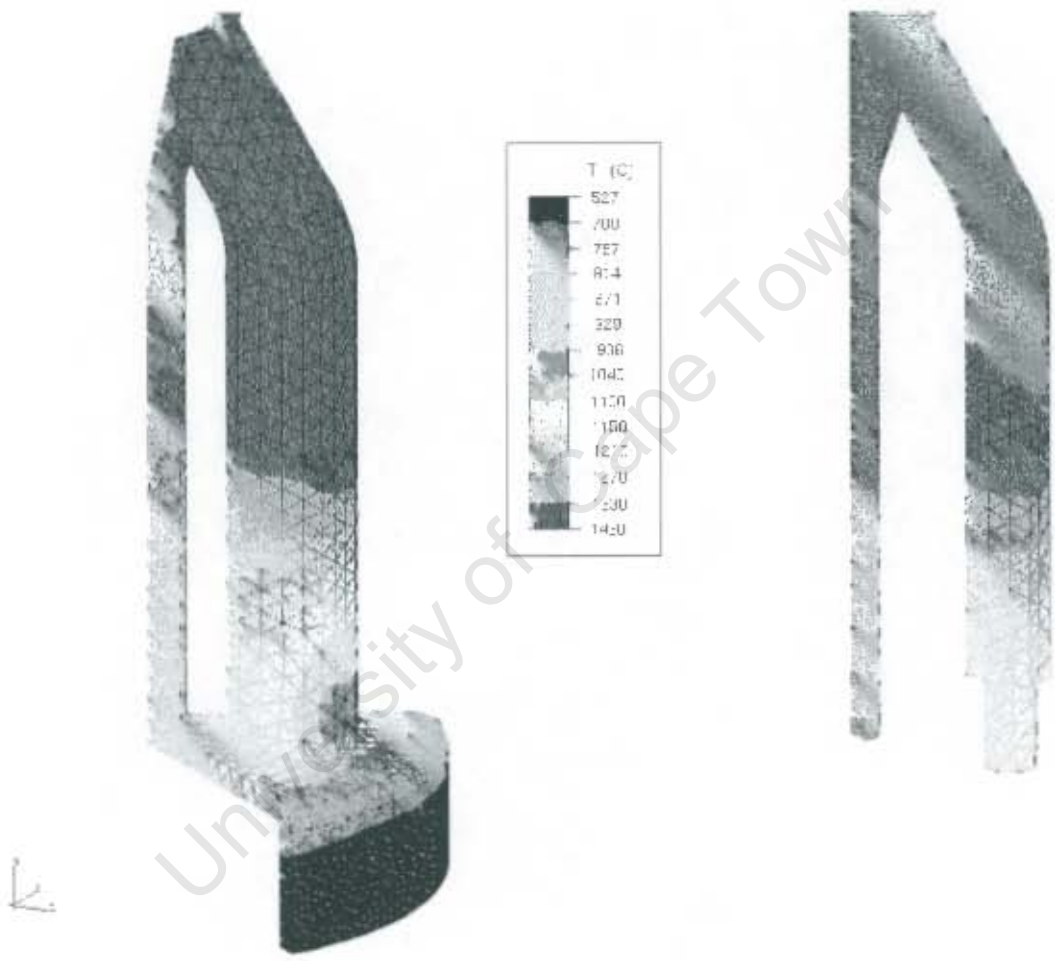

Figure 6.32: Computed temperature distributions on shell and metal surfaces 1300s after pouring

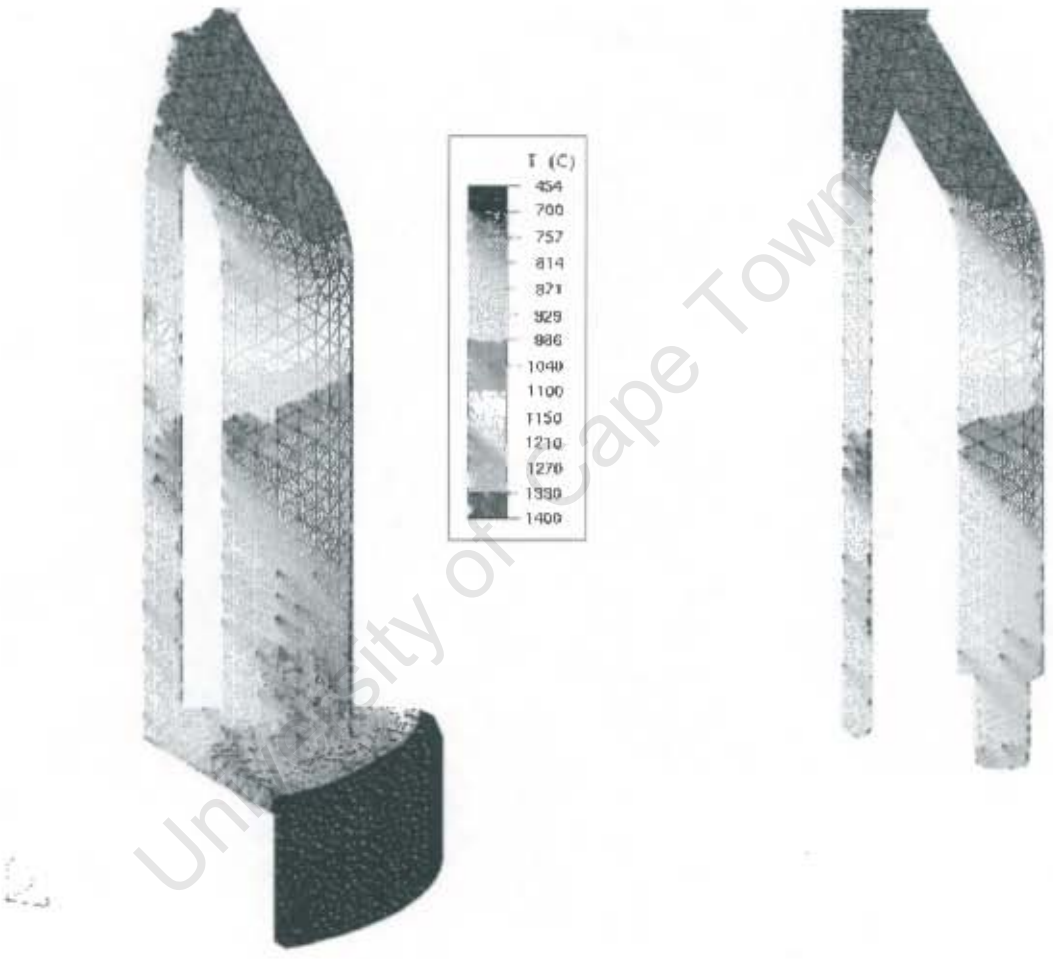

Figure 6.33: Computed temperature distributions on shell and metal surfaces 2300s after pouring

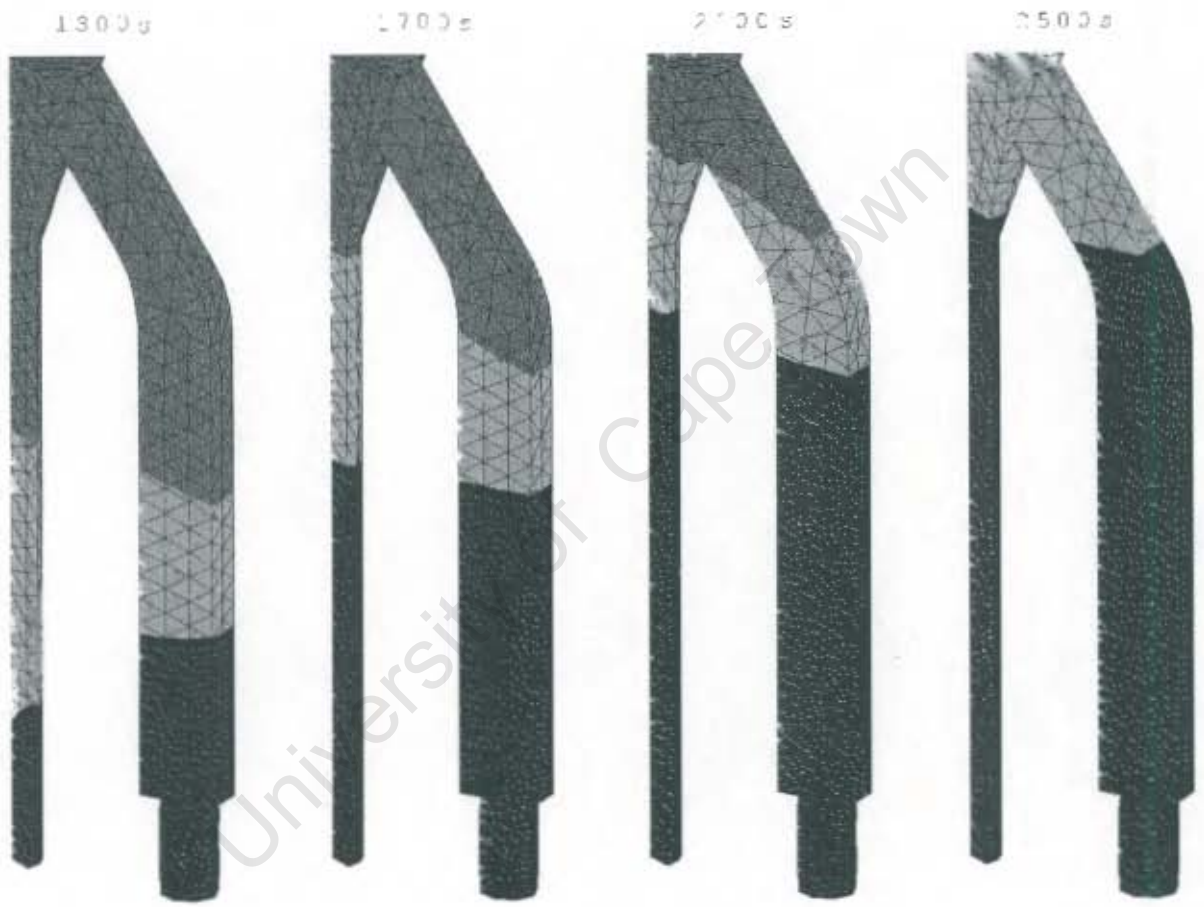

Figure 6.34: Computed evolution of mushy zone over time interval [1300s,2500s]

radiation. This confirmed the importance of implementing the coupling algorithm of §4.4, because the only possible source of large error in this model is to be found at the interface between the radiation and conduction calculations. Furthermore, the coupling algorithm effected a reduction in the average number of Newton iterations per time increment.

Next, a numerical model of the directional solidification of a single cylindrical bar was considered. The objective was to study the complexities that arise in modelling actual directional casting processes, where such complexities do not stem from the radiant interactions. In this regard, good agreement between computed and measured results was obtained when the existence of a 'thermal gap' between the solidifying metal and the chill plate was modelled.

With respect to the analysis of a tensile test specimen which was cast as a single crystal, the cross–sectional variation in the geometry of the specimen at different axial positions was found to have a profound influence on the growth of the primary dendrites in the specimen. A finite element model of the single–crystal casting of a specimen predicted, with reasonable accuracy, the spacing between the dendrite arms. The ability of such models to correlate both casting process parameters and casting geometry with the resultant microstructure was therefore confirmed.

Finally, a three–dimensional model of the directional casting of a cluster of six rectangular bars was developed. As expected, the application of a simple axisymmetric model of the radiant interaction between the furnace and the mould was found to be inadequate. It was only by application of the rigorous cavity radiation model developed in §3.3, §4.3 and §4.4 that acceptable agreement between computed and measured temperature histories was obtained. The latter model was able to account for not only the interaction between the mould and the furnace surfaces, but also between the mould surfaces themselves.

The efficacy of the symmetry algorithms of §4.3.4 was discussed. The ability to represent certain regions of the radiating cavity with a coarse mesh, and to then apply cyclical symmetry conditions over these regions, resulted in a 39–fold reduction in the computational cost.

Chapter 7

Conclusion

The directional investment casting process involves complex interactions of various mechanisms of heat and mass transfer in spatially complex domains and in the presence of a change of phase. In particular, the transfer of heat occurs within the furnace in the form of conduction, convection and radiation.

This transfer may be described in terms of conservation laws in which these modes are coupled. The mathematical statement of these laws is typically too complex to facilitate the derivation of analytical solutions. Complexities arise from the need to account both for the release of latent heat accompanying the change of phase, and for radiant interactions which are non–local in character.

The focus of this thesis has therefore been on the development of numerical models of the directional investment casting process. The abovementioned complexities have been addressed by coupling a model of the radiant interactions to a finite element model of the conduction heat transfer.

A 'specific heat'–based formulation was adopted to account for the change of phase during solidification. The solid and liquid phases were not treated separately. Instead, conservation of heat energy was prescribed over the entire region, and a moving planar heat source located between the solidus and liquidus isotherms accounted for the liberation of latent heat.

A Galerkin isoparametric finite element formulation using first–order hexahedral elements was applied. The well–known backward–difference temporal algorithm, together with a modified Newton iterative method, was used to solve the non–linear equations at selected instants during the solidification history of a casting.

In formulating a description of the radiation, a radiating cavity was defined as the union of the exposed surfaces of: the casting and shell mould, the furnace chamber walls, the furnace heating elements, and the baffle plates. The interactions were analysed in terms of emitted, absorbed and reflected radiant energy components for each infinitesimal surface element.

By applying a diffuse–grey approximation to these energies, an expression for the net heat flux

for each infinitesimal surface was derived. This expression is a function of the average radiosity for the surface, as well as an infinite set of view factors which depend only on the magnitude of the area of the surface and its orientation with respect to all other surfaces. Unfortunately, the radiosity of each surface depends integrally on the radiosities of every other surface, so that analytical solutions are generally not obtainable.

To obtain a numerical solution to the radiosities, therefore, the geometry of the furnace was assumed to be comprised of a finite number of bilinear facets, with some of these facets being exactly coincident with the exterior elemental faces of the finite element mesh. By further assuming that the radiant quantities do not vary significantly over each facet, the description of the radiant interactions was reduced to a system of linear equations for the unknown radiosities at each increment in time. This system was solved using a Gauss–Seidel relaxation method.

The quest for computed solutions to these radiant interactions requires a level of computing resource that is often not in proportion with the impact of the radiation on the overall problem. A primary objective of this thesis was therefore to extend the modelling capability by developing specialised techniques to minimise both the computational cost as well as the time spent by the analyst in setting up the models. Specific innovations included:

- the exploitation of planes of geometric symmetry which may be present in the radiating cavity in a manner which drastically reduces the required number of degrees of freedom without a significant loss of accuracy
- the development of an algorithm to couple the finite element calculations to the radiation calculations
- the derivation of an analytical solution to the abovementioned view factors applicable to the view between two bilinear facets.
- the simulation of the relative motion of the casting and the furnace without requiring the view factor database to be reconstructed at every time increment

Four increasingly complex numerical models were studied. From the results obtained for the model of the clustered directional casting and the axisymmetric models, it is evident that the radiation interactions contribute critically to the solidification behaviour of the casting.

In the case of the clustered casting, the presence of radial thermal gradients across the bars arose not only from the interaction of the casting and ceramic mould surfaces with the furnace, but also from a 'self–interaction' between the various surfaces. It was shown that such interactions could only be simulated correctly using a radiation model which accounted for a contribution from each surface to the state of the radiation of the cavity as a whole.

The resulting 'non–local' radiation model was found to translate into a high cost penalty with respect to the computation of the database of view factors. However, by application of algorithms developed in this thesis, the computational cost was reduced by a factor 39 for the model of the clustered casting.

The spacing between the primary dendrite arms in the casting of a tensile test specimen was measured. Its variation correlated with the variation in the geometry of the specimen. The reasonable agreement between computed and measured values for this variation demonstrated the ability of such modelling techniques to provide a link between casting process parameters, the casting geometry and the resultant microsctructure.

Analytical View Factor Expression

The analysis begins with the surface integral formula (4.32) for the view of S^n from S^m:

$$F_{mn} = \int_{A^n} \frac{\cos(\beta(\mathbf{c}^m, \mathbf{x}^*)) \cos(\beta(\mathbf{x}^*, \mathbf{c}^m))}{\pi \left|\mathbf{c}^m - \mathbf{x}^*\right|^2} \, \mathrm{d}A^*$$

Application of Stokes' Theorem reduces the integration to a single contour integration around the boundary of S^n, yielding

$$F_{mn} = \frac{1}{2\pi} \hat{\mathbf{n}}^m \cdot \oint_{\partial A^n} \frac{(\mathbf{c}^m - \mathbf{x}^*)}{\left|\mathbf{c}^m - \mathbf{x}^*\right|^2} \times \mathrm{d}\mathbf{x}^*$$

If the facet S^n consists of *sides* edges, F_{mn} may be written

$$F_{mn} = \frac{1}{2\pi} \hat{\mathbf{n}}^m \cdot \sum_{i=1}^{\substack{sides \\ \text{of } S^n}} \int_{\mathbf{x}^i}^{\mathbf{x}^{i+1}} \frac{(\mathbf{c}^m - \mathbf{x}^*)}{\left|\mathbf{c}^m - \mathbf{x}^*\right|^2} \times \mathrm{d}\mathbf{x}^*$$

as long as it is understood that $\mathbf{x}^{sides+1} \equiv \mathbf{x}^1$.

If S^n is constrained to have straight edges, then for $\mathbf{x}^*$ located on the edge $\overline{\mathbf{x}^i\mathbf{x}^{i+1}}$, there must exist some $\alpha \in [0, 1]$ s.t. $\mathbf{x}^* = \mathbf{x}^i + \alpha(\mathbf{x}^{i+1} - \mathbf{x}^i)$, so that F_{mn} can be written as

$$\begin{aligned} F_{mn} &= \frac{1}{2\pi} \hat{\mathbf{n}}^m \cdot \sum_{i=1}^{\substack{sides \\ \text{of } S^n}} \mathbf{d}^i \times \int_0^1 \frac{(\boldsymbol{\mu}^i + \mathbf{d}^i\alpha)}{\left|\boldsymbol{\mu}^i + \mathbf{d}^i\alpha\right|^2} \, \mathrm{d}\alpha \\ &= \frac{1}{2\pi} \hat{\mathbf{n}}^m \cdot \sum_{i=1}^{\substack{sides \\ \text{of } S^n}} \mathbf{d}^i \times \boldsymbol{\mu}^i \int_0^1 \frac{1}{\left|\boldsymbol{\mu}^i + \mathbf{d}^i\alpha\right|^2} \, \mathrm{d}\alpha \end{aligned}$$

where $\mathbf{d}^i \equiv \mathbf{x}^{i+1} - \mathbf{x}^i$ and $\boldsymbol{\mu}^i \equiv \mathbf{x}^i - \mathbf{c}^m$.

The integrand can be rearranged to give

$$F_{mn} = \frac{1}{2\pi} \hat{\mathbf{n}}^m \cdot \sum_{i=1}^{\substack{sides \\ \text{of } S^n}} \mathbf{d}^i \times \boldsymbol{\mu}^i \int_{\frac{\boldsymbol{\mu}^i \cdot \mathbf{d}^i}{(d^i)^2}}^{1 + \frac{\boldsymbol{\mu}^i \cdot \mathbf{d}^i}{(d^i)^2}} \left[\xi^2 + \left(\frac{\mu^i d^i}{(d^i)^2} \right)^2 + \left(\frac{\boldsymbol{\mu}^i \cdot \mathbf{d}^i}{(d^i)^2} \right)^2 \right]^{-1} \mathrm{d}\xi \qquad (1)$$

with $d^i \equiv \left|\mathbf{d}^i\right|$ and $\mu^i \equiv \left|\boldsymbol{\mu}^i\right|$. The integral in (1) is in a standard form, and can therefore be integrated easily.

Recognizing that

$$(\mu^i)^2(d^i)^2 - (\mu^i \cdot \mathbf{d}^i)^2 = (\mu^i \times \mathbf{d}^i)^2$$

and

$$(d^i)^2 + \mu^i \cdot \mathbf{d}^i = \mathbf{d}^i \cdot \mu^{i+1}$$

the solution to (1) is then

$$F_{mn} = \frac{1}{2\pi} \sum_{i=1}^{\substack{sides \\ of\ S^n}} \hat{\mathbf{n}}^m \cdot \frac{\omega^i}{|\omega^i|} \left[\arctan\left(\frac{\mathbf{d}^i \cdot \mu^{i+1}}{|\omega^i|} \right) - \arctan\left(\frac{\mathbf{d}^i \cdot \mu^i}{|\omega^i|} \right) \right] \tag{2}$$

with $\omega^i \equiv \mathbf{d}^i \times \mu^i$.

Letting

$$\theta = \arctan\left(\frac{\mathbf{d}^i \cdot \mu^{i+1}}{|\omega^i|} \right) \quad \text{and} \quad \psi = \arctan\left(\frac{\mathbf{d}^i \cdot \mu^i}{|\omega^i|} \right)$$

then, using standard trigonometric identities, is is easy to show that

$$\begin{aligned} \cos(\theta - \psi) &= \cos(\theta)\cos(\psi) + \sin(\theta)\sin(\psi) \\ &= \frac{(\omega^i)^2 + (\mathbf{d}^i \cdot \mu^{i+1})(\mathbf{d}^i \cdot \mu^i)}{\sqrt{[(\omega^i)^2 + (\mathbf{d}^i \cdot \mu^{i+1})^2][(\omega^i)^2 + (\mathbf{d}^i \cdot \mu^i)^2]}} \end{aligned} \tag{3}$$

But, recognising that $\mu^i + \mathbf{d}^i = \mu^{i+1}$, and with some algebraic manipulation

$$\begin{aligned} (\omega^i)^2 + (\mathbf{d}^i \cdot \mu^{i+1})(\mathbf{d}^i \cdot \mu^i) &= (d^i)^2 \mu^{i+1} \cdot \mu^i \\ (\omega^i)^2 + (\mathbf{d}^i \cdot \mu^{i+1})^2 &= (d^i)^2 (\mu^{i+1})^2 \\ (\omega^i)^2 + (\mathbf{d}^i \cdot \mu^i)^2 &= (d^i)^2 (\mu^i)^2 \end{aligned}$$

Equation (3) therefore becomes

$$\cos(\theta + \psi) = \frac{\mu^{i+1} \cdot \mu^i}{|\mu^{i+1}|\,|\mu^i|} = \hat{\mu}^{i+1} \cdot \hat{\mu}^i \tag{4}$$

Finally, using (4), the solution (2) simplifies to

$$F_{mn} = \frac{1}{2\pi} \sum_{i=1}^{\substack{sides \\ of\ S^n}} \hat{\mathbf{n}}^m \cdot \hat{\boldsymbol{\omega}}^i \arccos\left(\hat{\mu}^{i+1} \cdot \hat{\mu}^i \right) \tag{5}$$

Bibliography

[1] V. Pontikis, editor. *Computer Simulation in Materials Science — Nano/Meso/Macroscopic Space and Time Scales*, NATO – ASI. Kluwer Academic Publisher, 1996.

[2] T.S. Piwonka, V. Voller, and L. Katgerman, editors. *Modelling of Casting, Welding and Advanced Solidification Processes — VI*. TMS, 1993.

[3] F. Giamei. Solidification process modelling: Status and barriers. *JOM*, pages 51–53, January 1993.

[4] M. McLean. *Directionally Solidified Materials for High Temperature Service*. The Metals Society, Bristol, 1983.

[5] J.W. Rutter W.A. Tiller, K.A. Jackson and B. Chalmers. The redistribution of solute atoms during the solidification of metals. *Acta. Metall.*, 1:428, 1953.

[6] M.H. Burden and J.D. Hunt. *J. Crystal Growth*, 22:99–109, 1974.

[7] M. Rappaz *et al*. Modelling of single-crystal turbine blade castings. In M. Rappaz, M.R. Özgü, and K.W. Mahin, editors, *Modelling of Casting, Welding and Advanced Solidification Processes — V*, pages 635–640. TMS, 1991.

[8] J.R. Howell. Thermal radiation in participating media: The past, the present, and some possible futures. *J. Heat Transfer*, 110:1220–1229, 1988.

[9] T.K. Pratt, F. Landis, and A.F. Giamei. Iterative non-linear thermal analysis of directional solidification using a fast elliptic solver. *Numer. Heat Transfer*, 4:199–213, 1981.

[10] A.F. Giamei, R.J. Mador, M.O. Duffy, and F. Landis. Finite element simulation of the directional solidification process for cylinders (2D) and rectangular bars (3D). In S. Kou and R Mehrabian, editors, *Modelling and Control of Casting and Welding Processes*, pages 433–448. TMS, 1986.

[11] P.J. Kotschy and P. Carter. Finite element modelling of directional processing with an emphasis on post-processing. In D. Hibbit, editor, *ABAQUS Users' Conference 1990*, page 78. HKS, 1990.

[12] A.F. Giamei, R.J. Mador, M.O. Duffy, and P.M. Morris. Simulation of superalloy castings. *JOM*, pages 7–10, February 1988.

[13] A.F. Giamei, R.J. Mador, M.O. Duffy, and P.M. Morris. Superalloy casting perspectives. In *Technology for Premium Quality Castings*, pages 15–28, 1988.

[14] L. Vermont des Roches and J.C. Chevrier. In J. Beech and H. Jones, editors, *Solidification Processing 1987*, page 522. The Institute of Metals, 1988.

[15] F. Dupret *et al.* Global modelling of heat transfer in crystal growth furnaces. *Int. J. Heat Mass Transfer*, 33:1849–1871, 1990.

[16] N. Hofmann, U. Reske, H. Vor, and P.R. Sahm. Numerical simulation of directional solidification using the bridgman process. *Giessereiforschung*, 43(3):101–106, 1991.

[17] N. Hofmann, U. Reske, A. Bader, and P.R Sahm. Numerical simulation of directional solidification using the bridgman process II. *Giessereiforschung*, 44(3):113–120, 1992.

[18] K.O. Yu, J.A. Oti, M. Robinson, and R.G. Carlson. Solidification modelling of complex-shaped single-crystal turbine airfoils. In S.D. Antolovich *et al*, editor, *Superalloys 1992*, pages 135–144. TMS, 1992.

[19] J.S. Tu and R.K. Foran. The application of defect maps in the process modelling of single-crystal investment casting. *JOM*, pages 26–28, June 1992.

[20] J.S. Tu, D.M. Olinger, and A.M. Hines. Computer-aided development of an investment casting process. *JOM*, pages 29–32, October 1993.

[21] A.L. Purvis, C.R. Hanslits, and R.S. Diehm. Modelling characteristics for solidification in single-crystal, investment-cast superalloys. *JOM*, pages 38–41, January 1994.

[22] G.K. Upadhya, S. Das, U. Chandra, and A.J. Paul. Modelling the investment casting process: A novel approach for view factor calculations and defect prediction. *Appl. Math. Model.*, 19(6):354–362, 1995.

[23] Hibbit, Karlson and Sorenson, Inc. *ABAQUS/Standard User's Manual I & II.* Providence, Rhode Island, USA.

[24] R.F. Smart. High strength and integrity investment castings. *Materials & Design*, 10(6):301–305, 1989.

[25] R.L. Dreshfield. Defects in nickel-base superalloys. *JOM*, pages 16–21, July 1987.

[26] F.L. Versnyder. In R.F. Hehemann and G. Mervin, editors, *High Temperature Metals*, New York, 1959. Wiley-Interscience.

[27] F.L. Versnyder and M.E. Shank. *Mat. Sci. Eng.*, 6:213, 1970.

[28] W.J. Molloy. Investment-cast superalloys — A good investment. *Advanced Materials and Processes*, 10:23–29, 1990.

[29] P. Kotschy and P. Carter. Predicting microstructure in metal castings. In *Finite Element Methods in South Africa 1992*, pages 297–312. FRD/UCT Centre for Research in Computational and Applied Mechanics, University of Cape Town, 1992.

[30] P. Kotschy. Internal report no. 450/27471, CSIR. page 43, May 1990.

[31] H.S. Whitesell, L. Li, and R.A. Overfelt. Influence of solidification variables on the dendrite arm spacings of ni–based superalloys. *Metall. Trans. B*, pages 546–551, June 2000.

[32] M. Morikawa E. Niyama, T. Uchida and S. Saito. A method of shrinkage prediction and its application to steel casting practice. In *International Foundry Congress*, pages 33–41. TMS, 1988.

[33] E. Niyama *et al. AFS Int. Cast Metals J.*, 7(3):52–63, 1982.

[34] J. Coughlin T.Z. Kattamis and M.C. Flemmings. *Trans. Metall. Soc. AIME*, 239:1504, 1967.

[35] K.A. Jackson and J.D. Hunt. Lamellar and rod eutectic growth. *Trans. Metall. Soc. AIME*, 239:1129, 1966.

[36] T.Z. Kattamis A.K. Bhambri and J.E. Morral. *Metall. Trans.*, 68:523, 1975.

[37] W. Gust, editor. *Institution of Metallurgists. Series 3. Number 11*, volume 1, 1979.

[38] M. Cross, C. Bailey, P. Chow, Y. Fryer, and K. Pericleous. Multiphysics modelling of the metals casting process. *Proc. R. Soc. Lond. A*, 452:459–486, 1996.

[39] M. Trovant and S.A. Argyropoulos. Mathematical modeling and experimental measurements of shrinkage in the casting of metals. *Canadian Metallurgical Quarterly*, 35(1):75–84, 1996.

[40] M. Cross, S. Bounds, G. Moran, K. Pericleous, and T.N. Croft. A computational model for defect prediction in shape castings based on the interaction of free surface flow, heat transfer, and solidification phenomena. *Metall. Trans. B*, 31(B):515–527, June 2000.

[41] M.N. Özisik. *Heat Conduction*. John Wiley and Sons, Inc., New York, 1980.

[42] R. Siegel and J.R. Howell. *Thermal Radiation Heat Transfer*. McGraw-Hill Book Company, New York, 1972.

[43] J.B. Fourier. *Theorie Analytique de la Chaleur*. Paris, 1822. English translation by A. Freeman, Dover Publications, New York, 1955.

[44] G.B. Arfken and H.J. Weber. *Mathematical Methods for Physicists*. Academic Press, San Diego, 1995.

[45] G. Lam and B.P. Clapeyron. *Ann. Chem. Phys*, 47:250–256, 1831.

[46] J. Stefan. *Ann. Chem. Phys. (Wiedemannsche Annalen)*, 42:269–286, 1891.

[47] T.R. Goodman. *Trans. Am. Soc. Mech. Eng.*, 80:335–342, 1958.

[48] T.R. Goodman. *J. Heat Transfer*, 83(c):83–86, 1961.

[49] G. Poots. *Int. J. Heat Mass Transfer*, 5:525, 1962.

[50] R.H. Tien and G.E. Geiger. *J. Heat Transfer*, 90(c):27–31, 1968.

[51] J.C. Muehlbauer, J.D. Hatcher, D.W. Lyons, and F.E. Sunderland. *J. Heat Transfer*, 95(c):324–331, 1973.

[52] K. Mody and M.N. Özisik. *Lett. Heat Mass Transfer*, 2:487–493, 1975.

[53] Y.K. Chuang and J. Szekely. *Int. J. Heat Mass Transfer*, 14:1285–1295, 1971.

[54] H. Budhia and F. Dreith. *Int. J. Heat Mass Transfer*, 16:195–211, 1973.

[55] D.S. Filey, F.T. Smith, and G. Poots. *Int. J. Heat Mass Transfer*, 17:1507, 1974.

[56] C.L. Hwang and Y.P. Shih. *Int. J. Heat Mass Transfer*, 18:689–695, 1975.

[57] B.A. Boley. *J. Math. Phys.*, 40:300–313, 1961.

[58] B.A. Boley. *Int. J. Eng. Sci.*, 6:89–111, 1968.

[59] Y.F. Lee and B.A. Boley. *Int. J. Eng. Sci.*, 11:1277, 1973.

[60] M.N. Özisik and S. Gereri. *J. Chem. Eng.*, 55:145–148, 1977.

[61] N.M.H. Lightfoot. *Proc. London Math. Soc.*, 31:97–116, 1929.

[62] H. Budhia and F. Kreith. *Int. J. Heat Mass Transfer*, 16:195–211, 1973.

[63] R.D. Richtmyer. *Principles of Mathematical Physics*. Springer-Verlag, New York, 1978.

[64] P.A.M. Dirac. *The Principles of Quantum Mechanics, 3rd Edition*. Clarendon Press, Oxford, 1947.

[65] J. Crank. *Free Moving Boundary Problems*. Clarendon Press, Oxford, 1984.

[66] R.W. Lewis and P.M. Roberts. *Appl. Sci. Res.*, 44:61–92, 1987.

[67] M.O. Duffy, P.M. Morris, and R.J. Mador. Casting solidification analysis and experimental verification. *Materials and Design*, 10:287–291, 1989.

[68] K.S. Kim and B. Yimer. Thermal radiation heat transfer effects on solidification of finite concentric cylindrical medium-enthalpy models and P-1 approximation. *Numer. Heat Transfer*, 14:483–498, 1988.

[69] M. Planck. *Ann. Physik*, 4:553–563, 1901.

[70] J. Liu, T. Lee, and W. Hwang. *Mat. Sci. and Tech.*, 7:954–964, October 1991.

[71] J.L. Desbiolles, Ph. Gilgien, T. Imwenkelried, M. Rappaz, F. Suter, and Ph. Thévoz. Modelling of single crystal turbine blade castings. In M. Rappaz, M.R. Özgü, and K.W. Mahin, editors, *Modelling of Casting, Welding and Advanced Solidification Processes — V*, pages 635–640. TMS, 1991.

[72] R.L. Long. *J. Eng. Power*, 87:277–280, 1965.

[73] R.R. Hibbard. *Solar Energy*, 5:129–132, 1961.

[74] O.C. Zienkiewicz. *The Finite Element Method — Third Edition*. McGraw–Hill, London, 1977.

[75] Hibbit, Karlson and Sorenson, Inc. *ABAQUS Theory Manual*. Providence, Rhode Island, USA.

[76] V. Comini, S. Del Guidice, R.W. Lewis, and O.C. Zienkiewicz. Finite element solutions of non–linear heat conduction problems with special reference to phase change. *Int. J. Num. Methods in Eng.*, 8:613–624, 1974.

[77] L.A. Crivelli and S.R. Idelsohn. A temperature–based finite element solution for phase–change problems. *Int. J. Num. Methods in Eng.*, 23:99–119, 1986.

[78] A.J. Dalhuijsen and A. Segal. Comparison of finite element techniques for solidification problems. *Int. J. Num. Methods in Eng.*, 23:1807–1829, 1986.

[79] V.R. Voller and C.R. Swaminathan. Fixed grid techniques for phase change problems: A review. *Int. J. Num. Methods in Eng.*, 30:875–898, 1990.

[80] B. Carnahan, H.A. Luther, and J.O. Wilkes. *Applied Numerical Methods*. John Wiley and Sons, Inc., New York, 1969.

[81] J.R. Howell. Application of the Monte Carlo method to heat transfer. In T.F. Irvine and J.P. Harnett, editors, *Advances in Heat Transfer*, volume 5, New York, 1968. Academic Press.

[82] J.D. Maltby and P.J. Burns. Performance, accuracy, and convergence in a three–dimensional Monte Carlo radiative heat transfer simulation. *Numer. Heat Transfer*, 19(B):191–209, 1991.

[83] A. Haidekker, A. Charette, and Y.S. Kocaefe. Application of the hybrid zone/Monte Carlo method to 3–D curvilinear grids in radiative heat transfer. *Int. J. Num. Methods in Eng.*, 37:203–216, 1994.

[84] The World Wide Web and FTP server (URL: `http://www.netlib.org`) at the University of Tennessee, Knoxville, maintains an extensive repository of mathematical software, papers and databases.

[85] A guide to freely and commercially available software is also available at the URL: `http://gams.nist.gov`.

[86] N. Comins and P. Kotschy *et al.* Internal report, CSIR. Maraba Project §113122—Instrumented Mould Casting and Modelling, September 1990.

[87] P. Carter and P. Kotschy *et al.* Internal report no. 450/27471, CSIR. First Report on the Intelligent Processing of Materials. New Investment Program, October 1990.

[88] P. Carter and P. Kotschy *et al.* Internal step project report, CSIR. Modelling of Directional Solidification: Comparison of Simulation with Experimental Results, July 1991.

[89] N. Comins and P. Kotschy *et al.* Internal report, CSIR. Maraba Project §113122—Instrumented Mould Casting and Modelling, September 1991.

[90] N. Comins and P. Kotschy *et al.* Internal report, CSIR. Maraba Project §113122—Instrumented Mould Casting and Modelling, February 1992.

[91] N. Comins and P. Kotschy *et al.* Internal report, CSIR. Maraba Project, April 1993.

[92] N. Comins and P. Kotschy *et al.* Internal report, CSIR. Maraba Project §253-02 Solidification Modelling, February 1994.

[93] *Metals Handbook, 9th Edition*, volume 3. ASME, 1980.

[94] Y.S. Touloukian and D.P. Dewitt. *Thermal Radiative Properties: Non-Metallic Solids*. 1972.

[95] R.W. Lewis and R.S. Ransing. A correlation to describe interfacial heat transfer during solidification and its use in the optimal feeding design of castings. *Metall. Trans. B*, 29(B):437–448, April 1998.